

MASTER OF SCIENCE THESIS

Void formation during RTM

An experimental and analytical study on the influence of bundle porosity on void formation during liquid composite molding in woven fabrics.

Floris Zaaijer

Faculty of Aerospace Engineering · Delft University of Technology

Void formation during RTM

An experimental and analytical study on the influence of bundle porosity on void formation during liquid composite molding in woven fabrics.

MASTER OF SCIENCE THESIS

For obtaining the degree of Master of Science in Aerospace Engineering
at Delft University of Technology

Floris Zaaijer

October 2021



Copyright © Floris Zaaijer
All rights reserved.

DELFT UNIVERSITY OF TECHNOLOGY
FACULTY OF AEROSPACE ENGINEERING
DEPARTMENT OF AEROSPACE MANUFACTURING TECHNOLOGIES

GRADUATION COMMITTEE

Dated: October 2021

Committee chair:

Dr. ir. Kunal Masania

Committee members:

Dr. ir. Julie Teuwen

Dr. ir. Barış Çağlar

Dr.ir. René Alderliesten

Abstract

Mechanical air entrapment, void compression and void dissolution are the main mechanisms behind void formation in liquid composite molding. Mechanical air entrapment is induced by the highly non-uniform geometry at the meso- and micro-scale and the heterogeneous properties of the reinforcing material. This results in differences in the velocity profile through the porous- and free flow domains, which can lead to air being entrapped in slow-flowing domains, by resin flowing through the faster flowing domains. Depending on the competition between the viscous flow through the free flow domains and the capillary flow through the porous domains, voids occur either in the intra-bundle domain or in the inter-bundle domain, where the competition between the two flow types can be quantified by the capillary number. Once the voids are entrapped, they can change in size due to void compression and -dissolution, all which occur on considerably different timescales. An experimental set-up was developed which uses fast radiation curing to almost instantly cure the resin during injection and thus detach the different stages of void formation from each other. In this research the relationship between the mesoscale structure of a woven fabric and mesoscale void formation was investigated. The mesoscale structure is strongly related to void formation, as viscous flow is related to the inter-bundle domain size in the through-thickness direction of the preform and capillary flow is related to the mesoscale bundle porosity. As the bundle porosity is related to both the bundle permeability, and the capillary pressure, its influences on void formation were considered to be large, and thus bundle porosity became the main research topic. A 2D semi-analytical model based on mechanical air entrapment was constructed which was capable of determining the filling times of the intra- and inter-bundle domains on the mesoscale. A parameter called the competitive number was introduced which was related to these filling times. Once the competitive number was larger than 1, spherical inter-bundle voids should be formed, once it was equal to 1 no voids should be formed and once it was lower than 1 ellipsoidal intra-bundle voids should be formed. This model was validated experimentally. Flow behavior predicted by the model was compared to video footage of the flow front propagation at the surface of the preform at the macro- and mesoscale during multiple injections. Void volumes, types and locations obtained from the model were compared to voids observed in micro-CT scanned samples and were in agreement with each other. The validated model was eventually used to investigate the effects of bundle porosity on void formation. It was found that increased bundle porosity at a constant global preform porosity, leads to increased intra-bundle flow and decreased viscous flow, thus considerably influencing void formation by mechanical air entrapment. In short injection cycles with high macroscopic flow velocities, which can lead to intra-bundle voids, it could be beneficial to switch a fabric with a higher bundle porosity, as that would effectively reduce the intra-bundle void size. For injections with low macroscopic flow velocities, the opposite would apply, thus usage of fabrics with lower bundle porosities could help to reduce the inter-bundle void volumes.

Table of Contents

Abstract	vii
1 Introduction	1
2 Research scope	5
2.1 Research questions	5
2.2 Research Hypothesis	6
3 Void formation mechanisms	9
3.1 Mechanical air entrapment	9
3.2 Void compression	12
3.3 Void dissolution	13
3.4 Concluding remarks on void formation mechanisms	16
4 Modeling of void formation	17
4.1 Macro-flow modeling	17
4.2 Finite element meso-flow model	21
4.3 Semi-analytical meso-flow model	24
5 Experiments	31
5.1 Experimental set-up	33
5.2 Materials	35
5.3 Characterisation of resin mixture	36
5.4 Sample types and injection procedure	37
5.5 Curing Procedure	40
5.6 Experimental methodology	40

6	Experimental observations	43
6.1	Mechanical air entrapment and void compression	44
6.2	Void dissolution	46
7	Model validation	49
7.1	Macro-flow model	49
7.2	Meso-flow: Analytical model	51
8	Bundle porosity effects	53
9	Conclusion	57
10	Recommendations	59
	References	61
A	Macro-flow model	65
B	Meso-Flow model	73
C	Viscosity Measurements	87
D	Surface tension measurements and processing	97
E	Global permeability determination	99

List of Figures

1.1	Macro-void formation due to race-tracking [1]	2
1.2	Geometrical non-uniformity in a UD-fabric [2]	3
1.3	E-glass woven fabric (left) can be modelled on the mesoscale as shown on the right. Here the domain is split into meso-pores (the inter-bundle domain; green encapsulating domain) and bundles in warp- and weft direction (red- and grey intra-bundle domains). The bundles on the mesoscale are modelled with homogenized properties based on the micro-structure (combination of fibers and micro-pores). Properties such as permeability in the bundle domains are described with a directionality tensor to account for the micro-structural fiber alignment. Bundle porosity at the mesoscale is used to describe the micro-pores in between the individual fibers. . .	4
3.1	Multiple scales in a woven fabric [3]	9
3.2	Modified capillary number versus void content [2]	11
3.3	Void compression due to difference in resin- and air pressure [1]	12
3.4	Low energy nucleation site for bubble formation provided by a degassing agent leading to bubble growth by diffusion and eventually detachment from the degassing agent [4]	15
3.5	Degassing set-up used by Afendi et al. [5]	15
4.1	Volume averaged velocity in a porous control volume [6]	18
4.2	1D linear macro-flow set-up example	19
4.3	Linear pressure drop between inlet and flow front (excluding capillary pressure at the flow front) [7]	20
4.4	Capillary pressure drop as defined in the work of Michaud [8]	22
4.5	Finite element meso-flow model without capillary pressure	23
4.6	2D-simplification of a woven fabric [9]	25
4.7	Intra-bundle void in transverse bundle as per analytical model, where v_g is the macroscopic flow, v_a is the axial intra-bundle flow and v_{bt} is the transverse intra-bundle flow.	27

4.8	Maximum bundle widths- and height observed in micro-CT images of five different samples.	28
4.9	Geometry simplifications	30
5.1	Video-camera and USB-microscope in set-up.	32
5.2	UV-lamp in set-up.	32
5.3	Experimental set-up excluding UV-lamp, camera and USB-microscope	33
5.4	Permeability versus fiber volume content [10]	34
5.5	Components in UV-curable resin system; Omnilane OC1005 (left), Omnicat 250 (middle) and Genocure ITX (right) [11]	35
5.6	Viscosity measurements; literature datafit from Çağlar et al. [11]	36
5.7	Typical pressure measurement during injection by two Balluff BSP00ZK pressure sensors (Void dissolution sample 2)	37
5.8	Location at which surface flow is investigated by USB-microscope and where the resin is spot-cured at different times during the injection. At the high capillary number location the macroscopic flow is dominant over the capillary (intra-bundle) flow, thus resulting in intra-bundle voids. At the low capillary number location the capillary (intra-bundle) flow is dominant over the macroscopic flow, thus resulting in inter-bundle voids. Illustrations on flow behavior and void formation adapted from the work of Mehdikhani et al. [2].	38
5.9	Degassing set-up; -80kPa vacuum pressure for two hours with Scotch Brite tape as a bubble nucleation agent.	39
5.10	Non-uniform flow front shape during injection	41
6.1	Subsurface mechanical air entrapment and void compression for a high capillary number sample (VC4). The lines indicate the flow front in the free flow domains, whereas the arrows indicate the direction of this flow front. Dotted lines indicate that the flow front will pass underneath a bundle.	43
6.2	Micro-CT image of hCa-VC specimen (VC4) indicating intra-bundle void formation in transverse tows: resolution $5\mu m$. Part of the image on the left shows bundles (darker shade of blue), resin (lighter shade of blue) and entrapped air (white). Part of the image on the right indicates the voids which have been filtered out from the micro-CT images and displayed in a 3D-environment. Combining the two images indicates that voids appear in the intra-bundle domains and almost exclusively in those perpendicular to the flow direction.	44
6.3	Micro-CT image of lCa-VC specimen (VC2) indicating inter-bundle void formation: resolution $5\mu m$. Part of the image on the top shows bundles (darker shade of blue), resin (lighter shade of blue) and entrapped air (white). Part of the image on the bottom indicates the voids which have been filtered out from the micro-CT images and displayed in a 3D-environment. Combining the two images indicates that voids appear in the inter-bundle domains and almost exclusively at the intersection of the warp- and weft direction of the bundles.	45
6.4	Void dissolution taken over 150 minutes at half the impregnation length of the preform (lCa-position)	46
6.5	Number of voids observed at the surface by USB-microscope over time once the flow is stopped. Due to injection with an unsaturated resin, voids dissolve back into the resin over time by diffusion. A linear decrease in void-number is observed over time.	47

7.1	Flow front propagation based on 1D-Finite Element macro flow model and experiments. Samples have been assigned both a specimen type name and a specimen number. Here 'FF' denotes flow front-sample, 'VC' denotes void compression-sample and 'VD' denotes void dissolution-sample. The exact definition of the different sample types is described in chapter 5.	50
7.2	Impregnated length versus competitive number, capillary number and void volume. Note that in the graph on the right, colored dots are used to indicate the experimentally obtained void volumes, where the green dot shows the average void volume at the high capillary number location (sample VC4) and the orange dot shows the average void volume at the low capillary number location (VC2). . . .	51
7.3	Location, capillary number and the inverse of the competitive number versus void volume. Void volumes obtained from the semi-analytical meso-flow model are plotted against the capillary number and the inverse of the competitive number. From the capillary number plot (the middle graph) it can be observed that the capillary number - void volume relationship obtained from the model is similar to that found in literature [2], thus indicating the validity of the model and thus the competitive number - void volume relationship.	52
8.1	Bundle porosity effects on the competitive number	53
8.2	Global- and bundle Permeability relationships w.r.t porosity levels	54

List of Tables

5.1	Samples used for further analysis. In the 'used for' column, the analyses performed on a specific sample have been listed. Here 'GPD' stand for global permeability determination, 'CD' stands for cross-section definition, 'VS' stands for void size determination by post-processing of micro-CT scans and 'ST' stands for surface tracking at predefined location by USB-microscope.	41
C.1	Viscosity measurements	89
D.1	Measured surface tension and contact angle from 96 wt % Omnilane OC1005 + 3 wt% Genocure ITX + 1 wt% Omnicat 250. Note that 'PD' in the name column stands for pendant drop method which can be used to determine the surface tension. 'CA' and 'CAST' on the other hand were measurements based on the sessile drop method, which is capable of measuring both the surface tension as the contact angle.	98
E.1	Injection parameters used to determine the global permeability values	99
E.2	Flow front tracking information used for permeability determination	100

Chapter 1

Introduction

Fiber-reinforced polymers (FRPs) are composite materials that offer great potential in strength-weight, modulus-weight and durability optimization [12] and therefore experienced increased attention throughout the years. Traditionally FRPs were predominantly used in the aerospace industry, but its potential is now being recognised in other industries, such as civil-, marine- and automotive engineering. Take for instance the Ramsses project where composite marine vessels up to 85 meters are being designed and tested to increase the fuel-efficiency by drastic weight reductions and to reduce the life cycle costs [13], indicating the great potential.

Different production methods exist for the manufacturing of FRP-composites, such as prepreg-autoclave processing, hot compression molding and liquid composite molding, which all present specific opportunities and limitations. As the aerospace industry has the highest benefit from weight-optimization, FRPs were introduced there at an early stage. To meet rather high safety standards of that industry, prepreg-autoclave composite manufacturing initially was the only suitable manufacturing method for aerospace components, as it was possible to create relatively high-quality products with the method; parts would have minimal manufacturing defects, high fiber volume fractions, and a high degree of cure. However, both the recurrent- as non-recurrent costs for this production method are relatively high and the production rate is limited.

With increased interest over the years from other industries, as well as a drive from the aerospace industry to reduce the costs and increase the production rate of FRPs, a lot of investigation has been performed on the other manufacturing techniques, which therefore improved over time. [12] One of the most promising manufacturing techniques, besides prepreg manufacturing, is liquid composite molding (LCM). This manufacturing technique describes a group of processing methods which are characterized by liquid polymers (the resin) which are forced through a porous medium (the reinforcing material), either by injection, hand-layup or otherwise. When applied correctly, LCM-parts can also achieve a high fiber volume fraction and degree of cure. However, the manufacturing technique is relatively vulnerable to a specific type of manufacturing defect, being the formation of voids in the polymer matrix, which can significantly reduce the mechanical- and dynamical properties of the material (e.g. 6% inter-laminar shear strength reduction for every 1% void content increase [2]). As the

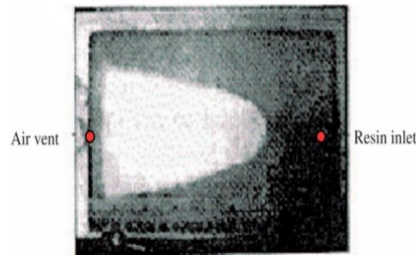


Figure 1.1: Macro-void formation due to race-tracking [1]

polymer matrix has the function to distribute the loads over the reinforcing materials, voids can induce stress-concentrations, which can be detrimental for the part-quality. As such there is a great interest to reduce voids obtained LCM-manufactured parts, which has led to a abundance of research being conducted over the years.

Three different types of voids are distinguished, being macro-, meso- and micro-voids, where the name has to do with the scale and location at which the void appears. Macro-voids, often referred to as dry spots, are specified as large unimpregnated areas, which are the result of a poor injection strategy or race-tracking at the sides of the preform. These macro-voids appear on the macroscale and typically are visible with the naked eye, as indicated in figure 1.1 [1].

Meso- and micro-voids on the other hand, generally cannot be observed by the naked eye. Multiple mechanisms leading to meso- and micro-void formation during LCM have been identified, such as mechanical air entrapment, bubble nucleation and gas formation during cure [2]. From these three mechanisms, mechanical air entrapment is identified as the driving mechanism for void formation.

Mechanical air entrapment is induced by the geometrical non-uniformity and the heterogeneous material properties of the reinforcing material. Reinforcing materials used in LCM generally consist of multiple layers of high-strength textiles. An example of the geometrical non-uniformity of an engineering textile is illustrated in 1.2 [2]. In this UD-fabric, different domains can be distinguished at different scales. At the mesoscale the distinction is made between pores in between bundles. These bundles then can be subdivided into even smaller domains, where within a bundle, individual fibers are distinguished as well as the micro-pores in between the individual fibers. These different domains drastically influence the flow behavior of the resin. At high macroscopic resin velocities, the resin will flow faster through the (meso-)pores than through the bundles as the fibers in that domain obstruct the free flow (which is characterised by the permeability, which differs based on the fiber-orientation relative to the flow), effectively entrapping air within the bundles, referred to as intra-bundle voids. At low macroscopic resin velocities, the flow in the bundle domains can actually exceed the free flow in the meso-pores due to capillary pressure induced by surface tension effects, effectively entrapping air in the meso-pores, referred to as inter-bundle voids. The competition between capillary flow inside the bundles and free flow inside the pores can be quantified by the capillary number, which will be discussed later on.

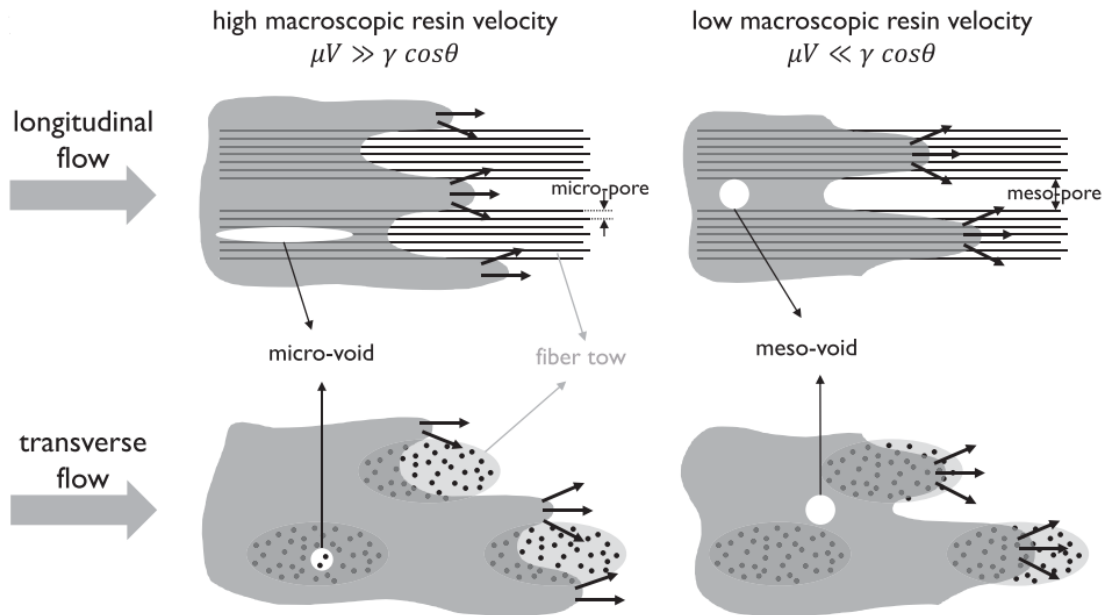


Figure 1.2: Geometrical non-uniformity in a UD-fabric [2]

The multiscale nature of this problem, makes it difficult to properly model void formation, as there is only limited control over the geometry at the microscale during LCM. Multiple models have been presented which can give an indication of the location and size of the pores, but preemptive modelling of the actual geometry remains extremely difficult, therefore not allowing for detailed information on void formation.

Mesoscale void formation modelling however, is promising as it is capable of predicting sizes and locations of inter- and intra-bundle voids. In these models, the geometry is split into free flow (inter-bundle) domains and porous flow (intra-bundle) domains, as illustrated in figure 1.3. The intra-bundle domains here are described by homogenized properties based on the micro-structure (combination of individual fibers and micro-pores). A parameter of specific interest in these homogenized intra-bundle domains, is the bundle porosity (the percentage of micro-pores over the mesoscale bundle domain), as it strongly related to both the bundle permeability and the homogenized capillary pressure induced by micro-structural surface tension effects. The goal of the research is to create a validated model that is capable of quantifying the effects of the mesoscale bundle porosity on void formation. To validate the model a relatively new experimental procedure is used. This experimental procedure is based on injection of an UV-curing resin into a RTM-mould and locally curing the resin by fast-radiation curing. Fast-radiation curing results in a near instant solidification of the resin, allowing to effectively freeze voids in a certain phase of their formation [11].

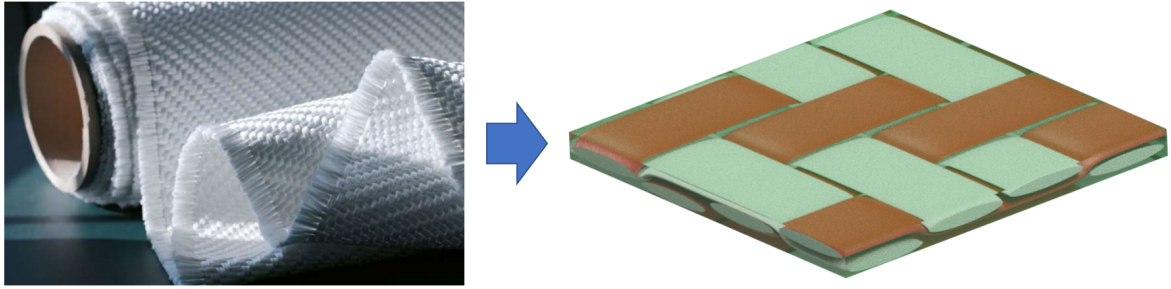


Figure 1.3: E-glass woven fabric (left) can be modelled on the mesoscale as shown on the right. Here the domain is split into meso-pores (the inter-bundle domain; green encapsulating domain) and bundles in warp- and weft direction (red- and grey intra-bundle domains). The bundles on the mesoscale are modelled with homogenized properties based on the micro-structure (combination of fibers and micro-pores). Properties such as permeability in the bundle domains are described with a directionality tensor to account for the micro-structural fiber alignment. Bundle porosity at the mesoscale is used to describe the micro-pores in between the individual fibers.

According to Matsuzaki et al. [14] void mechanics (air entrapment, void compression and -dissolution) occur at different time steps and have been studied in single-layered fabric by video analysis at the surface of the specimens. These studies however are limited to single-layered systems, as it is only possible to record the surface effects. Synchrotron X-ray computed laminography during infusion [15] is emerging as a method to investigate void mechanics in multi-layered fabrics. However, this method still needs to gain maturity. An alternative method to investigate void mechanics in multi-layered fabrics is based on fast-radiation curing as discussed above. This method makes it possible to separate the different stages in void formation. By rapidly curing samples at different time steps in separate injections (where the injection parameters are kept the same), the void mechanisms in multi-layered fabrics can be studied separately by X-ray micro-CT or microscopy. In this report the model will be validated by these techniques and that validated model will then be used to quantify the influence of bundle porosity on void formation.

Chapter 2

Research scope

As mentioned in chapter 1, the non-uniform geometry of the reinforcing materials leads mechanical air entrapment and thus void formation. As such, geometrical changes on the meso- and microscale can greatly influence the void formation behavior. Note that in microscale analysis the distinction between single fibers and micro-pores is made (see figure 1.2), whereas in mesoscale analysis that distinction is not made (see figure 1.3). The goal of this research is to investigate geometrical changes on the mesoscale on void formation. In mesoscale analysis, the intra-bundle flow is determined based on the homogenized (but directional) bundle permeability and the capillary pressure. As void formation is determined by the competition between viscous flow through the (free flow) inter-bundle domains and porous flow through intra-bundle domains, these parameters are of great importance. Both parameters are directly linked to the bundle porosity, and thus this research will be focused predominantly on the effects of the bundle porosity on void formation.

2.1 Research questions

Based on the introduction of this chapter, different research questions have been developed, where the main research question is the following:

'What is the influence of the mesoscale bundle porosity on void formation during resin transfer molding in woven fabrics?'

In order to answer the main question, the research question needs to be divided in subquestions. The first subquestion is 'Which mechanisms lead to void formation in woven fabrics?' and will be answered based on a literature review. The second subquestion is 'What type of model can be constructed to quantify mesoscale bundle porosity effects on void formation?', for which two models will be presented which are based on mechanical air entrapment on the mesoscale. The third- and last subquestion is 'What experimental set-up and methodology can be created to observe individual void formation mechanisms, where the observations can

also be used to validate the model created to quantify mesoscale bundle porosity effects on void formation?'. For this last subquestion an experimental set-up design will be presented alongside the methodology used to observe different void formation mechanisms, for which the observations can be used to validate the mesoscale model. Answering these questions will help to better understand the influence of the bundle porosity on void formation, which is especially important for woven fabric composites, due to their highly non-uniform geometry.

2.2 Research Hypothesis

In this section, the hypotheses based on the questions presented in the previous section will be discussed. As described in the introduction the main void formation mechanisms are mechanical air entrapment, void compression and void dissolution, which will be discussed separately in more depth in the next chapter. The hypothesis for the subquestion on modelling is that mechanical air entrapment at the mesoscale can be modelled by the Brinkman equations in combination with the continuity equation for both the intra- as inter bundle flow domains. Here the intra-bundle domains will be modelled on the mesoscale and therefore individual fibres will not be modelled. After mechanical air entrapment, void compression could be modelled based on the ideal-gas law. Followed by void dissolution, which could be modelled based on Henry's Law on solubility of gasses in resins. However, the assumption, is that void compression and -dissolution do not have to be included in the void formation model as they occur on considerably longer timescales than mechanical air entrapment [14]. To validate this (mechanical air entrapment) model, voids will be studied at different times after formation. To do so, a set-up and methodology needs to be constructed capable of detaching the void formation mechanisms from each other, which is therefore one of the research questions. The hypothesis on what experimental methodology is suitable of doing that, is that injecting a UV-curing resin system in a linear injection mold and rapidly cure the resin by fast radiation curing at different times and locations during the injection, would make it possible to observe the individual mechanisms. As the void formation mechanisms occur subsequently in time, and the timescale at which these occur are assumed to be considerably different, it is thought that fast radiation curing is capable of detaching these mechanisms as the curing procedure only takes a matter of seconds. As such, if mechanical air entrapment indeed can be detached from the other void formation mechanisms, it can be used to validate the model which is solely based on mechanical air entrapment. Here the validation of the model could be done by taking samples near the flow front and measuring the void volume by post-processing micro-CT scanned images, which then can be compared to the void volumes obtained from the model. Void volumes taken from samples near the flow front, are assumed not to be influenced by void compression and -dissolution yet as the resin pressure at this location is nearly identical to the gas pressure inside the void (thus no compression of the void according to the ideal-gas law) and due to the expected relatively slow diffusion rate the entrapped gas in the void will not yet have had the time to dissolve back into the resin system. Based on this validated model bundle porosity effects on void formation can be studied to answer the main research question, where the expected behavior of the bundle porosity on intra-bundle flow, and thus void formation, is presented in the following paragraph.

The bundle porosity is related to the permeability of the porous domains and the capillary pressure induced by surface tension effects. Decreased bundle porosity will lead to decreased bundle permeability and increased surface tension effects.. Based on Gebart's model for axial- and transverse bundle permeabilities [16], it can be observed that there is a nonlinear relationship between the bundle porosity and the permeability. Using the formulation referred to by Michaud [8], which relates the capillary pressure to the surface tension, contact angle and interfacial area between resin and fiber, a linear relationship can be expected between the bundle porosity and the capillary pressure once the static contact angle is used. However, the formulation is actually based on the dynamic contact angle which is related to the macroscopic flow velocity and thus the global preform permeability, which is related in a non-linear manner to the global porosity, therefore indicating the complex interplay between the porosity, surface tension effects and viscous flow. But as the macroscopic permeability is based on a combination of porous medium flow through the bundles and free flow between the bundles, it is assumed influence of the bundle porosity on permeability is more dominant on a local scale (inside the bundles) than on the global scale. Considering all the above, the hypothesis therefore is that the bundle porosity-permeability relationship is dominant over the bundle porosity-capillary pressure relationship, thus the increased bundle porosity at a constant global porosity should promote intra-bundle flow over inter-bundle flow.

2.2.1 Research Objectives

The research objective for this project is:

"To quantify the influence of bundle porosity on void formation by creating a validated model which is capable of predicting the location and volume of voids in a fabric at different bundle porosity levels."

To achieve this objective different sub-goals are set. First the void formation mechanisms will be studied based on a literature review. The second sub-goal is to develop a model for multiscale void formation based on mechanical air entrapment. The third sub-goal is to design an experimental methodology, which can be used to validate the void formation model. This methodology would need to prove that the omission of void compression and -dissolution models in the designed void formation model is reasonable once void volumes of samples taken near the flow front are used to validate the this void formation model. This is based on the assumption that void sizes of samples taken near the flow front are unaffected by void compression- and dissolution, and thus these sizes should be similar to those obtained from the mechanical air entrapment based void formation model. The last sub-goal is to use this validated void formation model to quantify the bundle porosity effects on void formation. Note that other void mechanisms, such as gas formation during cure and resin shrinkage, will not be investigated as they are not identified as the main void formation mechanisms in the literature review of Mehdikhani et al. [2]. In addition to that, exothermal effects, such as the surface tension-temperature relationship, will not be modelled or investigated as it is assumed that their effects in the experimental set-up are negligible, because the resin in this set-up will be injected isothermally, and curing heat is not generated during the injection. As this UV-curing resin will only cure (and generate heat) once UV-light is introduced in the resin, the exothermal effects are assumed not to influence the flow behavior leading to void formation.

Void formation mechanisms

3.1 Mechanical air entrapment

Mechanical air entrapment is the driving factor in the formation of voids and occurs on all scales. As mentioned in the introduction, generally three different scales are distinguished as illustrated in figure 3.1 [3]. In this figure the macro-scale describes the fabric as a single domain, the meso-scale splits to fabric up into domains of bundles and pores, and the micro-scale even distinguishes single fibers, and therefore micro-pores, inside the bundles. Generally, voids are described based on the scale on which the analysis is performed, therefore it is possible to distinguish macro-voids, meso-voids, and micro-voids. The causes leading to air entrapment on the macroscale differ from those related to meso- and micro-void formation. The differences will be discussed in this section.

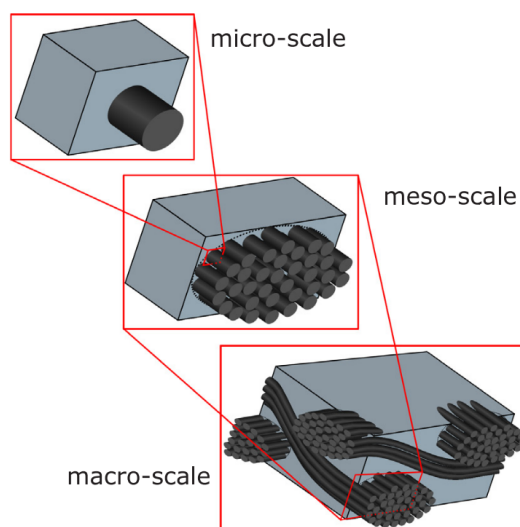


Figure 3.1: Multiple scales in a woven fabric [3]

3.1.1 Mechanical air entrapment at the macroscale

Macroscale void formation due to mechanical air entrapment can be attributed to either a poor injection strategy, a heterogeneous permeability on the macroscale of a preform leading to the resin front prematurely ending up at the outlet, non-permeable media inside the mold, or a combination of the above.

Ideally the resin travels through the preform, impregnating the reinforcing material fully before ending up at the outlet, however, due to the causes described here above, large unimpregnated areas might appear once the flow front on the macroscale prematurely ends up at the outlet. These unimpregnated areas can be referred to as macro-voids and are characterized by a distinct flow front splitting up the macroscale domain in clearly distinguishable saturated- and unsaturated areas. Note that in these saturated areas voids on the meso- and microscale do exist, but these are not considered as voids in macroscale analysis.

To avoid macro-void formation multiple solutions are available, such as for example aiding materials. Aiding materials, such as spiral chord, flow-mesh and breathers, make it possible to locally change the flow behavior and therefore avoid macro-void formation. In addition to that one can also design a suitable injection strategy, combined with the aiding materials, by simulating the macro-behavior in readily available commercial FEM-software, where the software is capable of flow front tracking by modelling the fluid flow by Darcy's law for fluid flow through porous media, therefore distinguishing saturated and unsaturated areas in a time dependent study. Finite element method analysis on the macroscale is relatively easy and offers acceptable results on the macro-flow behavior, making it possible to design an injection strategy to avoid macro-voids altogether, as macro-flow behavior with the help of the aiding materials mentioned above, can be influenced with relative ease. Also, phenomena such as race tracking can take place, but they can also be mitigated by active control of the process, for example by opening/closing gates/vents etc. On the meso- and microscale however, it is rather difficult to influence the flow behavior, leading unavoidably to void formation at those scales as will be discussed in the next subsection.

3.1.2 Mechanical air entrapment at the meso-/microscale

Mechanical air entrapment at the meso- and microscale is predominantly caused by the non-uniform permeability of the preform at these scales [17]. This non-uniform permeability is the results of the geometry at the meso- and microscale.

At the mesoscale, the distinction between pores (inter-bundle domains) and bundles is made. Flow through inter-bundle domains in mesoscale analysis is described by viscous (free) flow and flow through fibrous domains (the bundles) is described by porous medium flow. Note that at the mesoscale individual fibers are not considered. Instead, fibrous domains are described by an averaged directional permeability tensor. The permeability tensor is anisotropic to account for the fiber orientation on the microscale, which influences the flow behavior on the mesoscale considerably. Different analytical methods have been proposed to determine the permeability in different directions of porous domains. Possibly the most well-known methods are those of Kozeny-Carman [12] and Gebart [16], which can be used to determine the directional permeability of bundles based on the geometry at the microscale.

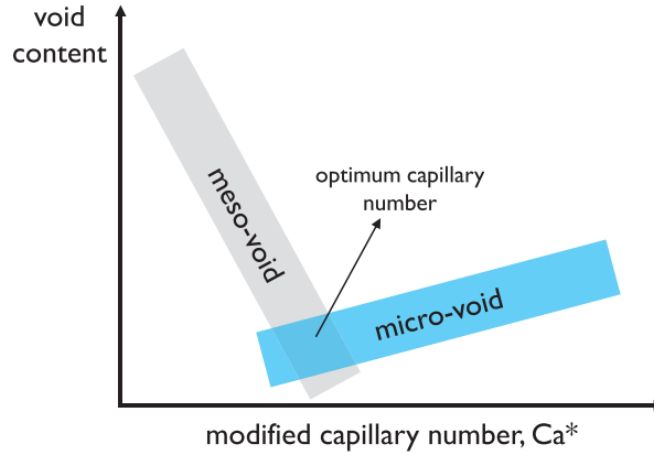


Figure 3.2: Modified capillary number versus void content [2]

At the microscale, the fibrous domains (the bundles) from the mesoscale analysis are subdivided into fibers and micro-pores. Flow through the micro-pores is described by the Navier-Stokes equations to account for capillary pressure stemming from surface tension effects and viscous drag induced by the fibers. Due to these effects a non-uniform flow front can be modelled throughout the different domains, which can lead to mechanical air entrapment.

Non-uniform permeability of the preform is the driving parameter for a non-uniform flow front leading to mechanical air entrapment. Capillary pressure induced by surface tension effects, however, can also play a crucial role in the formation of voids by mechanical air entrapment. Capillary pressure induced by surface tension effects can locally increase the flow velocity in the fibrous domains, and when the capillary pressure effect is dominant enough, it can overtake the viscous flow through the pores, leading to inter-bundle voids. However, if the overall flow is dominated by hydrodynamic forces and the surface tension effects therefore are not strong enough, the flow through the inter-bundle domain exceeds the flow through the fibrous domains due to the higher permeability inside the inter-bundle domain, leading to mechanical air entrapment inside the bundles and therefore intra-bundle voids.

The competition between hydrodynamic forces and surface tension effects can be quantified with the so-called modified capillary number [18] (referred to as the capillary number in the of this report), which can indicate where voids will appear and to what extend. The capillary number in this case is given by:

$$Ca = \frac{\eta u_s}{\gamma_{lv} \cdot \cos(\theta)} \quad (3.1)$$

Here η is the viscosity of the fluid, u_s is the resin flow velocity at the macroscale, γ_{LV} is the surface tension and θ is the contact angle. In addition to determining the location and approximate amount of voids, the capillary number can also be used to find the optimum combination of hydrodynamic – and capillary pressures to minimize the total amount of voids obtained in a LCM-process (see figure 3.2 [2]).

3.2 Void compression

Voids formed by mechanical air entrapment will change in size due differences in resin- and air pressure. Before the air entrapment, the air pressure will be similar to the outlet pressure. As the resin encloses the air, a pressure equilibrium needs to be formed between the air and the resin as illustrated in 3.3 [1]. To reach equilibrium, changes in the void volume will occur in order to alter the air pressure and therefore balance out the resin pressure, which can be described by the ideal gas law:

$$PV = n \cdot R \cdot T \quad (3.2)$$

Where P, V and T are the pressure, volume and temperature of the substance respectively, R is the ideal gas constant and n is the amount of substance. Considering an isothermal setting, the pressure then can be altered by changing the volume. Lundström et al. [19] initially proposed the following method to describe void compression based on the ideal gas law and the location along the impregnation length in a macroscale analysis:

$$V_{\xi} = \frac{P_0}{P_0 + \Delta P \frac{\xi}{L}} \cdot V_0 \quad (3.3)$$

Where P_0 is the initial pressure in the bubble, ΔP is the driving pressure difference in the mould, V_{ξ} is the volume at location ξ along the impregnation length, L is the total impregnated length at a given time and V_0 is the initial volume of the bubble formed by mechanical air entrapment. This equation however, does not include surface tension effects, which can have a considerable effect on the pressure state in the porous domains [1, 20]. Therefore, in 1997 Lundström [21] expanded the equation to include capillary pressure, which Park and Lee [1] denoted as:

$$V_v = \frac{P_i + P_c}{P_v + P_c} \cdot V_i \quad (3.4)$$

Where P_c is the capillary pressure and V_v is the void volume. In general this formulation can be applied to describe void compression- or expansion for both spherical- and ellipsoidal voids. Final interesting remarks to be made are that alterations in the air pressure inside the void can influence the bundle permeability (increasing the air pressure inside the void

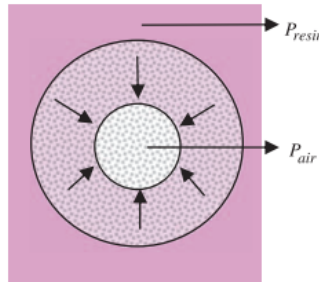


Figure 3.3: Void compression due to difference in resin- and air pressure [1]

leads to a reduction in the bundle permeability as the increased pressure hinders the resin flow [1, 20]) and that void compression occurs relatively slow in the porous domains as the resin flow through these domains is lower with respect to free flow domains due to the low permeability of the porous domains [1]. Hence, resin flow needed to compact the void occurs over a certain period of time and takes longer in the porous domains.

3.3 Void dissolution

As mentioned in the introduction, an important mechanism for void formation, is void dissolution. Void dissolution is related to the solubility of gasses inside liquids on a molecular level, and thus for liquid polymers that entails that gasses can be dissolved into the liquid and stored in between the individual polymer chains. The amount of gas that can be stored inside a volume of resin, is thermodynamically defined. Change in a thermodynamic parameter such as pressure or temperature, therefore will result in a change in the solubility capacity.

During RTM the temperature- and pressure changes throughout the injection lead towards local changes in the solubility capacity of gas into the resin. Depending on the pressure state of the resin, and the initial concentration of gas dissolved into the resin, the resin can become either supersaturated or unsaturated. Once the resin is supersaturated, gas is forced out from the resin and can accumulate and therefore form bubbles inside resin, and thus lead to void formation. On the other hand, once the resin is unsaturated, gas bubbles formed by for example mechanical air entrapment can dissolve back into the resin and therefore reduce the void size.

To model the effects of void dissolution, Wood and Bader [22] used a diffusion based model which relates the void size to the initial void size, a diffusion coefficient and dissolution time as given by:

$$R_v^2 = R_{v0}^2 - \frac{2D_r}{\rho} (C_s - C_{\infty}) t \quad (3.5)$$

Where R_v is the void radius at time 't', R_{v0} is the initial void radius, D_r is the diffusion coefficient, ρ is the density of the gas, C_s is the saturated gas concentration and C_{∞} is the gas concentration at $t = \infty$. Here the saturated gas concentration can then be related to the resin pressure at that location by Henry's law:

$$C_s = H \cdot p \quad (3.6)$$

Note however that this model only applies to circular voids under specific conditions. Dissolution of elliptical voids, which are formed inside the bundles at high capillary numbers, can be approximated by other, more complex models. These however are not discussed in this research as the intention of this section is just to give an indication of the mechanisms behind void dissolution and on how to model them.

Void dissolution during LCM however, remains vastly complex due to the geometry on the microscale, surface tension effects and the movement of bubbles during the injection. Lundström et al. [21] for example pointed out that voids which move through the resin, can pass through regions with varying saturation concentrations, leading to different diffusion rates. In addition to that, they observed that voids which are entrapped inside the bundles, can decrease in size due to diffusion, which lowers the constrictive surface tension effects on the bubbles, allowing them to escape the bundle and flow freely through the inter-bundle space at which void dissolution occurs at a different rate.

Though precise modelling of void dissolution in LCM remains difficult, the theory can be applied preemptively to reduce the void content of LCM-manufactured parts by injecting with an unsaturated resin mixture. To obtain an unsaturated resin, gas needs to be pulled from the resin. This can be done by a degassing procedure, where resin is placed inside a vacuum container and degassed for a certain period of time. During this procedure the resin temporarily becomes supersaturated and therefore gas is forced out from between the polymer chains, accumulates to bubbles which then rise to the resin surface per Archimedes' law and evacuate the resin [4]. However, a large part of the gas might remain trapped inside the resin once the gas fails to nucleate a bubble and thus cannot rise through the resin and escape the mixture. Labordus [4] identified this problem with bubble nucleation during degassing and suggested to apply degassing agents which locally reduce the nucleation energy to form a bubble. An example of such an agent is for instance Scotch-Brite tape. This tape is a low surface energy, sponge like material which is placed at the bottom of a resin container in a vacuum chamber. Initially micro-pores present in the tape contain small air bubbles, which remain inside the sponge as it is submerged into the resin mixture. Due to diffusion of gas from the supersaturated resin towards the bubbles captured in the tape, the bubbles grow, as is illustrated in figure 3.4 [4]. At a certain bubble volume the bubble rise force (as defined by Archimedes' law) exceeds the constraining surface tension force and the majority of the bubble detaches from the tape. The bubble then rises through the resin and grows along the way due to gas diffusion into the bubble and evacuates the mixture. The remainder of the original bubble in the tape again grows by diffusion and the process repeats until the gas saturation concentration reaches a new steady state equilibrium, where the gas diffusion rate drops over time due to the smaller saturation concentration.

An alternative to bubble formation by introduction of nucleation agents, is artificially adding bubbles to the resin mixture at the bottom of the container. This method is called sparging. The artificially added bubbles rise through the resin mixture and grow by gas diffusion. Afendi et al. [5] observed that this method can be very efficient with a 50 - 60% oxygen removal relative to the initial concentration after 15 minutes whilst degassing at a (vacuum) degassing pressure of 90 mBar.

Degassing by sparging however, can lead to micro-bubble formation in the resin [23], which can get stuck once the resin is degassed to the extent that there is not gas left for bubble growth. To filter out these micro-bubbles Afendi et al. [5] proposed to force the degassed resin through a fine porous medium, which appeared to work well in the experimental set-up (see figure 3.5 [5]). Note however, that their set-up used a nucleation agent rather than sparging, but the methodology should hold for sparging methods as well.

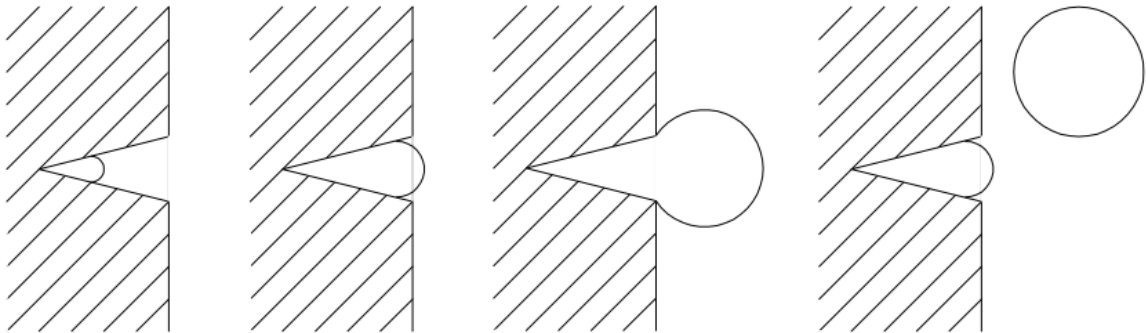


Figure 3.4: Low energy nucleation site for bubble formation provided by a degassing agent leading to bubble growth by diffusion and eventually detachment from the degassing agent [4]

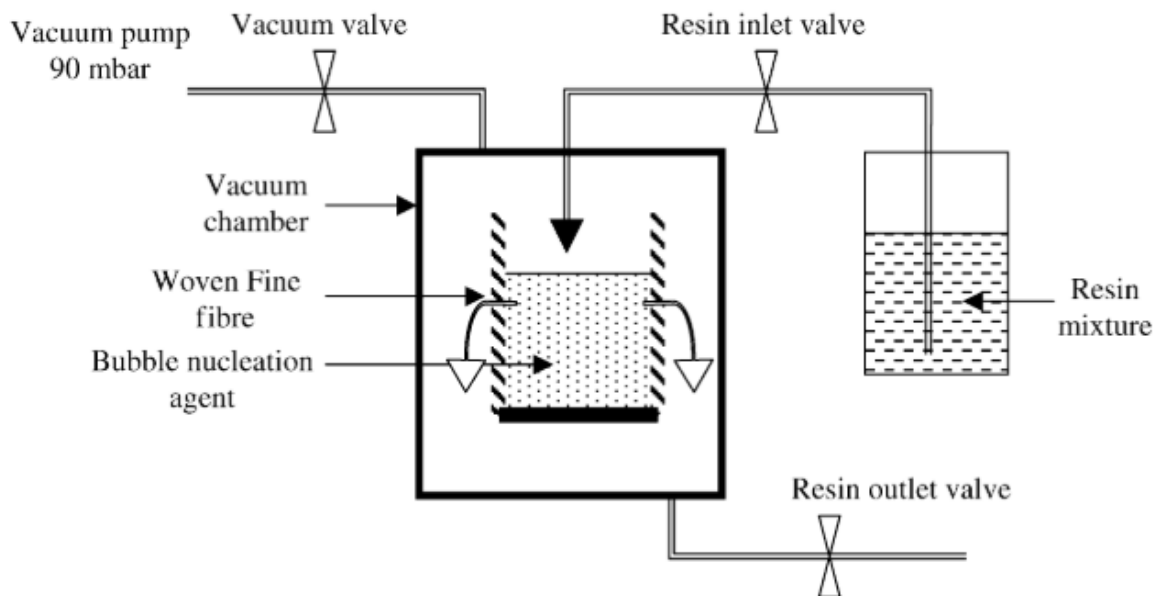


Figure 3.5: Degassing set-up used by Afendi et al. [5]

3.4 Concluding remarks on void formation mechanisms

In this chapter, the three main void formation mechanisms have been discussed, which answer the research question: 'Which mechanisms lead to void formation in woven fabrics?'. Voids initially are formed by local differences in flow velocity profile throughout the preform, which is the result of a highly non-uniform geometry. Once gas is entrapped by resin, the void size decreases due to the surrounding resin pressure which is higher than the pressure of the entrapped gas. To form a force equilibrium, the void reduces in size, resulting in an increase in the gas pressure according to the ideal-gas law. The entrapped pockets of gas (the voids), can then change even further in size due to a mechanism which is called void dissolution. Void dissolution here, is a diffusion based mechanism. A certain amount of gas can be stored in between the polymer chains of the resin depending on the pressure- and temperature state of the resin, where the pressure - storage relationship can be approximated by Henry's law. Once either the pressure or the temperature of the resin changes, the storage capacity changes, thus resulting in either a supersaturated or unsaturated resin mixture. To obtain the equilibrium state, gas is either forced out of the resin, or dissolved back into the resin to reach a saturated mixture. As such, voids present in the resin, can either grow or shrink due to diffusion. These three mechanisms occur subsequently and at different time scales [14]. Void compression occurs after mechanical air entrapment, but might take some time as the pressure differential between resin and the entrapped gas is relatively low right after air entrapment (due to the voids vicinity to the flow front) and thus the flow velocity which should reduce the void size at that moment is relatively low and so is the expected void size reduction due to the small differences between resin- and gas pressure. After mechanical air entrapment and void compression, void dissolution occurs, but due to the relatively high viscosities of resin systems, the diffusion rate is low and thus void dissolution occurs over a much longer period of time. Thus, as mentioned in chapter 2, the mechanisms occur at different time scales and the influences of void compression and -dissolution directly after void formation should be relatively small, making it reasonable to omit the mechanisms from the eventual model if the resin can be cured rapidly directly after void formation (near the flow front).

Modeling of void formation

Fluid flow models are needed to construct void formation models. In this chapter three different fluid flow models will be discussed, being a macro-flow model, a finite element (FE) meso-flow model and a semi-analytical meso-flow model.

From the macro-flow and FE-meso-flow model the modelling principles will be discussed as they they can be used in readily available software packages such as PAM-RTM or Comsol Multiphysics, where void formation can be observed by tracking the cell saturation of the fluid over time, which should apply to arbitrary geometries. The semi-analytical model however, uses geometry simplifications and void-shape fitting functions and thus this model needs to be discussed in depth.

4.1 Macro-flow modeling

Macro-flow modeling can be used to describe the propagation of a fluid through a porous medium, where volume averaged quantities are used to homogenize the domain. In this section the fluid flow principles used, their implementation in the model, and the validation of the model will be presented. Based on this model mechanical air entrapment on the macro-scale could be used to predict macro-void formation. However, as the goal is to quantify the relationship between bundle porosity and void formation at the mesoscale, macro-void formation will not be investigated. The pressure distributions obtained from the macroscale analysis however, are used as input in the meso-scale analyses. The macro-scale model will be validated based on video-camera footage in chapter 7, which is also used to determine the macro-scale permeability.

4.1.1 Fluid flow principles

Fluid flow through a porous medium on the macro-scale is generally described by Darcy's law in combination with the continuity equation, where the domain is split into clearly distinguishable saturated and non-saturated zones [24], where Darcy's law is given by:

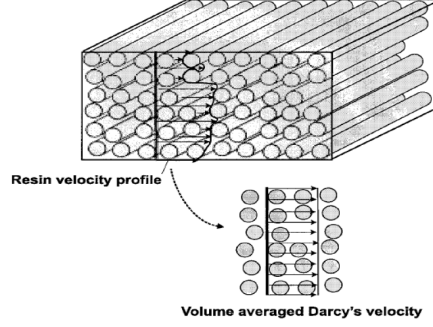


Figure 4.1: Volume averaged velocity in a porous control volume [6]

$$\bar{v} = -\frac{\bar{K}}{\mu\phi} \cdot \nabla P \quad (4.1)$$

Where \bar{v} is the volume averaged velocity, \bar{K} is the saturated permeability tensor, μ is the dynamic viscosity, ϕ is the porosity and ∇P is the pressure differential applied over the domain.

From this equation it can be seen how averaged values are used to determine the velocity on a high order scale. In reality the velocity profile however, is very non-uniform due to the anisotropic geometry of the fabric, which consists of free flow- and porous domains at the meso- and micro-scale, which is indicated in 4.1 [6]. Note that the permeability tensor in Darcy's law is also volume averaged over the domain and is written in the following manner:

$$\bar{K} = \begin{bmatrix} K_{xx} & K_{xy} & K_{xz} \\ K_{yx} & K_{yy} & K_{yz} \\ K_{zx} & K_{zy} & K_{zz} \end{bmatrix} \quad (4.2)$$

Where the permeabilities in the different directions generally are obtained from experiments where video analysis is used to map the flow progression over time and to solve for the permeability based on Darcy's law [25, 26].

The velocity profile obtained by Darcy's law can be combined with the continuity equation to describe the fluid mass progression through the domain, where the continuity equation is given by:

$$\frac{dM}{dt} = - \oint_S \rho \bar{v} \cdot d\bar{S} \quad (4.3)$$

Which describes how the mass of a certain control volume changes over time, where the right hand side of the equation describes the mass leaving/entering the control volume of the surface of that control volume. Note that the density in this equation is denoted by ρ .

Equation 4.3 can then be rewritten based on the divergence theorem to a volume integral:

$$\int_V \frac{\delta \rho}{\delta t} dV = - \int_V \bar{\nabla} \cdot (\rho \bar{v}) dV \quad (4.4)$$

Assuming the fluid to be incompressible, the density term becomes a constant, meaning that the derivative is zero so that equation 4.4 reduces to:

$$\bar{\nabla} \cdot (\bar{v}) = 0 \quad (4.5)$$

The combination of the Darcy velocities and the continuity equation can provide excellent results for the flow propagation of an fluid on the macroscale, when Newtonian incompressible fluids are modelled. In this research the resin is assumed to behave as an incompressible, Newtonian fluid. In addition to that, the experiments were conducted under isothermal conditions (no heat induced by curing etc.), therefore the viscosity is assumed to be constant throughout the injection. The validity of these assumptions will be tested in chapter 7 based on a comparison between the experimental results and a macro-flow model.

4.1.2 Model set-up

As the goal of this model is not to capture macro-scale void formation, but to model the macro-flow through an porous medium in a linear injection system, the model can be simplified into an 1D-problem. The (Python) model used for the analysis can be found in Appendix A.

A certain number of nodes is taken over the injection length, for which the pressure profile and saturation levels can be tracked. The first node is set as fully saturated ($\phi = 1$) and the other nodes are set as fully unsaturated ($\phi = 0$). Based on these saturation levels the code is capable of tracking the flow front (also once the flow propagates through the preform). The first node is then assigned the inlet pressure, and node at the location of the flow front is assigned the outlet pressure. Nodal pressures in between the inlet- and flowfront nodes are assigned as unknown pressures. The unknown pressures can be calculated by construction of a global permeability matrix, where elemental permeabilities are stored based on the saturation levels. Here the elemental permeabilities are given by:

$$K_{element_{xx}} = -\frac{K_{xx} \cdot A}{\mu \cdot L_{element}} \quad (4.6)$$

Here $K_{element}$ is the elemental permeability in the x-direction, K_{xx} is the global permeability in the x-direction, A is the cross-sectional area of the element, μ is the dynamic viscosity and $L_{element}$ is the element length. With these element permeabilities the global permeability matrix can be constructed, which can be used to calculate the unknown pressures as well as the flow rates by creating a system of equations as shown in equation 4.7, which is based on a simplified three-nodes-two-elements example (as shown in figure 4.2).

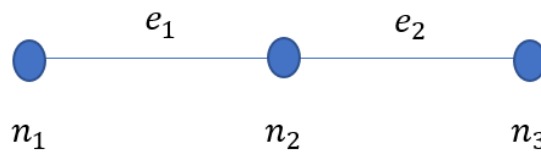


Figure 4.2: 1D linear macro-flow set-up example

$$\begin{bmatrix} Q_1 \\ Q_2 \\ Q_3 \end{bmatrix} = \begin{bmatrix} K_{xx}^1 & -K_{xx}^1 & 0 \\ -K_{xx}^1 & K_{xx}^1 + K_{xx}^2 & -K_{xx}^2 \\ 0 & -K_{xx}^2 & K_{xx}^2 \end{bmatrix} \begin{bmatrix} P_1 \\ P_2 \\ P_3 \end{bmatrix} \quad (4.7)$$

This system of equations is based on Darcy's law and needs boundary conditions in order to be solved. Two boundary conditions have already been discussed, being that the first node represents the inlet and thus there the inlet pressure should be applied, and that at the last node in the system which represents the flow front the outlet pressure should be applied. The last boundary condition used to solve this system is based on the continuity equation where the flow at the middle nodes is set at zero, because the node is fully saturated and thus what enters the node from one side, must leave the node on the other side (else the node would overflow). By using these three boundary conditions, the number of unknowns becomes equal to the number of equations and thus can be solved to determine the unknown pressures:

$$[P_2] = [-K_{xx}^1 P_1 - K_{xx}^2 P_3] \cdot [K_{xx}^1 + K_{xx}^2]^{-1} \quad (4.8)$$

Which in the case of 1D-analysis of flow propagation through an homogenized preform, will lead to a pressure distribution as shown in 4.3 [7]. The pressure distribution then can be used in equation 4.7 to calculate the unknown nodal flows at the inlet and flowfront. The flow at the flowfront (nodes 1 and 2 are fully saturated, node 3 is unsaturated), fills node 3 and the time to saturate the node can be determined linearly. Once the node is filled, the system of equations is then expanded (with the next unsaturated node in line with the flow direction) and the flow propagation is tracked until the entire preform is saturated and the simulation is stopped. Note however, that according to the model in Appendix A, the flow at the outlet node is equal to the flow at the inlet node and the flows at the nodes in between is set to zero. This would imply that the saturation level at the inlet-node would drop due to the outgoing flow. However, in reality the inlet is coupled to a resin container, which in the system of equations can be added locally to the continuity equation as a source term. This however, has not been done in this model, but the inlet node is kept fully saturated artificially, as this gives the same results.

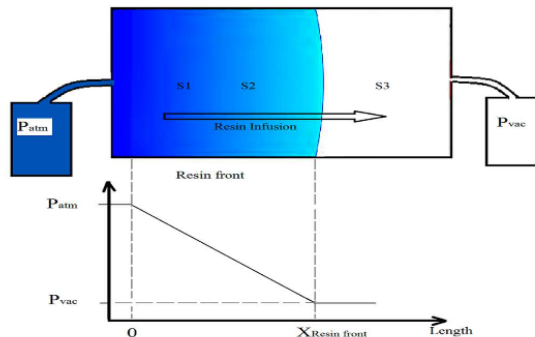


Figure 4.3: Linear pressure drop between inlet and flow front (excluding capillary pressure at the flow front) [7]

4.2 Finite element meso-flow model

Comsol Multiphysics was used to model void formation on the meso-scale, by using the 'Free-and-Porous Media Flow'(FP)-module and combining that with the 'Level Set'(LS)-module, which were both available in their application library.

The FP-module allows the user to assign free flow- and porous flow domains to the geometry. A single layer of geometry was imported into Comsol and consisted of fibers in warp- and weft direction, and a body which encapsulated these bundles as to represent the free flow domain. The bundles then were assigned as porous domains, which allowed the user to assign a permeability tensor to these porous domains. The encapsulating domain was then automatically assigned as a free flow domain. The function of the FP-module is to determine the velocity profile and pressure distribution according to a predefined set of boundary conditions and preform saturation state, for which it uses the Brinkman equations combined with the continuity equation (as taken from the work of Park and Woo [27]):

$$\rho \left[\frac{\partial \vec{v}}{\partial t} + \vec{v} \cdot \nabla \vec{v} \right] = -\nabla P - \frac{\mu}{\tilde{K}} \vec{v} + \mu_e \nabla^2 \vec{v} + f \quad (4.9)$$

Where the new parameters are the effective viscosity μ_e and the body force f . The main benefit from the Brinkman equation is that it can describe both free- as porous flow by using specific values for the effective viscosity. Because once the effective viscosity is set to zero, it reduces to Darcy's law and once a sufficiently large value is taken the Brinkman equation reduces to the Navier-Stokes flow equation [27]. In order to solve the problem, boundary conditions were needed. The boundary conditions applied were that a pressure differential was applied between two opposing sides of the preform and that the side with the higher pressure was set to be fully saturated. To reduce the wall effects, periodic boundary conditions were used at the other sides of the preform as it was assumed that the wall effects for a first-order model were negligible once a multi-layered system was used and only a single ply was modelled. With these boundary conditions it was possible to obtain a velocity profile, which then was fed into the LS-module to update the saturation levels of the cells based on a set timestep.

Unfortunately it was not possible to add a uniform capillary pressure term to the porous domains based on the modules available in the Comsol-Multiphysics application library, but the following attempts have been made to add a capillary pressure term to these domains.

The first try was to correct the velocity profile obtained from the Brinkman equations (without inclusion of a capillary term) in the porous domains. This velocity profile was corrected for the porous domains based on the following approximation:

$$u_{corrected} = \left(1 + \frac{\frac{dP_c}{dn}}{\frac{dP}{dn}} \right) \cdot u_{original} \quad (4.10)$$

Where u is the velocity profile, dP/dn is the externally applied pressure differential and dP_c/dn is the pressure differential induced by the surface tension effects. The main reason that this approximation did not produce reasonable results was that it was not really possible to define a correct surface-tension induced pressure differential, as no suitable literature on how to do that properly was found.

A second effort was to add the capillary pressure as a constant pressure over the saturated domain and lower its contribution towards the flow front as shown in figure 4.4 [8]. A very unrealistic flow propagation was observed and it was thought that this might be caused by a discrepancy with the continuity equation, because if the pressure differential at the flow front is larger than in the fully saturated areas, the flow velocity near the flow front is larger. As such, resin would have been pulled from the saturated areas, without there being enough resin being fed into the saturated cells from the inlet side, effectively pulling vacuum voids, which did not make sense. Different variations of this have been tested as well, such as applying a local pressure drop at the flow front, but these of course yielded the same problem.

Other forms, such as applying surface tension models from soil science (e.g. Van Genuchten) from the Comsol application library and adding it to the weak form of the bundle domains were tried as well, but without success. In addition to that, their relevance to the meso-scale analysis is also questionable because they are meant for homogenized soils, rather than highly directional fibers.

All this led to the belief that there is a need for a new capillary pressure model which also includes a way on how to properly take the differential with respect to saturation and impregnation length, for meso-scale analysis. Unfortunately it was not feasible (also because the models are very computationally expensive, because a very fine mesh is needed to properly track the flow in between the bundles) to do that in this research and therefore an analytical model has been proposed, which will be discussed in the next section.

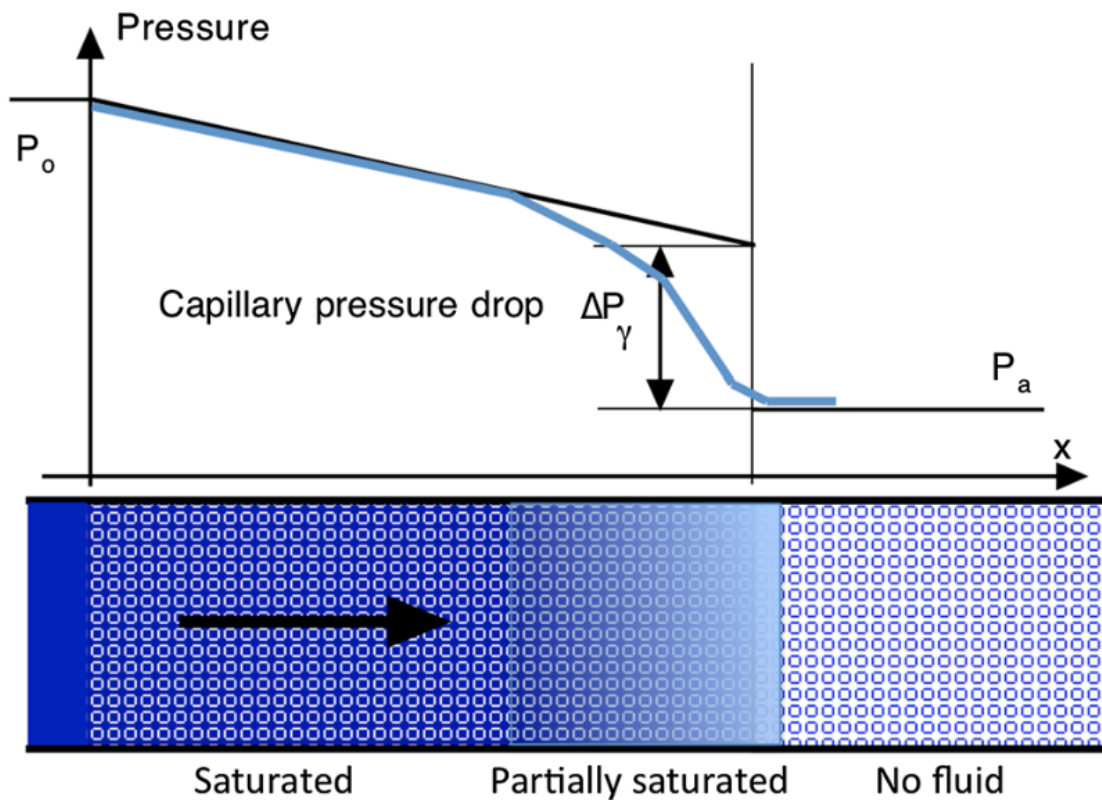


Figure 4.4: Capillary pressure drop as defined in the work of Michaud [8]

Model runs without the inclusion of the capillary pressure, did show the free-flow wraps around the bundles in a high capillary pressure setting (as shown in figure 4.5), but it also indicates that with the relatively low bundle permeabilities based on the Gebart permeability models for axial- and transverse permeabilities [9], the surface tension effects are non-negligible as there is nearly any impregnation of the bundles, which is unrealistic.

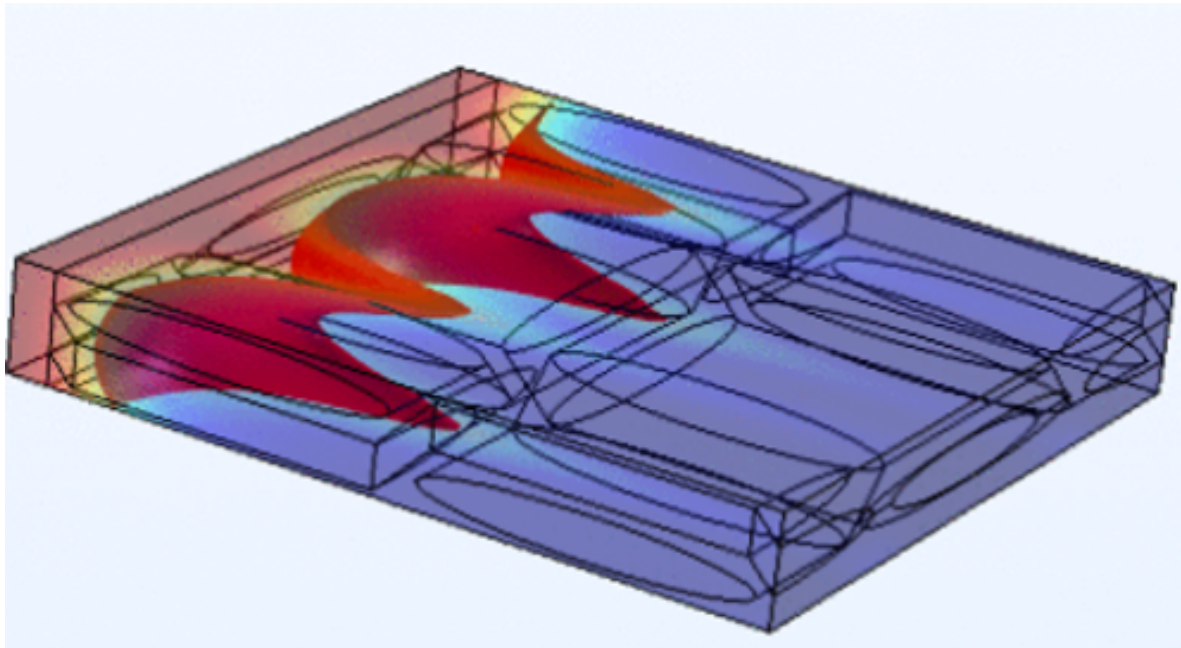


Figure 4.5: Finite element meso-flow model without capillary pressure

4.3 Semi-analytical meso-flow model

The semi-analytical meso-flow model is based on the void formation model from Matsuzaki et al. [9] and can be found in Appendix B. In their work they presented a methodology to simplify a woven fabric into a 2D-geometry (see 4.6 [9]), where the cross-sectional properties (such as the permeability and the porosity) are height averaged over the actual domain, because in reality the through thickness geometries consist of free flow- and porous domains as the bundles cross over each other. In addition to that, the bundles have elliptical cross-sections which are simplified to rectangular sections. Though the meso-flow model presented in this thesis is based on height-averaging (homogenizing) of properties in the through-thickness direction and determining the void size based on the ratio of intra- over inter-bundle filling times, which were introduced in the work of Matsuzaki et al., the models vastly differ. The main differences between this new model and that of Matsuzaki et al. is that flow velocities in the intra-bundle domain will not be based on the height-averaged permeability of the upward crimp (section at the corners of warp- and weft direction), but rather the height-averaged permeability of the actual domains. In addition to that, the new model also includes intra-bundle void size prediction and shape functions for inter- and intra-bundle void sizes. Lastly a new parameter is introduced in this new model, which is the competitive number, which is the ratio of the filling time of the free flow (inter-bundle) domain over the filling times of the intra-bundle domains. This number has the advantage over the earlier discussed capillary number, as it is based on meso-structural properties, which are not included in the capillary number analysis. In addition to that a clear relationship between the competitive number and different void types and sizes exist. That relationship was not clearly included in the capillary number analysis. A detailed explanation of all the newly induced parameters, and thus the newly developed model, will be provided in the following paragraphs.

The semi-analytical meso-flow model used in this research distinguishes three domains, being the axial-bundle domain, the transverse-bundle domain and the inter-bundle domain. Meso-void formation in the inter-bundle domain will occur once the filling time of the axial-bundle domain combined with the filling time of the transverse bundle domain is lower than that of the inter-bundle domain. The ratio over the intra-bundle filling times over the inter-bundle filling time can eventually be used to determine the void size. To determine the filling times a couple of assumptions have been made. The first assumption is that the applied (macroscopic) pressure differential over the domain can be taken as a constant. In addition to that the capillary pressure differential which is added to the intra-bundle domains, can be approximated by taking the capillary pressure as presented in equation 4.11 and divide that by the inter-bundle length L_L as indicated in figure 4.6.

$$\Delta P_\gamma = -S_f \gamma_{ma} \cos(\theta) \quad (4.11)$$

The next assumption is that the elliptical shape of the bundles can be simplified to a rectangle by dividing the bundle area (as per $A = \pi \cdot width_{max} \cdot height_{max}$), by the maximum bundle height. Based on the dimensions of the simplified rectangular bundles, and a predefined bundle spacing, the inter-bundle dimensions (L_T and L_L) can be determined.

The next assumption is that the intra-bundle domains can be homogenized through-thickness by height-averaging the porosity over the ply-thickness with the following equation:

$$\phi' = 1 - \frac{h_{bundle}}{t_{ply}} \cdot (1 - \phi) \quad (4.12)$$

Where ϕ' is the apparent (height-averaged) porosity, h_{bundle} is the experimentally obtained averaged maximum bundle height, t_{ply} is the experimentally obtained averaged ply thickness and ϕ is the bundle porosity based on the experimentally observed global porosities (which can be found in appendix E).

The apparent porosities can be used to determine the axial- and transverse permeabilities of the intra-bundle domains based on the bundle-permeability model of Gebart:

$$K_{axial} = \frac{8R^2}{c_{axial}} \frac{\phi^3}{(1 - \phi)^2} \quad (4.13)$$

$$K_{\perp} = C_{\perp} \left(\sqrt{\frac{V_{fmax}}{1 - \phi}} - 1 \right)^{5/2} R^2 \quad (4.14)$$

Where R is the fiber radius, $c_{axial} = 53$, $c_{\perp} = 16/9\pi\sqrt{6}$, $V_{fmax} = \pi/2\sqrt{3}$ (assuming hexagonal ordering of the fibers [9, 28]) and ϕ is the bundle porosity, and thus in the case the apparent porosity. These permeabilities then can be used to determine the flow velocities through the intra-bundle domains based on Darcy's law:

$$v_{axial} = \frac{K_{axial}(\phi') * \left(\frac{dP}{dn} + \frac{P_c}{L_L} \right)}{\mu * \phi'} \quad (4.15)$$

Where v_{axial} is the intra-bundle velocity in the direction of the fibers, P_c is the capillary pressure according to equation 4.11 and μ is the viscosity. Note that this velocity is used for

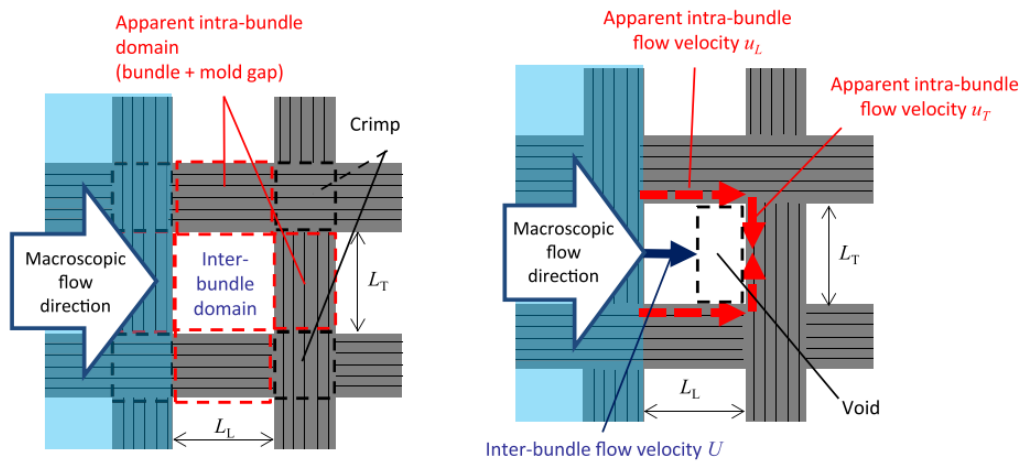


Figure 4.6: 2D-simplification of a woven fabric [9]

both the axial-intra-bundle as the transverse-intra-bundle domain, because once the flow turn around the corner at the intersection between warp- and weft direction, the flow aligns again with the fiber direction. The filling times of the domains can then be approximated with the following equations:

$$t_L = \frac{L_L}{v_{axial}} \quad (4.16)$$

$$t_T = \frac{0.5 \cdot L_T}{v_{axial}} \quad (4.17)$$

Note that only half the transverse inter-bundle length is taken in the determination of the filling time of the transverse intra-bundle domain due to symmetry. To quantify the competition between macroscopic flow and intra-bundle flow, the ratio of the filling times needs to be calculated. The inter-bundle domain filling time in this model is determined with the following set of equations:

$$v_g = \frac{K_g \cdot \left(\frac{dP}{dn}\right)}{\mu \cdot \phi} \quad (4.18)$$

$$t_g = \frac{L_L}{v_g} \quad (4.19)$$

In these equations K_g is the experimentally determined global permeability and pressure different, dP/dn is given by:

$$\frac{dP}{dn} = \frac{P_{inlet} - P_{flowfront}}{l_{impregnation}} \quad (4.20)$$

Where P_{inlet} is the inlet pressure, $P_{flowfront}$ is the flow front pressure (equal to the outlet pressure) and $l_{impregnation}$ is the impregnated preform length at which the analysis is performed.

The ratio of the filling times can be then quantified by introducing a new parameter, which is the competitive number (somewhat analogous to the capillary number), which is given by:

$$C_o = \frac{t_g}{t_L + t_T} \quad (4.21)$$

As this number described the ratio of the inter-bundle filling time over the intra-bundle filling time, the following conditions should apply:

- $C_o < 1$: Intra-bundle voids are formed.
- $C_o = 1$: No voids are formed.
- $C_o > 1$: Inter-bundle voids are formed.

Based on this set of conditions it is possible to determine which type of voids will be formed and thus, how to approximate their size. If the competitive number is larger than 1, meso-voids will be formed, which predominantly are spherical. With the following equations, the void volume therefore can be approximated:

$$r_s = \frac{L_L}{2} \cdot \left(1 - \frac{t_L + t_T}{t_g}\right) \quad (4.22)$$

$$V_s = \frac{4}{3}\pi r_s^3 \quad (4.23)$$

Where r_s is the radius of the spherical void and V_s is the volume of that same void. On the other hand once the competitive number is lower than 1, intra-bundle voids should be formed. These voids however are generally ellipsoidal and predominantly appear in the bundle transverse to the macroscopic flow direction.

To predict their volumes the following set of equations have been used, from which the parameters are illustrated in figure 4.7:

$$V_e = \frac{4}{3}\pi \cdot a \cdot b \cdot c \quad (4.24)$$

$$a = 0.5 \cdot L_T \cdot \left(1 - \frac{t_L + t_T}{L_L}\right) \quad (4.25)$$

$$b = 0.5 \cdot w_{bundle} \cdot \left(1 - \frac{t_{bg}}{t_{bb}}\right) \quad (4.26)$$

$$c = 0.5 \cdot h_{bundle} \cdot \left(1 - \frac{t_{bg}}{t_{bb}}\right) \quad (4.27)$$

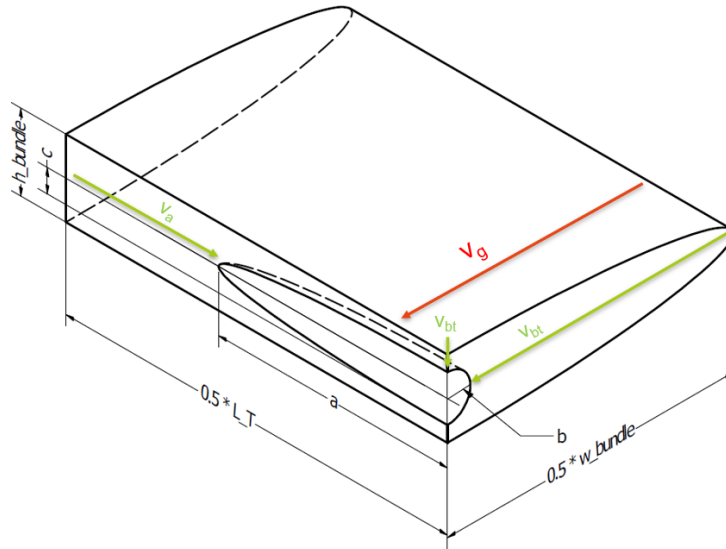


Figure 4.7: Intra-bundle void in transverse bundle as per analytical model, where v_g is the macroscopic flow, v_a is the axial intra-bundle flow and v_{bt} is the transverse intra-bundle flow.

Note that due to the complexity of the shape a couple of new parameters have been introduced. Parameter 'a' is based on the intra-bundle flow wrapping around the corner at the intersection of warp- and weft direction and it thus related to the inter-bundle length. Parameter 'b' is based on the ratio of bundle filling time due to the global flow (t_{bg}) over the intra-bundle filling time due to the intra-flow impregnating the bundle (t_{bb}) in the transverse direction, which then is multiplied by half the bundle width (w_{bundle}). Parameter 'c' is related to the bundle height (h_{bundle}) in a similar fashion. The final ellipsoid intra-bundle void shape then is displayed in figure 4.7. Where the following applies:

$$t_{bg} = \frac{w_{bundle}}{v_g} \quad (4.28)$$

$$t_{bb} = \frac{w_{bundle}}{v_t} \quad (4.29)$$

Where v_t is the transverse intra-bundle flow which is obtained in a similar fashion as the axial intra-bundle flow shown in equation 4.15, but with the transverse bundle permeability. Note that the same ratio of global filling time over bundle filling time is used in equations 4.26 and 4.27, which is based on the assumption that the propagation of the global flow into the bundle in the in-plane transverse direction should match that of the through thickness impregnation, because the global flow needs to wrap around the bundle first, before it can impregnate bundle through the thickness of the bundle.

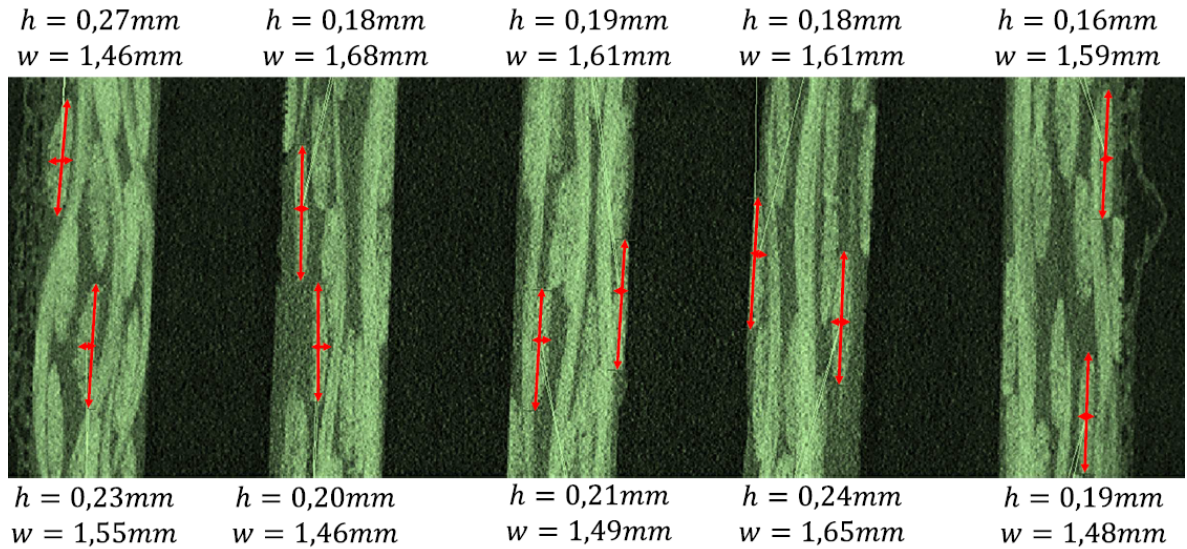


Figure 4.8: Maximum bundle widths- and height observed in micro-CT images of five different samples.

The model presented in this section can be used to approximate both voids in the intra-bundle domain and voids in the inter-bundle domain at high- and low capillary number conditions respectively. As the main research question is focused on the effects of bundle porosity on the void formation behavior, two different geometry simplifications are present in the model, which are both illustrated in figure 4.9:

- Constant Cross-sectional model (ccs): In this model the cross-sectional geometry is kept constant and is based on experimentally observed maximum height- and width averages as can be seen in figure 4.8. This geometry model's function is that it scales the porosity with the fiber volume fraction and therefore changes in intra-bundle (Gebart) permeabilities can be compared to those of global permeability changes due to fiber volume fraction (or global porosity) changes.
- Scaled geometry model (sgm): In this model the combination of fiber volume fraction and bundle porosity determines the final cross-sectional geometry. With this model it is possible to detach the influence of the bundle porosity on void formation from that of the influence global fiber volume fraction on void formation. This is an important quality as the global permeability is generally related to the fiber volume fraction of the preform, as per the Kozeny-Carmen relationship [10] for example, which does not account for the influence and therefore interplay between of variations in the bundle porosity at a constant global fiber volume fraction. Therefore to properly investigate the influence of the bundle porosity on void formation, bundle porosity- and global porosity effects need to be detached. Note that that means that in this model it is assumed that the bundle-porosity at a constant fiber volume fraction does not influence the global permeability, as it is assumed that decreased bundle porosity at a constant fiber volume fraction, requires a smaller bundle cross-section and thus larger free flow domains, which should compensate for the decreased bundle porosity.

A final remark on this model is on the global permeability - fiber volume fraction relationship. To determine the global permeability based on the fiber volume fraction, two different functions have been presented, being an exponential function fit and a Kozeny-Carmen-relationship based datafit. These two functions have been both fitted to two sets of data, one experimentally based dataset and one based on literature and those datafits will be discussed later. However, the Kozeny-Carmen fit to the experimental data will eventually be used to investigate the bundle porosity - void formation effects (raw data in Appendix B).

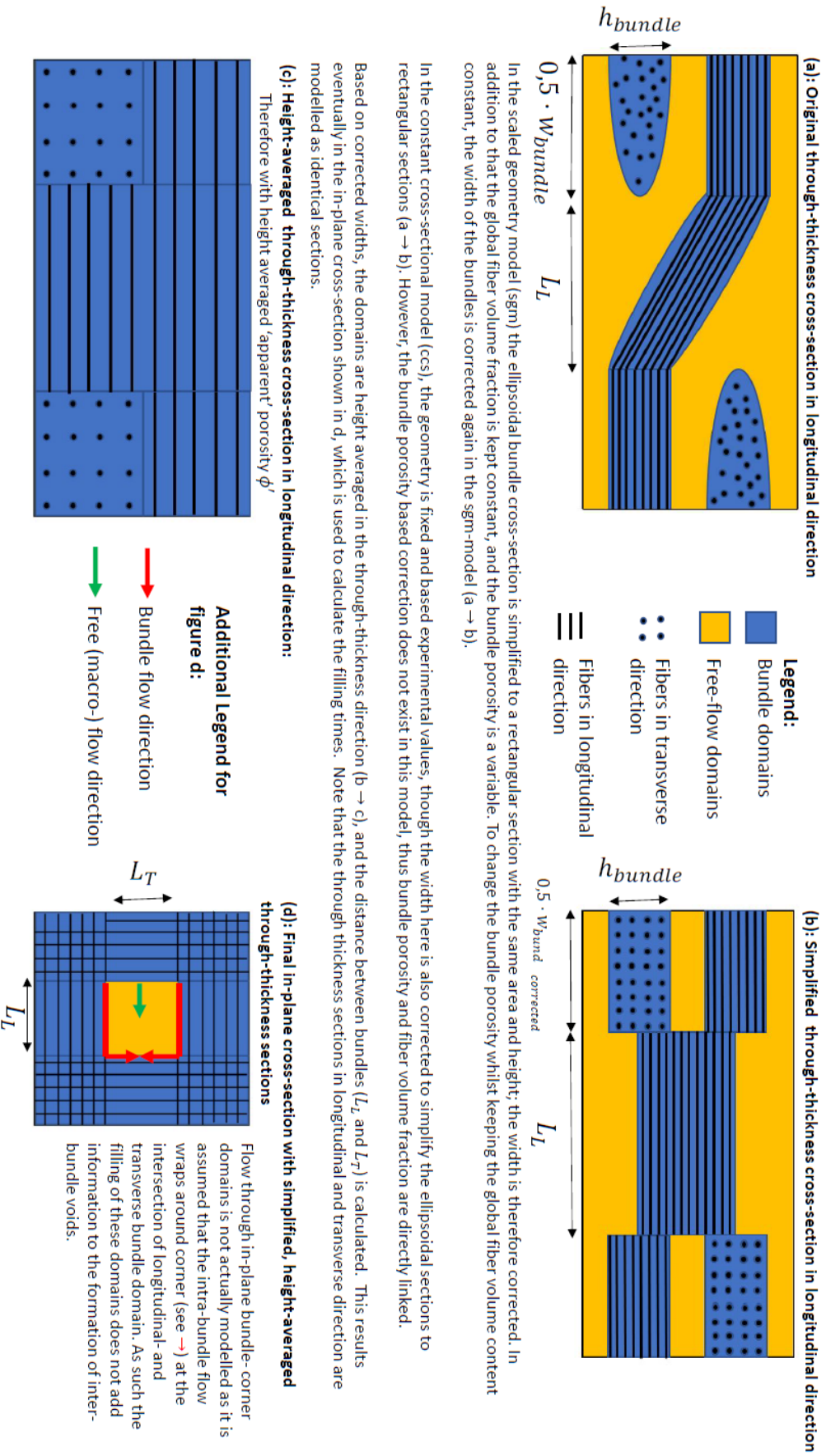


Figure 4.9: Geometry simplifications

Chapter 5

Experiments

In this chapter the experimental set-up, materials, manufacturing procedure and experimental methodology will be presented. The goal of the experimental set-up is to observe the different void formation mechanisms (mechanical air entrapment, void compression and void dissolution) and to validate the models described in the previous chapter. Fast radiation curing of an UV-curing was applied to detach the effects of the individual void formation mechanisms from each other. According to Matsuzaki et al. [14], these mechanisms occur subsequently in time and by fast radiation curing it is possible to detach these from each other by effectively freezing the resin mixture during injection at a predefined location at different time steps, where the time steps are defined as:

- the flow front is at the predefined location (mechanical air entrapment; $t=t_0$)
- the flow front has just passed the predefined location (void compression; $t=t_1$)
- the flow front has reached to outlet (the injection is done) and is left in the set-up for a period of time (3 hours after full injection) so that the entrapped- and compressed air can dissolve back into the resin.

These rapidly cured samples have been analysed by micro-CT. In addition to that, the void dissolution samples were also monitored by a micro-USB camera during the injection, and the macroscopic flow behavior was captured by a regular camera set-up, as can be seen from figure 5.1. Note that samples have been taken at two different locations in order to observe both inter- as intra-bundle voids, which should aid in the validation of the models. Samples taken at the beginning of the preform (67mm from the preform edge) should show intra-bundle voids as the macroscopic flow velocity is relatively high compared to the expected capillary flow velocity, thus the capillary number should be high, indicating intra-bundle void formation. At half the preform length (200 mm from the preform edge), samples should show inter-bundle voids as the macroscopic flow velocity there is relatively low, thus the capillary number is high, which indicates inter-bundle void formation. The analysis of these observations however, will be discussed in the next chapter.

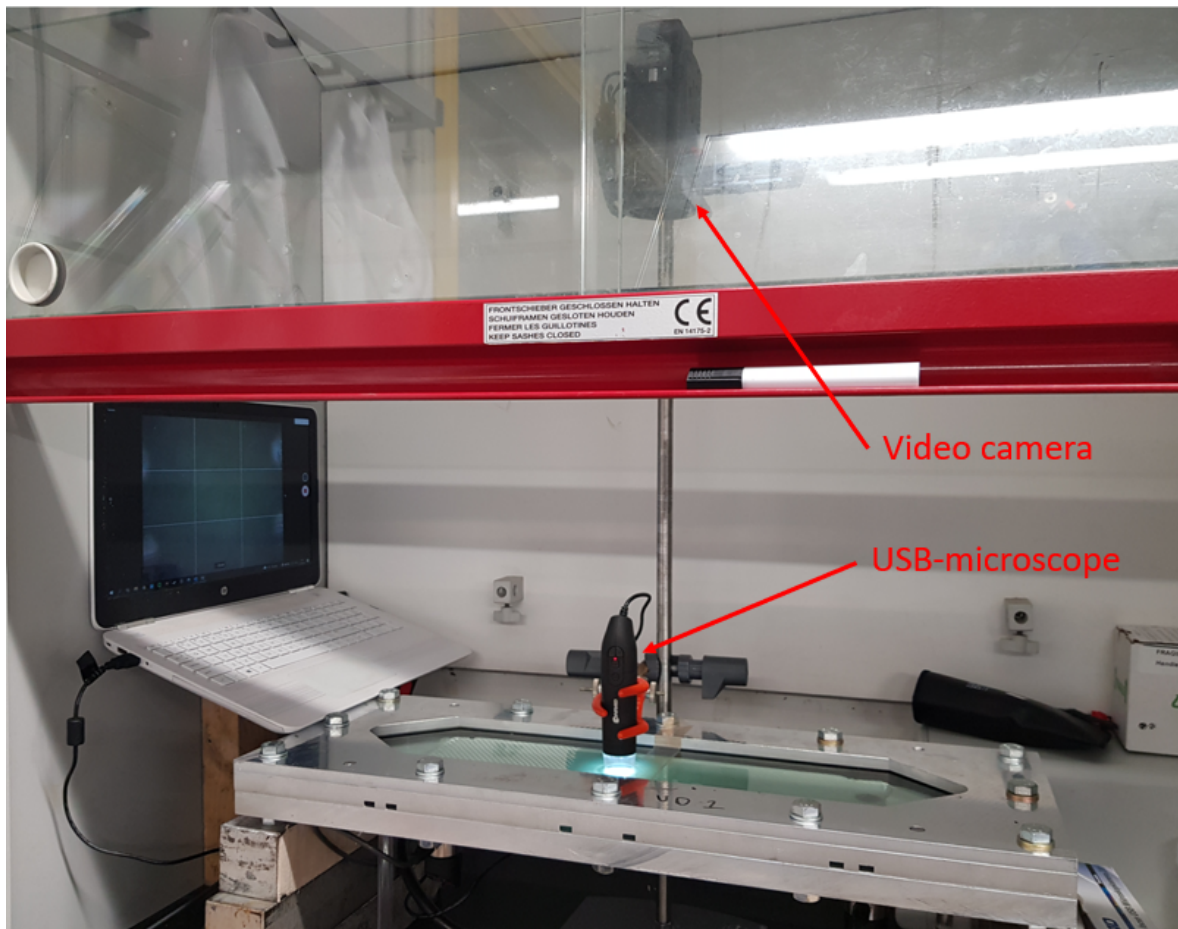


Figure 5.1: Video-camera and USB-microscope in set-up.

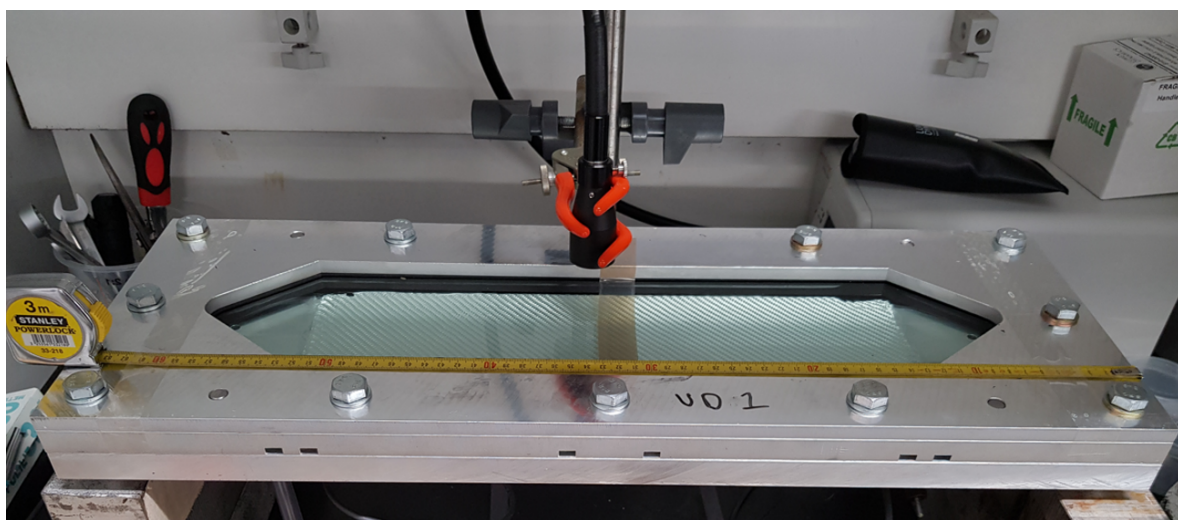


Figure 5.2: UV-lamp in set-up.

5.1 Experimental set-up

The experimental set-up used in this research is illustrated in figure 5.3. By applying vacuum pressure, the resin will be transported through the inlet, into the porous preform and towards the outlet, where excess resin will be caught in the vacuum chamber to avoid it from entering the vacuum pump. To fix the fiber volume fraction for a certain number of plies, the lower spacer was designed with a thickness of 1.0 mm. The upper spacer was designed separately to make a modular system in which only the lower spacer needs to be changed in order to change the specimen thickness. The thickness of the upper spacer is chosen just a bit larger than that of the glass plate, to ensure that the glass plate does not make hard contact with the upper mold plate and crack. To properly compress the specimen a rubber plate was placed on top of the glass plate to account for irregularities in both the glass plate as the upper mold, to avoid cracking of the glass plate induced by stress concentration formed by irregularities in the machined parts. Note that all the machined parts are made from AL6061.

Hard contact between the glass plate and the lower spacer however, needs to be ensured, as the final thickness of the specimen strongly relates to the fiber volume content and the fiber volume content has a relationship with the permeability of the fabric (see figure 5.4 [10]). The relationship can be approximated with the Kozeny-Carman relationship:

$$K(V_f) = \frac{R^2 (1 - V_f)^3}{4k V_f^2} \quad (5.1)$$

Where, K is the permeability, V_f is the fiber volume fraction, R is the fiber diameter and k is the Kozeny constant.

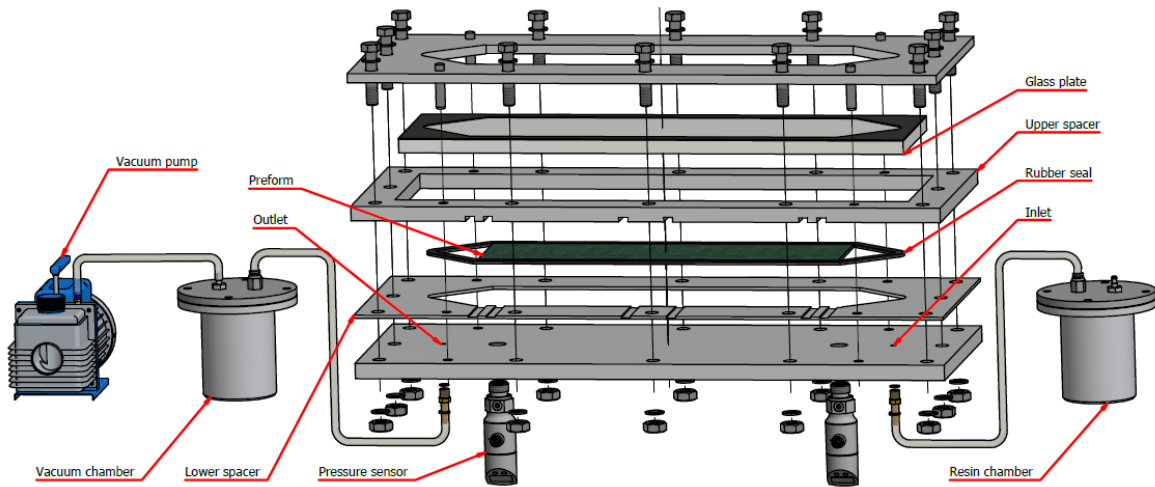


Figure 5.3: Experimental set-up excluding UV-lamp, camera and USB-microscope

Where the fiber volume fraction can be determined based on the areal weight (A_w), the number of plies (N), the fiber density (ρ_f) and the specimen thickness (T_b):

$$V_f = \frac{N \cdot A_w}{\rho_f \cdot T_b} \quad (5.2)$$

The maximum allowable error in the global permeability was set at 2%, which deemed to occur at the center of the plate due to pressure induced deflection under the assumption that the parts were machined with great precision. A 15 mm thick glass plate was capable of meeting the deflection induced permeability error criterion as calculated by classical plate theory.

The function of the glass plate is that it will allow flow-front tracking on the macroscale by a regular camera set-up as indicated in figure 5.1, which can be combined with the Balluff BSP00ZK pressure sensors sunk into the bottom mold to perform global permeability measurements by linear injection as defined in the work of Vernet et al. [25], which is needed in the modelling phase to model the macro-flow and therefore pressure distribution over the specimen area, which is limited due to the maximum specimen sizes of the micro-CT scanner. Also the transparent top mold allows for meso-scale video analysis of mechanical air entrapment at the surface via USB-microscope (also shown in 5.1). In addition to that it also has a reasonable transparency for UV-A light (approximate transparency of 65% over the UV-A domain for a Soda-lime glass plate [29]), which is needed to cure the UV-curable resin system. From initial experiments it turned out that the transparency of the glass plate indeed was high enough to allow light emitted by a Omnicure S1500 UV-lamp (shown in figure 5.2) to cure the UV-curing resin system up to 1.5 mm thickness, and thus suitable for intended 1.0 mm thick samples as defined by the lower spacer. The exact details will be presented in the curing procedure of the UV-specimen in the next section. The main benefit of using an (soda-lime)glass plate over other transparent plate materials is the stiffness. An alternative for example would be PMMA, but that would require external stiffeners to reach the acceptable deflection criterion, which also would hinder flow front tracking and UV-curing underneath the stiffeners.

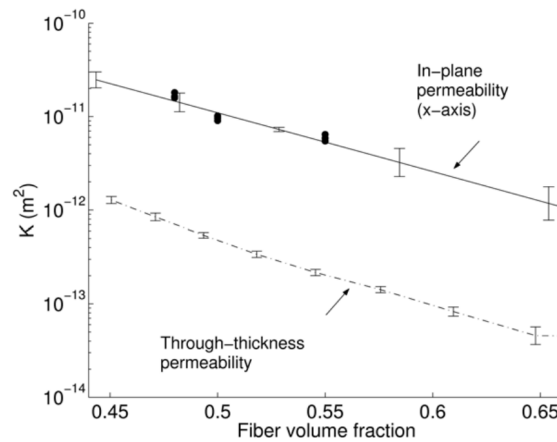


Figure 5.4: Permeability versus fiber volume content [10]

5.2 Materials

The samples will be made from a 2x2 twill weave glass fabric and the same resin mixture used in the work on capillary phenomena by Çağlar et al. [11]. The UV-curable resin system consists of three components, being a cycloaliphatic epoxy resin (Omnilane OC1005), a blend of an iodonium salt and a propylene carbonate as photoinitiator (Omnicat 250) and isopropyl thioxanthone photosensitizer (Genocure ITX). The chemical structures of these components are shown in figure 5.5 [11]. The photoinitiator allows epoxy molecules to polymerize when radiated with UV-light in the UV-C (wavelengths ranging from 100 to 280 nm) and UV-B (wavelengths ranging from 280-315 nm) spectrum, however has almost no absorption in the UV-A (wavelength ranging from 315- 400 nm) spectrum. As the UV-curable resin system is to be used in an RTM set-up, UV-light needs to be transmitted through an transparent upper mold. Two options were considered as mentioned earlier for the transparent mold, being PMMA and soda-lime glass. For both PMMA [11] as soda-lime glass [30] the transparency for UV-B and UV-C light is very low, therefore the combination of resin system and transparent mold would not be suitable. Çağlar et al. [11], therefore added a photosensitizer to the resin system, which effectively shifts the absorption spectrum to the UV-A spectrum. In this range of wavelengths the transparency of PMMA and soda-lime glass is sufficient to let enough UV-A light pass through, which then can be absorbed by the resin-system, leading towards polymerisation. Note however, that as the system polymerises, that the transparency reduces. Meaning that in practise the curing thickness of the system is limited as the radiated, and therefore polymerised, surface increasingly absorbs light needed for through-thickness curing. In addition to that, through thickness transparency is also hindered by the reinforcing material, which in this study is a 2x2 twill weave E-glass fabric. As the of cure-dependent transparency related to through thickness light absorption is difficult to determine up front, the maximum achievable curing thickness in this study was determined by trail and error, and was found at 3 uncompressed layers of fabric with a thickness of approximately 1.5mm.

The resin mixture used in this study will be the same as that used in the study by Çağlar et al. [11], being 96 wt% epoxy resin with 3 wt% photoinitiator and 1 wt% photosensitizer and was mixed in a speedmixer (SpeedMixer - DAC 400.2 VAC-P LR) for ten minutes (2 minutes at 800 rpm, 2 minutes at 1400 rpm and 6 minutes at 2300 rpm in a symmetric pyramid cycle). Also the same glass fabric will be used in this research as in the work of Çağlar et al., which is a 2x2 twill weave E-glass fabric with an areal weight of 390 g/m^2 , and uncompressed thickness of 0.45mm, and a bulk density of $\rho_{bulk} 2.6 \text{ g/cm}^3$, 6.0 ends/cm in warp direction and 6.7 picks/cm in weft direction. These fabrics will not be corona treated however.

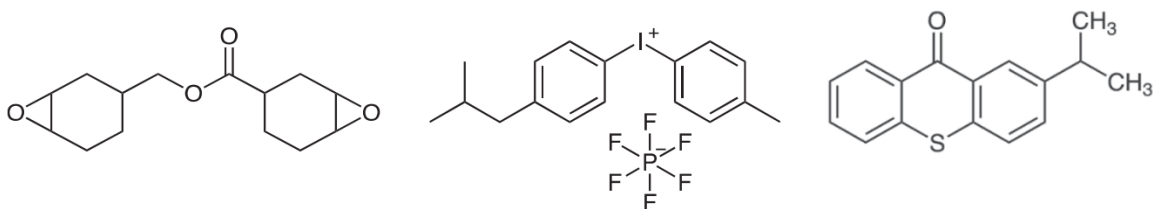


Figure 5.5: Components in UV-curable resin system; Omnilane OC1005 (left), Omnicat 250 (middle) and Genocure ITX (right) [11]

5.3 Characterisation of resin mixture

The viscosity of the resin mixture described in the previous subsection, was measured with a Peltier Couette setup in a ThermoFischer Haake Mars III rheometer, where the measurement were performed between $15^{\circ}C$ and $30^{\circ}C$ with a $0.1^{\circ}C/min$ temperature ramp and a constant $10 s^{-1}$ shear rate, identical to the measurements performed in the paper of Çağlar et al. [11]. Based on that measurement an Arrhenius curve was fitted to the data (see appendix C), resulting in the following relationship between temperature and viscosity:

$$\eta(T) = A * \exp\left(\frac{-Ea}{RT}\right) \quad (5.3)$$

Where R is the universal gas constant in $J/(mol \cdot K)$, A is the Arrhenius factor (fitted at $1.475e^{-12} Pa \cdot s$) and Ea is the activation energy (fitted at -63.87 [kJ/mol]). From figure 5.6 it can be observed that the fitted Arrhenius function corresponds well to the experimental data and that the behavior is similar to that found in literature [11].

In addition to the viscosity measurements, the surface tension and contact angle between a glass plate and the resin mixture were measured with a KSV Instruments CAM 200 drop shape analyzer and were found to be the following (see Appendix D):

- $\gamma = 26.5 \pm 6.2 mN/m$
- $\theta = 30.9 \pm 4.6^{\circ}C$

Note that the contact angle between the glass plate and resin mixture will be different from the actual glassfiber - resin mixture contact angle. However, when using the capillary pressure formulation referred to by Michaud [8] (equation 4.11), the capillary pressures determined with the measured values will be comparable to those found by Çağlar et al. [11] due to the reduced contact angle which compensates for the reduced surface tension. Measurements were done based on the pendant drop- (surface tension) and sessile drop (surface tension and contact angle) method.

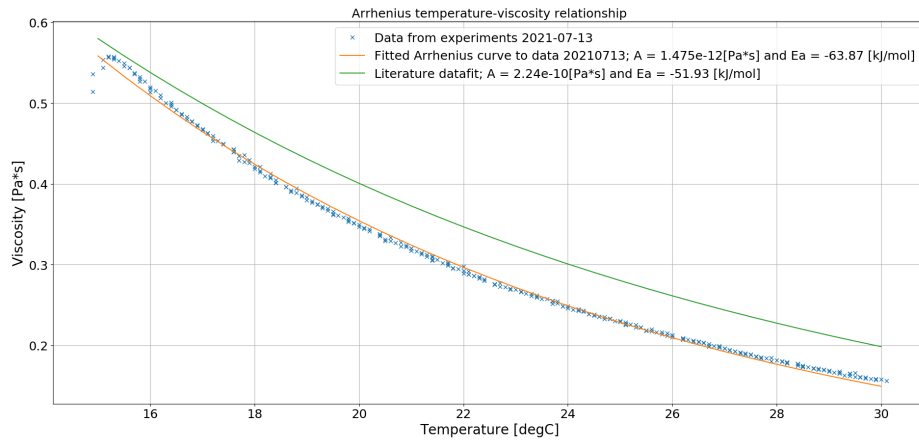


Figure 5.6: Viscosity measurements; literature datafit from Çağlar et al. [11]

5.4 Sample types and injection procedure

The injection procedure was the same for all samples. A vacuum pump was connected to the outlet and manually set to 50kPa absolute pressure as measured by the manometer connected to the pump. This resulted in a total pressure drop from inlet ($P_{inlet} = 1atm$ absolute pressure) to flow front ($P_{outlet} = 50kPa$ absolute pressure) of approximately 51.3 kPa. The two Balluff BSP00ZK pressure sensors were used to monitor the pressure drop over the preform over time and a typical graph is shown in figure 5.7, which corresponds well to the predefined 51.3 kPa pressure drop.

Two different sets of samples were be manufactured; being low capillary number samples (lCa; 200 mm from the preform edge) and high capillary number samples (hCa; 67 mm from the preform edge). The main difference between these samples is the location at which the sample is taken, which results in different ratio's of macroscopic- over capillary flow (quantifiable by the capillary number), and thus different void types, which is indicated in figure 5.8.

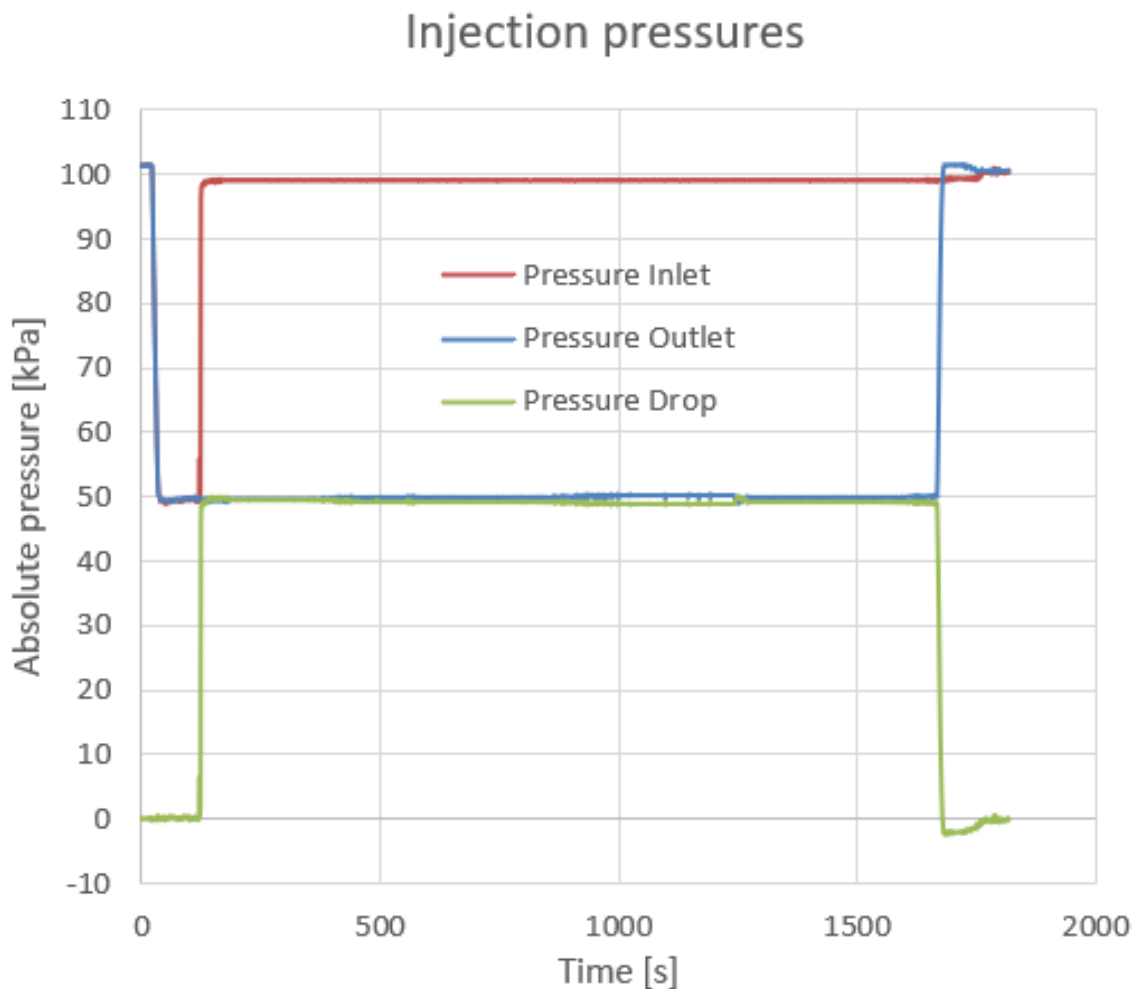


Figure 5.7: Typical pressure measurement during injection by two Balluff BSP00ZK pressure sensors (Void dissolution sample 2)

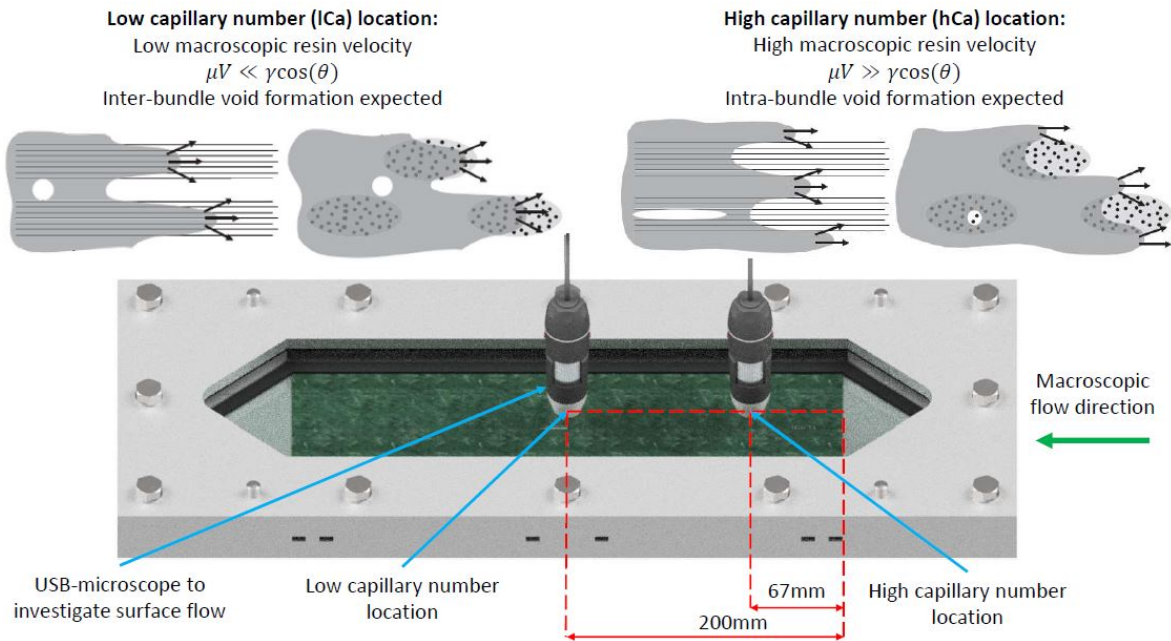


Figure 5.8: Location at which surface flow is investigated by USB-microscope and where the resin is spot-cured at different times during the injection. At the high capillary number location the macroscopic flow is dominant over the capillary (intra-bundle) flow, thus resulting in intra-bundle voids. At the low capillary number location the capillary (intra-bundle) flow is dominant over the macroscopic flow, thus resulting in inter-bundle voids. Illustrations on flow behavior and void formation adapted from the work of Mehdikhani et al. [2].

The lCa-samples are taken at 20 centimeters from the beginning of the preform. At this location the macroscopic flow is relatively slow as the applied pressure drop between the beginning of the preform and the flow front (51.3 kPa) is taken over 20 centimeters and thus the pressure differential locally is low; assuming a linear pressure drop between the beginning of the preform and the flow front, the pressure differential is about 2.5 kPa/cm. The capillary pressure at this location however, will be higher than the applied pressure differential. This higher capillary pressure is assumed to result in a larger flow velocity inside the bundles (capillary flow), than outside the bundles (macroscopic flow) and therefore inter-bundle voids should appear at this location. To investigate void formation mechanisms, three different types of specimens are taken within this sample set, being mechanical air entrapment samples, void compression samples and void dissolution samples. The difference between these samples is the following:

- Mechanical air entrapment samples: The spot cure is made at the flow front once the flow front reaches the predefined spot at 20cm from the beginning of the preform. These samples will be referred to as flow front (FF) samples
- Void compression samples: The spot cure is made once the flow front just passed the predefined area at 20 cm from the beginning of the preform. These samples will be referred to as void compression (VC) samples.

- Void dissolution samples: The spot cure is made 3 hours after full impregnation of the preform. Note that the injection time however, is considerably shorter; approximately 30 minutes. To stop the macroscopic flow after full impregnation of the preform the outlet pressure is increased to 1 atm so that the pressure differential over the preform reduces to zero, and thus the flow stops (pressure cycle of a void dissolution sample shown in figure 5.7). After the flow is stopped the specimen will stay inside the mold while the resin is still viscous for about three hours in which void dissolution is supposed to occur. After three hours the spot cure at the predefined spot will be made. Note that to observe void dissolution, the resin needs to be degassed prior to the injection. If not, the resin is saturated at 1 atm and therefore once the pressure is released (resin pressure returns to 1 atm absolute pressure), gas dissolution could not be observed as the resin is already saturated. Degassing prior to injection will result in an injection with a unsaturated resin. Therefore voids formed during the injection should dissolve back into the resin. To degas the resin, the resin is placed inside a vacuum chamber for 2 hours and a vacuum pressure of -80kPa is applied. In addition to that a piece of Scotch-Brite tape is placed at the bottom of the resin container to locally reduce the nucleation energy to form a bubble. Bubbles nucleated on the tape then will rise through the matrix, grow by air diffusion into the bubble and then evacuate the resin at the surface. The applied degassing time was based on visual inspection of the resin during degassing and monitoring the bubbles present in the resin, on the degassing agent and on the surfaces of the container over time and it was found that the bubbles had reached a steady state size after 1 hours and 45 minutes. The set-up used to degas the resin is displayed in figure 5.9. Void dissolution samples will be referred to as VD-samples.

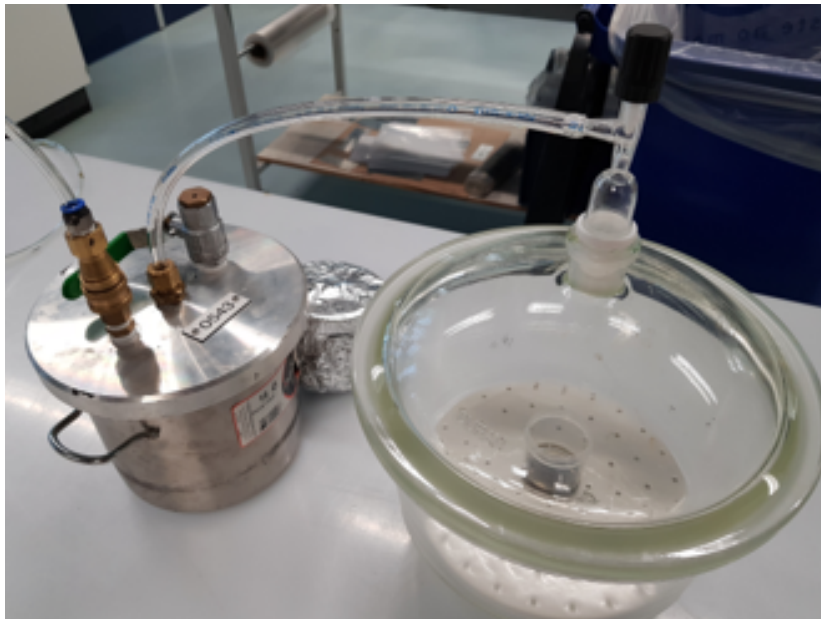


Figure 5.9: Degassing set-up; -80kPa vacuum pressure for two hours with Scotch Brite tape as a bubble nucleation agent.

In addition to the lCa specimens, hCa specimens were produced, which are taken from the beginning of the preform; approximately 6.7 centimeters from the preform edge on the inlet side. At this location the capillary number is assumed to be rather high as the macroscopic flow velocity is large as the pressure drop between is taken over a distance of only 6.7 centimeters, thus the pressure differential is relatively large. For the hCa specimens, only void compression samples have been produced as the macroscopic flow velocity was too high to properly produce mechanical air entrapment samples, and because void dissolution samples were assumed not to give additional information relative to the lCa-specimens with respect to answering the research question. The goal of the lCa-VD samples was to proof that void dissolution occurs over a much longer timescale than the other void formation mechanisms and thus can be neglected in the semi-analytical model presented in section 4.3 as they will be compared with rapidly cured samples in which the voids would not have had time to dissolve back into the resin. As the capillary number is assumed not to influence void dissolution, manufacturing of hCa-VD samples therefore was deemed redundant.

The samples created with the procedures described above were cut to size after cure with a diamond cutting blade on a water cooled Secotom 10 cutting machine to obtain clean edges without introducing defects in the samples (e.g. cracking of matrix or delamination of the laminate). Two different sets of samples sizes were made, being 30 mm squared samples for micro-CT scans with a resolution of 15 μm , and 7 mm squared samples for micro-CT scans with a resolution 5 μm . Based on these samples, void types and sizes could be investigated for the different specimen types, and could be investigated by micro-CT analysis. The results will be presented in the next chapter.

5.5 Curing Procedure

An Omnicure S1500 UV spot curing system with an 8 mm diameter lightguide connected to an collimating adapter to increase the cure area to spot with a 30 mm diameter, will be used to cure the resin system by fast-radiation curing. Short curing cycles have been investigated (single pulses of 1 s), which indicated that the resin system was no longer viscous, which therefore implies split second flow freezing. However, to ensure proper polymerization throughout the thickness, 60 second curing cycles have been applied at the curing zone. The actual radiation levels were not measured, but due to the similarity in curing procedure in the work of Çağlar et al. [11], it is assumed that similar radiation levels (41.1 mW/cm^2) will have occurred leading to proper polymerization of the specimen.

5.6 Experimental methodology

Based on the methods described in the previous sections, different types of samples have been produced. The samples have been monitored during the injection and cured samples have been analysed by post-processing micro-CT scans. Different types of measurements/observations were made during the experimental phase. In table 5.1 an overview of the samples and their experimental-settings used for further analysis in this report is displayed.

Table 5.1: Samples used for further analysis. In the 'used for' column, the analyses performed on a specific sample have been listed. Here 'GPD' stand for global permeability determination, 'CD' stands for cross-section definition, 'VS' stands for void size determination by post-processing of micro-CT scans and 'ST' stands for surface tracking at predefined location by USB-microscope.

Sample name	Location of sample	Average temperature during injection	Applied pressure drop	Micro-CT resolution	Used for
FF5	lCa	21,56 °C	51,3 kPa	15 μm	GPD, CD
FF6	lCa	21,7 °C	51,3 kPa	15μm	GPD, CD
FF7	hCa	-	51,3 kPa	15 μm	CD
VC2	lCa	19,67 °C	51,3 kPa	5 μm	GPD, VS
VC3	lCa	22,8 °C	51,3 kPa	15 μm	GPD, CD
VC4	hCa	-	51,3 kPa	5 μm	VS
VD1	lCa	20,75 °C	51,3 kPa	15 μm	GPD, CD, ST
VD2	lCa	22,9 °C	51,9 kPa	-	GPD, ST

5.6.1 Global permeability determination (GPD)

During the injection the macro-flow propagation was captured by a regular camera set-up, which is shown in figure 5.1. The injection set-up was designing for a linear injection of the rectangular preform. To determine the global axial permeability of the preform, the location of the flow front was tracked visually over time. From figure 5.10 it can be seen that a measuring tape was aligned with the flow direction. This measuring tape, as well as the entire preform were within view of the video camera. The measurement started once the flow front reached the beginning of the preform, and the time between every 2 centimeters of flow front propagation was recorded. Note that the flow front shape was not perfectly uniform, thus the measurements were taken along a single line along the flow direction parallel to the sides of the mold. This line was placed at a somewhat arbitrary location along the width of the preform, where the behaviour was deemed to be representative for the macro-behavior; not too close to the seal as there the mesoscale geometry might either be compressed too much by seal (leading to a local reduction in the flow velocity) or once not properly aligned with the seal (or improper stacking at the edges) not compressed enough (leading to race tracking and thus increased flow velocity along the seal), and also not directly above the pressure sensor as this appeared to induce some effects as well as it is not perfectly flush with the mold surface. It was observed that the non-uniform flow front shape was introduced at the very start of the impregnation, but that it did not change considerably during further propagation, indicating

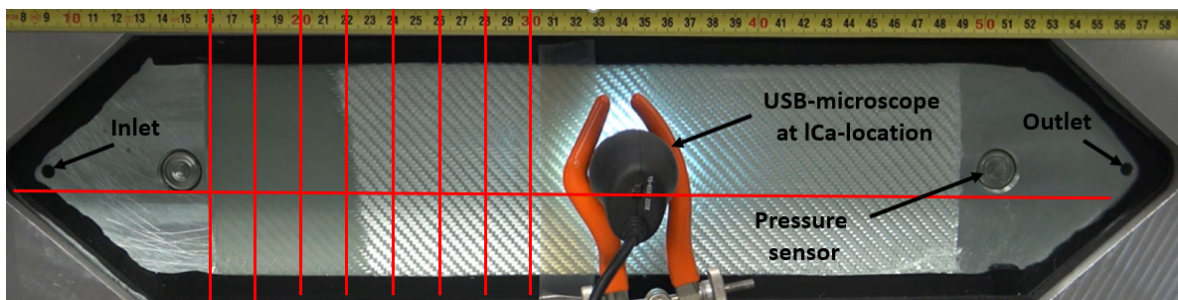


Figure 5.10: Non-uniform flow front shape during injection

that the more important flow front propagation was uniform during the injection. As such it was assumed that monitoring the flow front propagation along a single line indeed was reasonable. The data collected by this methodology is presented in appendix E. Based on the collected data it was possible to determine the global axial permeability of the preform based on the methods presented by Vernet et al. [25]. The results of this analysis will be discussed in chapter 7 along side with the validation of the macro-flow model.

5.6.2 Void size determination (VS)

Average void sizes were determined based on post-processing of micro-CT scans in Thermo Scientific Amira-Avizo Software. These images have been post-processed by multi-level thresholding based on greyscale intensities to obtain three distinguishable phases, being air, resin and fibers. In addition to that a majority filter has been applied to filter out numerical artifacts by rejecting voids below a volume of $3 \times 3 \times 3$ voxels, however some artifacts remain inside the images as increasing the majority filter would also lead to a loss of the actual void sizes in the analysis. The air-phase then was filtered out and individual void sizes were obtained. The average void sizes obtained by this method were used in chapter 7 to validate the semi-analytical meso-flow model.

5.6.3 Cross-section definition (CD)

The Thermo Scientific Amira-Avizo Software allows for manual geometrical measurements of micro-CT images. To obtain the average dimensions of the bundles on the mesoscale, an arbitrary plane in the through-thickness direction of a couple of samples was investigated, and multiple bundle dimensions along this plane were recorded (see figure 4.8). The average of these measurements were used as input for the semi-analytical meso-flow model described in section 4.3.

5.6.4 Surface tracking (ST)

The void dissolution samples did not require rapid radiation curing during impregnation of the preform. As such, it was possible to replace the UV-lamp by an USB-microscope during the injection and investigate the surface flow on the mesoscale during the injection. The USB-microscope was placed directly on top of the transparent upper mold and videos at both the lCa- and hCa-locations were made during the injections. In addition to that the microscope was also used to monitor void dissolution at the lCa-location over a period of 3 hours, where a snapshot was taken every ten seconds. The observations made by the USB-microscope will be presented in the next chapter.

Experimental observations

In this chapter the theory on void formation mechanisms will be checked based on microscopy and micro-CT imaging, for which the analysis methodology is presented in section 5.6. Surface flow was captured by microscopy to investigate mechanical air entrapment, void compression and void dissolution at the surface of the specimen. Micro-CT scans were used to investigate the average sizes and locations of voids for both the high- and low capillary number (void compression) samples.

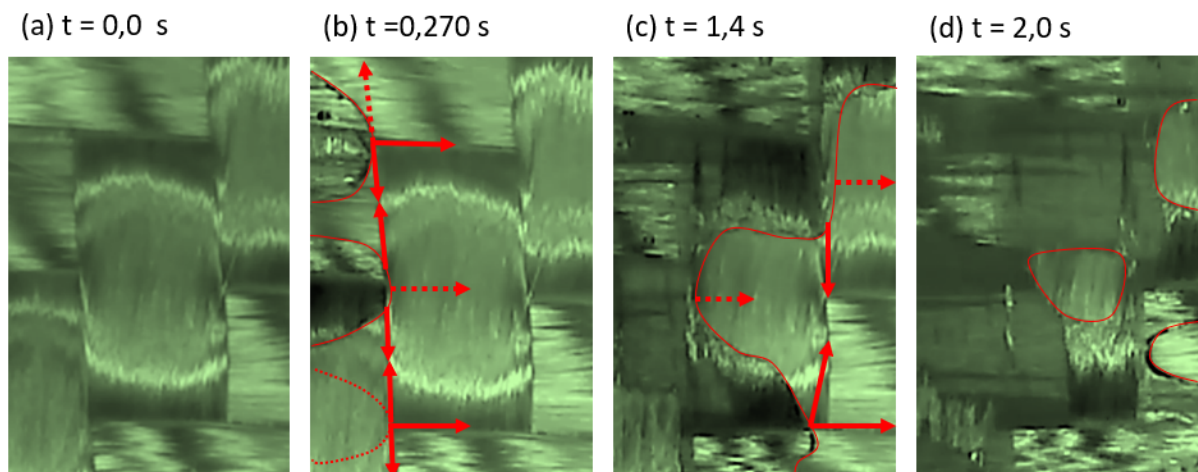


Figure 6.1: Subsurface mechanical air entrapment and void compression for a high capillary number sample (VC4). The lines indicate the flow front in the free flow domains, whereas the arrows indicate the direction of this flow front. Dotted lines indicate that the flow front will pass underneath a bundle.

6.1 Mechanical air entrapment and void compression

Mechanical air entrapment was observed with the microscope as shown in figure 6.1. From this figure it can be observed how the free flow exceeds the flow inside the bundles. The free flow domains are largest at the intersections of warp- and weft direction. These free flow domains fill faster than the bundles which are compressed by the upper mold plate. As such, resin flowing through the free flow domains, wraps around the air in the bundles, effectively entrapping it. This also occurs in through-thickness direction (not visible in the figure) and therefore eventually the void cannot be observed at the surface. However, it should be present in the bundle itself. The entrapment predominantly takes place in the bundles transverse to the flow direction as the transverse permeability is lower than the axial permeability of a bundle due to the alignment of the fibers and thus the obstruction of the flow.

From figure 6.2 it can be observed that voids indeed are observed within the bundles and that they predominantly exist in the transverse bundles. These voids have an ellipsoidal shape which matches with intra-bundle void shapes described in literature [21]. The spherical voids are assumed to be introduced during the injection where the manual opening of the valve introduces turbulent flow encapsulating air and forming spherical voids which then travel along the flow through the free flow domains (these voids have been observed by video analysis stemming from the inlet).

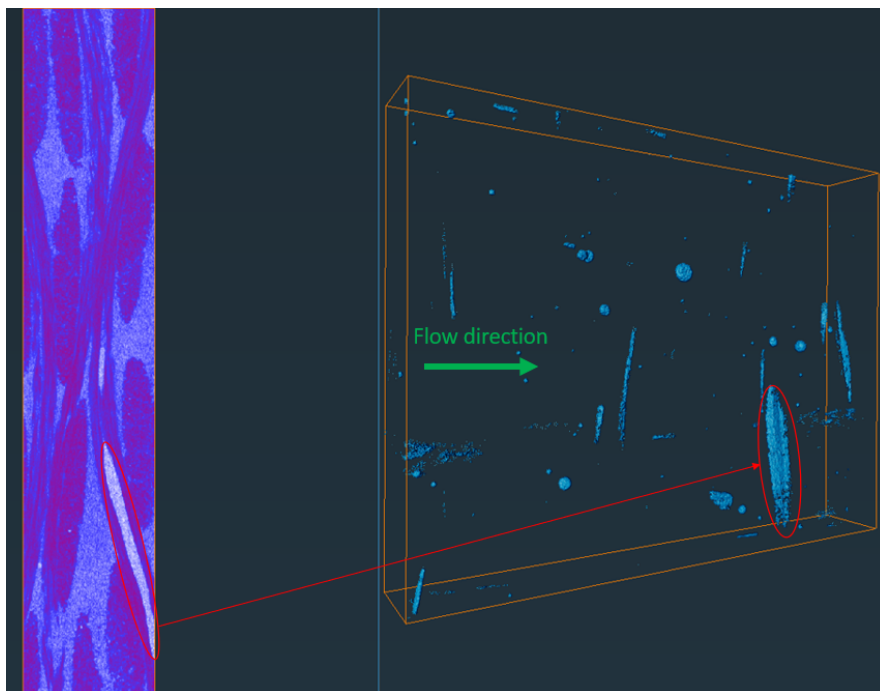


Figure 6.2: Micro-CT image of hCa-VC specimen (VC4) indicating intra-bundle void formation in transverse tows: resolution $5\mu m$. Part of the image on the left shows bundles (darker shade of blue), resin (lighter shade of blue) and entrapped air (white). Part of the image on the right indicates the voids which have been filtered out from the micro-CT images and displayed in a 3D-environment. Combining the two images indicates that voids appear in the intra-bundle domains and almost exclusively in those perpendicular to the flow direction.

Mechanical air entrapment at a low capillary number unfortunately was not captured at the surface as the free flow front was not clearly distinguishable from the intra-bundle flow front. Micro-CT scans however revealed voids entrapped in the free flow domains at the intersections of the warp- and weft direction as can be observed from figure 6.3 (where the free flow domain is largest) indicating that indeed the capillary flow has overtaken the free flow at this location along the impregnation length.

Note that a void threshold volume (0.001 mm^3) was applied to remove remaining artificial voids from the processed scans. This seemed like a reasonable threshold volume as then five voids remain which matches the five clearly distinguishable meso-voids observed in the micro-CT analysis as can be seen in figure 6.3 and it is approximately 0.1% of the modelled domain, which seemed a suitable volume for mesoscale analysis. This resulted in an average intra-bundle void volume of 0.004 mm^3 at the hCa-location, and an average inter-bundle void volume of 0.009 mm^3 at the lCa-location.

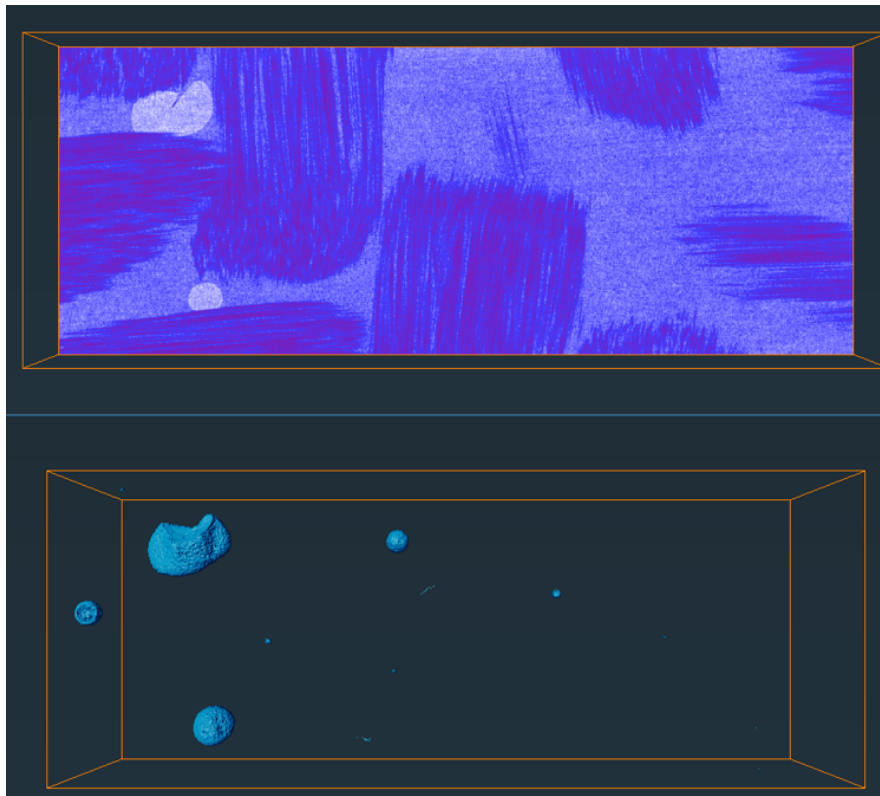


Figure 6.3: Micro-CT image of lCa-VC specimen (VC2) indicating inter-bundle void formation: resolution $5 \mu\text{m}$. Part of the image on the top shows bundles (darker shade of blue), resin (lighter shade of blue) and entrapped air (white). Part of the image on the bottom indicates the voids which have been filtered out from the micro-CT images and displayed in a 3D-environment. Combining the two images indicates that voids appear in the inter-bundle domains and almost exclusively at the intersection of the warp- and weft direction of the bundles.

These images show that the theory discussed in Chapter 3 is in agreement with the experimental results; at the domains where the applied pressure differential is considerably larger than the capillary pressure, intra-bundle voids are formed and vice-versa inter-bundle voids are formed. Therefore, it is assumed that once a model is capable of recreating these distinct void types at the correct locations, the model would be suitable for determining the influence of the bundle porosity on void formation.

6.2 Void dissolution

Void dissolution was observed at the surface by USB-microscope. Once the preform was fully impregnated, the outlet pressure was set to 1 atm, and therefore the pressure drop over the preform was zero, thus stopping the flow. At the location where the ICa-specimens were taken (at half the impregnation length) surface voids were monitored for four hours. As illustrated in figure 6.4, the voids at the surface are already almost completely dissolved into the matrix after 150 minutes, indicating that void dissolution indeed is a void mechanism that can alter the void size considerably. Micro-CT analysis of a void dissolution sample even showed that a void free laminate can be obtained with use of a resin degassing procedure prior to injection, indicating the considerable effect that void dissolution can have on void sizes.

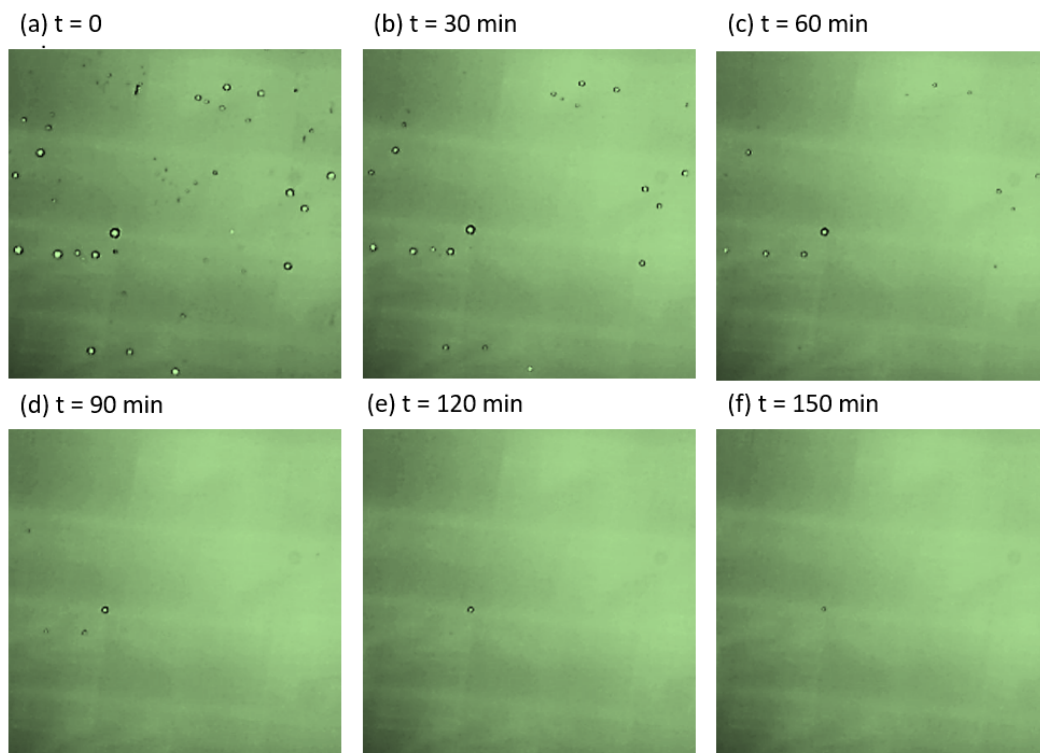


Figure 6.4: Void dissolution taken over 150 minutes at half the impregnation length of the preform (ICa-position)

The number of voids observed at the surface is tracked over time and illustrated in figure 6.5. From this figure it can be observed that the number of voids decreases in a linear fashion over time and that the void dissolution is a relatively slow process compared to mechanical air entrapment; changes in the number of voids present at the surface were only visible on the minute-scale, whereas mechanical air entrapment takes place in a matter of seconds (see figure 6.1). The assumption that void dissolution effects on the void sizes are negligible for a fast radiation cured system with a curing cycle of a minute, seems valid. Therefore it is reasonable to omit void dissolution in the semi-analytical meso-flow model described in section 4.3. A final remark to be made on the void dissolution-time curve presented in figure 6.5, is that the linear drop in number of voids does not mean that void dissolution itself is a linear process. Though linear decrease in the square of the void radius is also described by Lundström [21] (which in some way could be related to the reduction in the number of voids), it can be argued that once the resin saturates over time, that the diffusion rate decreases and thus the rate at which dissolve back into the resin. This however, was not observed in the experiments, nor was it the goal to prove that.

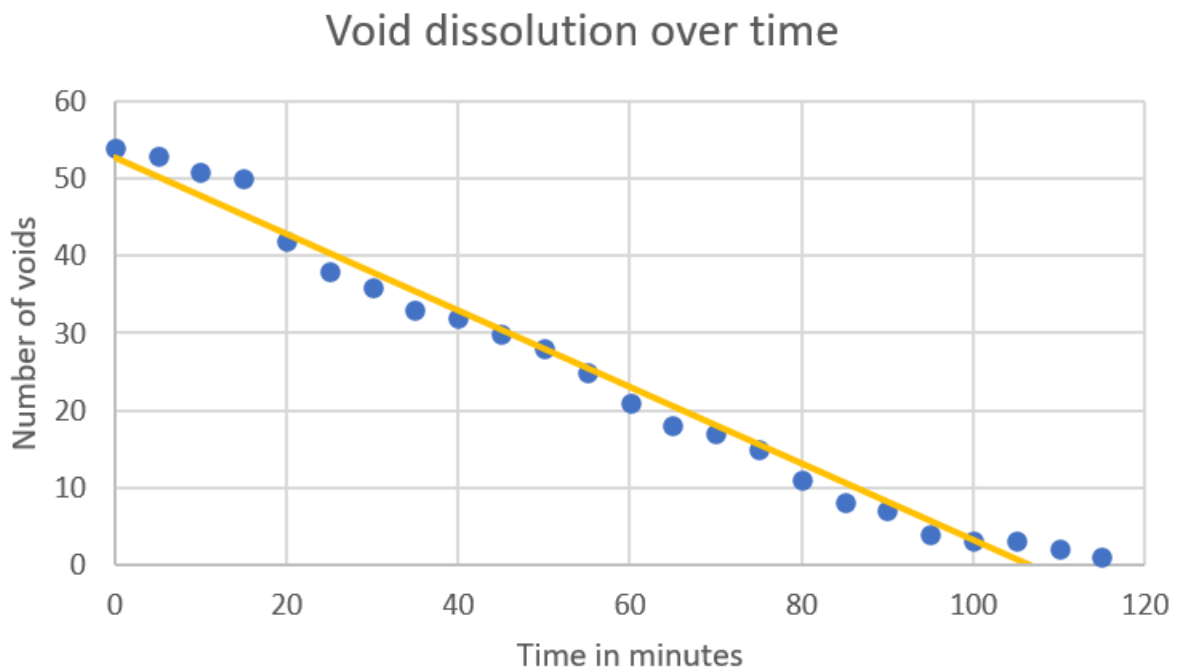


Figure 6.5: Number of voids observed at the surface by USB-microscope over time once the flow is stopped. Due to injection with an unsaturated resin, voids dissolve back into the resin over time by diffusion. A linear decrease in void-number is observed over time.

Model validation

In this chapter the 1D-Finite Element (FE) macro-flow model and the analytical meso-flow model will be validated. The FE-meso-flow model mentioned in section 4.2 will not be evaluated as no realistic results were obtained with that model.

7.1 Macro-flow model

During the experimental phase, the macro flow progression throughout the preform was monitored with a camera. Based on this data the permeability of the preform was determined based on the methodology presented by Vernet et al. [25]. In their work the permeability (K_{LSF}) was determined based on a least square fit (LSF) of the flow front location at a certain time and related to the pressure integral at that same time as per:

$$K_{LSF} = \left(\frac{\sum_{i=1}^n x_{ffi} \cdot \sqrt{I_i}}{\sum_{i=1}^n I_i} \right)^2 \frac{\Phi \cdot \mu}{2} \quad (7.1)$$

Where $x_{ff,i}$ was the location of the flow front along the preform, Φ was the volume averaged porosity of the preform, μ was the viscosity of the resin and I_i was the pressure integral defined as:

$$I_i = I_{i-1} + \frac{(P_{inj,i} - P_{inj}\lambda - 1)}{2} (t_i - t_{i-1}) \quad (7.2)$$

Five samples were analysed based on this technique and an axial permeability of $(1.48 \pm 0.17) e^{-10} m^2$ was measured for an average fiber volume fraction of 31% (raw data can be found in Appendix E). Çağlar et al. [11] used the same fabric and resin system and measured an axial unsaturated permeability of $(3.47 \pm 0.48) e^{-10} m^2$ for a fiber volume fraction of 33%, which is twice as high, but in the same order of magnitude.

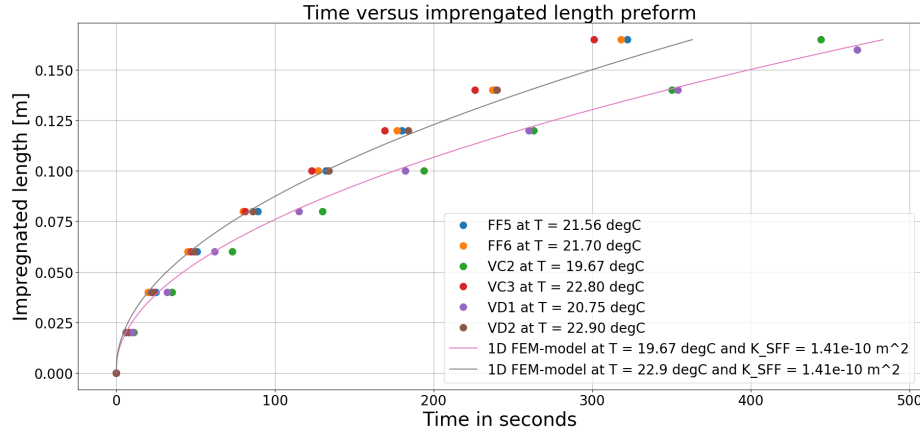


Figure 7.1: Flow front propagation based on 1D-Finite Element macro flow model and experiments. Samples have been assigned both a specimen type name and a specimen number. Here 'FF' denotes flow front-sample, 'VC' denotes void compression-sample and 'VD' denotes void dissolution-sample. The exact definition of the different sample types is described in chapter 5.

In addition to the least square fit, the squared flow front (SFF-method) approach referred to by Vernet et al. [25] was also used to determine the permeability of the preform, where the following equation was used:

$$K_{\text{SFF}} = \frac{\chi_{ff}^2 \cdot \Phi \cdot \mu}{2 \cdot P_{inj} \cdot t} = \frac{m \cdot \Phi \cdot \mu}{2 \cdot P_{inj}} \quad (7.3)$$

Using the SFF-method a similar permeability was obtained of $(1.41 \pm 0.15) \text{ e-}10 \text{ m}^2$. The difference between the two methods is small, but the squared flow front method has a lower standard deviation and is therefore used in the macro-flow analysis. To validate the macro-flow analysis based on Darcy's law, the SFF-permeability was used and plotted at two different injection temperatures as well as the experimentally observed flow propagations. The results are shown in figure 7.1 and indicate that the macro-flow model based on Darcy's law is in agreement with the experimentally observed macro-flow propagation. In addition to that, the plot shows that the measured permeability values were coherent with the flow propagation through the preform. It is assumed that the main contributor to the discrepancy between these measured permeabilities and the once measured by Çağlar et al. [11], is due to the amount of layers used. As a relatively small amount of layers (three) were used in the experimental phase, the mold effects (drag induced by the mold surfaces) are more dominant, therefore leading to a difference permeability relative to a system with extra layers. In addition to that, geometrical differences at the mesoscale can also influence the macroscopic permeability. [31] That these differences at the mesoscale exist for different number of plies stacked on top of each other at the same constant global fiber volume fraction, can be deduced from the different compaction pressure - fiber volume fraction curves presented in the work of Robitaille and Gauvin. [32] This also is assigned as one of the causes between the discrepancy between the measured axial global permeability values and those described by Çağlar et al. [11], indicating the strong effects that the mesoscale geometry can have on global homogenized properties such as the global permeability.

7.2 Meso-flow: Analytical model

The analytical meso-flow model has been compared with the average void volumes observed in the micro-CT scans for the $5\mu\text{m}$ resolution scans of void compression sample 2 (VC2) and void compression sample 4 (VC4). These void compression samples are taken at different locations at thus at different capillary number conditions. At the high capillary number site, which is when a sample is taken after an impregnation length of 67mm, an average void volume (for VC4) was observed from 0.004 mm^3 . At the location of the low capillary number site, which is when a sample is taken after an impregnation length of 200mm, an average void volume (for VC2) of 0.009 mm^3 was observed. Note that a void threshold volume (0.001 mm^3) was applied to remove artificial voids from the processed scans. This seemed like a reasonable threshold volume as then five voids remain which matches the five clearly distinguishable meso-voids observed in the micro-CT analysis as can be seen in figure 6.3 and it is approximately 0.1% of the modelled domain, which seemed a suitable volume for meso-scale analysis. The averaged void volumes are plotted alongside the meso-flow model void volumes along the impregnation length and seem to be in agreement with each other (see figure 7.2). From this same figure it can be observed that indeed high capillary numbers are observed at the beginning of the preform leading to intra-bundle voids and that the capillary number reduces during the flow propagation until intra-bundle voids switch to inter-bundle voids as the capillary flow becomes dominant. This also corresponds to the figures 6.2 (VC4) and 6.3 (VC2), where in the hCa-samples ellipsoidal voids were observed in the bundles perpendicular to the flow direction and in the lCa-samples spherical voids were observed in the inter-bundle domains.

To further validate the model, the void volumes were also plotted versus the impregnation

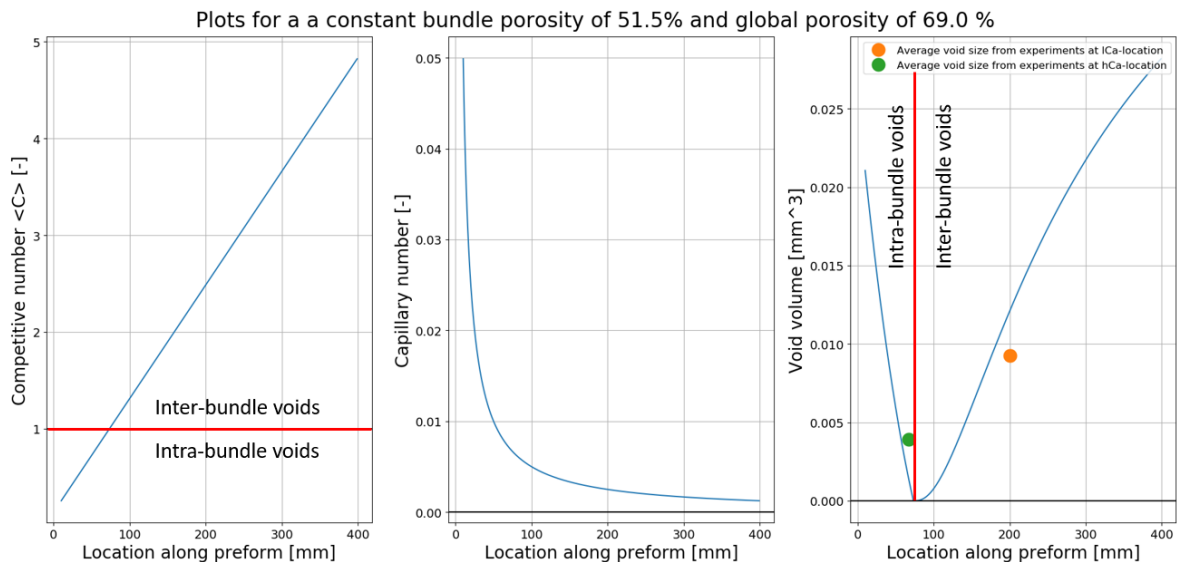


Figure 7.2: Impregnated length versus competitive number, capillary number and void volume. Note that in the graph on the right, colored dots are used to indicate the experimentally obtained void volumes, where the green dot shows the average void volume at the high capillary number location (sample VC4) and the orange dot shows the average void volume at the low capillary number location (VC2).

length, capillary number and the inverse of the competitive number, as illustrated in figure 7.3. When comparing the capillary number - void volume relationship in the middle graph from figure 7.3, with the generic graph shown in figure 3.2 [2], a similar trend can be observed: low capillary numbers result in inter-bundle voids and grow faster with a decrease in capillary number than the intra-bundle voids grow with an increase in capillary number, indicating that the model corresponds with observations from literature [2]. In addition to that the capillary number - void volume relationship (middle graph) shows the same trend as the inverse competitive number - void volume relationship (right graph).

As the model seems to provide a reasonable approximation of the void volume and the global behaviour is in line with literature (and seems logical), it was concluded that the model was good enough to quantify the tow porosity effects on void formation.

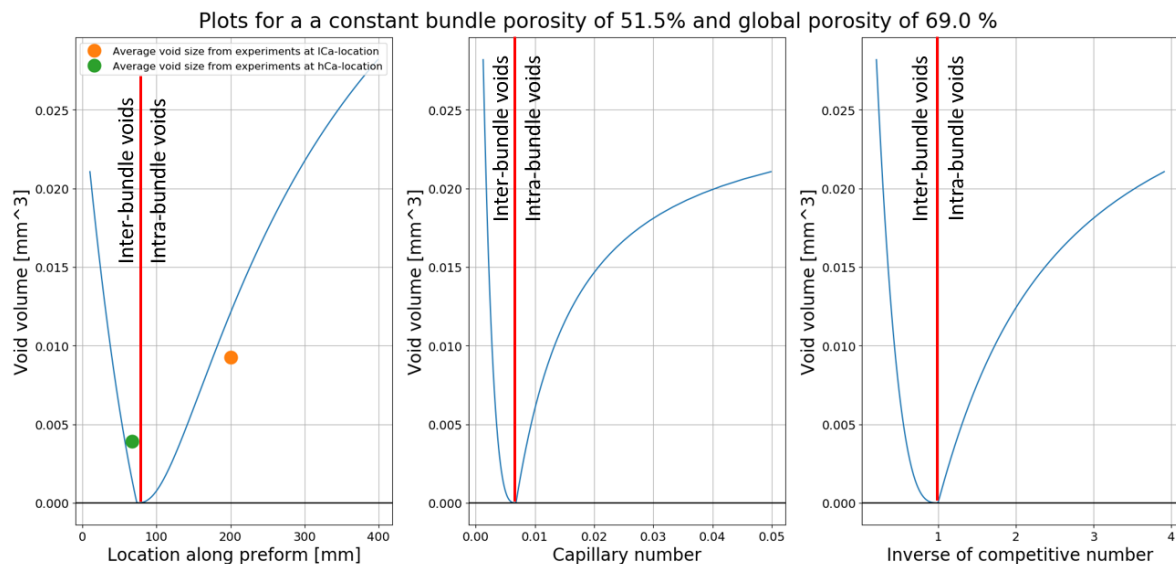


Figure 7.3: Location, capillary number and the inverse of the competitive number versus void volume. Void volumes obtained from the semi-analytical meso-flow model are plotted against the capillary number and the inverse of the competitive number. From the capillary number plot (the middle graph) it can be observed that the capillary number - void volume relationship obtained from the model is similar to that found in literature [2], thus indicating the validity of the model and thus the competitive number - void volume relationship.

Bundle porosity effects

The analytical meso-void formation model is used for the evaluation of the bundle porosity effects on void formation, where void formation is characterised by the ratio of the macroscopic flow over the capillary flow. As the macroscopic flow is directly related to the global permeability and thus the global porosity, variation in the global porosity can strongly influence the void formation process. In addition to that the global porosity of the preform is directly related to the bundle porosity and the bundle geometry. To therefore properly detach the global porosity effects from the bundle porosity effects, a model has been constructed which scales the geometry to the predefined global- and bundle porosity (the Scaled Geometry Model from section 4.3). Based on that model the porosity effects were investigated for a constant global porosity of 69% (the average 31% fiber volume from the experiments) at both the high capillary number location (at an impregnation length of 67 mm) and the low capillary number location (at an impregnation length of 200 mm).

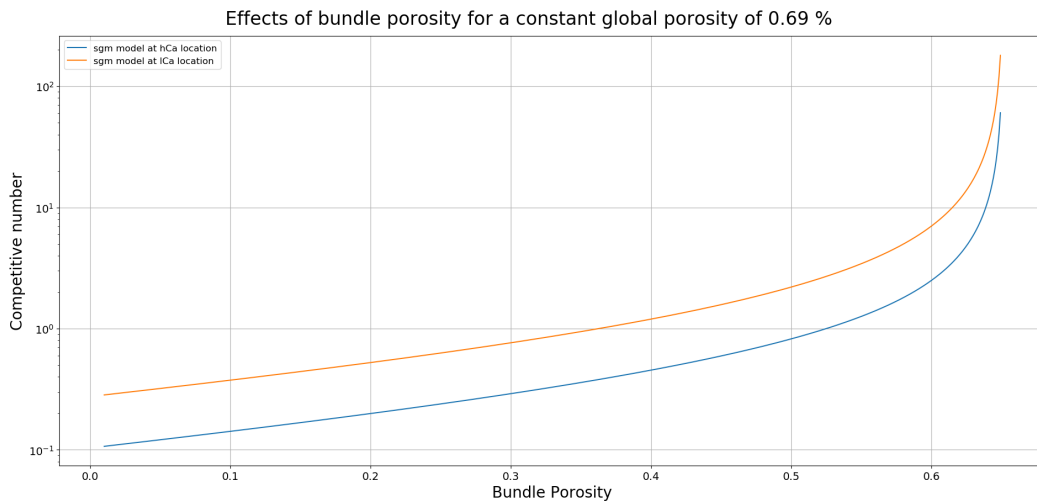


Figure 8.1: Bundle porosity effects on the competitive number

The results from this analysis are shown in figure 8.1. From this figure it can be observed that an increased bundle porosity leads to a higher competitive number, meaning that at a constant fiber volume fraction an increase in the bundle porosity will shift the void formation type from intra-bundle void formation towards inter-bundle void formation. This means that the increase in bundle permeability due to the increase in porosity is dominant over the capillary pressure reduction related to an increased porosity. Note that in figure 8.1 the competitive number increases drastically near a bundle porosity of 65%, which is the result of the geometrical correction. Because at global porosity of 69% and a bundle porosity of about 65%, the inter-bundle length is almost zero, thus increasing the bundle porosity even further will result in the denominator of equation 4.21 approaching zero.

Note that in these simulations the capillary numbers were kept constant, as the global porosity (and therefore the macroscopic flow velocity) was kept constant. This indicates one of the limitations of the capillary number analysis, because a bundle porosity change quite logically influences the void formation behavior: decreased bundle porosity at a constant global porosity, leads to larger free flow domains and smaller, less permeable bundle domains, and thus the free flow will increasingly exceed the capillary flow as the bundle permeability decrease is dominant over the capillary pressure increase.

The difficulty in updating current global porosity - global permeability relationships is that they are based on global porosity changes, which are directly coupled to meso- and micro-structural changes which are hard to detach experimentally. Because once multiple layers are compressed it leads to bundle porosity changes and geometrical changes at the meso-scale.

In this analysis the macroscopic flow velocity was based on the global permeability - global porosity relationship as well. A couple of datafits were made as can be seen in figure 8.2. Two were based on the global permeability data from Çağlar et al. [11] to which a Kozeny-Carman relationship [F2] (equation 5.1) and an exponential function [F1] were fitted, and the last one was based on a Kozeny-Carman relationship [F3] between the measured global permeability (described in section 7.1) and an artificial data point with a 0% porosity and therefore a global

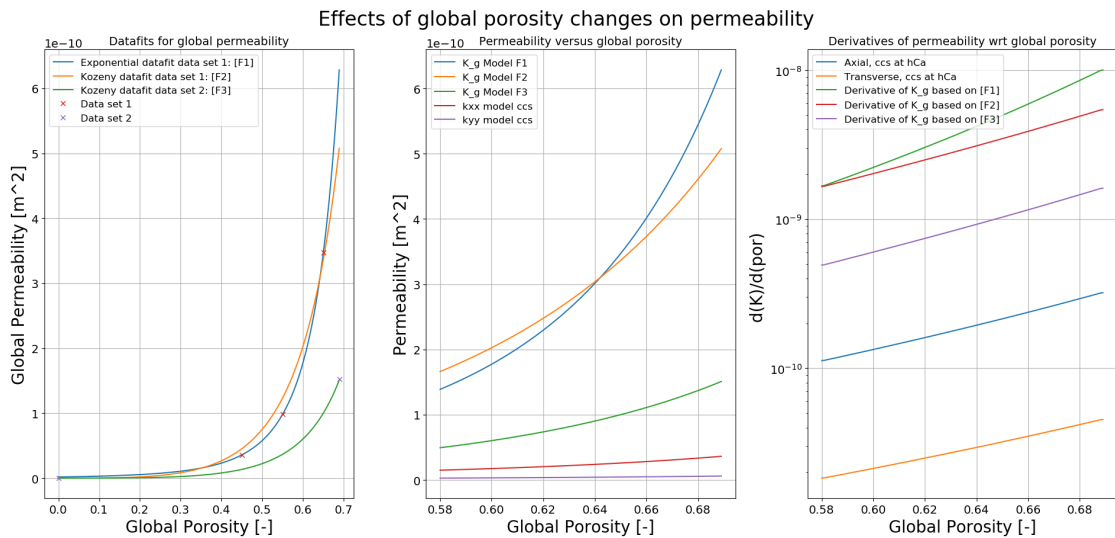


Figure 8.2: Global- and bundle Permeability relationships w.r.t porosity levels

permeability of 0 m^2 . Even though the Kozeny-Carman relationship isn't a perfect fit to the permeability data (as can be seen from 8.2), it is chosen over the exponential function due to the limited amount of data through which the function is fitted and the general academic acceptance of the Kozeny-Carman relationship. In addition to that the Kozeny-Carman fit to the experimental data was used in the modelling to better match the experiments. However, all functions show the same tendency, which is that the global permeabilities grow much faster than the bundle permeabilities with increased porosity, which can also be observed from the figure (note that in this figure the Constant-Cross-Section model was used and thus the global porosity is linearly related to the bundle porosity). This indicates once again the importance of the global permeability - bundle porosity relationship, because the global permeability is thus clearly dependent on more than just the bundle permeability.

Salvatori et al. [31] even describe that the macroscopic flow in the in-plane direction is predominantly related to the free flow through the inter-bundle domains. In this work they present two analytical methods for the determination of the global permeability based on the geometry on the mesoscale, which were in agreement with experimentally determined permeabilities. The first analytical method combines the Hagen-Poiseuille law for pressure driven, steady-state flow of incompressible fluids through straight channels (free flow) [33] with Darcy's law for fully saturated flow. The flow rate determined by the Hagen-Poiseuille law is fed into Darcy's law, and is then rewritten to determine the meso-geometry based global permeability [31]. Note that flow determined by the Hagen-Poiseuille law only describes the free flow through the inter-bundle domain, and therefore it can be argued that this is not representative for the global permeability. Therefore a second analytical method was proposed. In this method the permeabilities of the intra-bundle domains are based on the Gebart equations (equations 4.13 and 4.14) and the permeability of the inter-bundle domain is based on the first analytical (Hagen-Poiseuille law based) method. These different permeabilities are then area-averaged based on areas of the individual domains in the through thickness direction in an attempt to include the intra-bundle domain permeabilities. It turned out however, that the inter-bundle domain induced permeability was so dominant, that the effect of including the intra-bundle permeabilities was relatively small (only a maximum of 8% deviation between the two analytical methods). This indicates that the macroscopic flow indeed is predominantly related to the free flow through the inter-bundle domains, which is also supported by Syerko et al. [34], which state that the intra-bundle contribution to the macroscopic permeability is negligible. This therefore supports the assumption that the flow through the inter-bundle domains in the semi-analytical meso-flow model proposed in this thesis can be modelled by the macroscopic flow model which is fed with the experimentally determined global permeability.

Considering all the effects described above, a conclusion can be drawn on bundle porosity effects on void formation at a constant global preform porosity (or fiber volume fraction). If the bundle porosity is increased, intra-bundle flow is promoted. In addition to that increased bundle porosity at a constant global preform porosity results in smaller inter-bundle domains, and thus a reduction macroscopic (free) flow [31]. This can be advantageous for fast injection cycles, which are likely to result in intra-bundle voids. Increase bundle porosity in such a case could therefore lead to a reduction in the intra-bundle void size.

In slow injection situations on the other hand, from a void reduction point of view, it could be advantageous to do the opposite. Decreasing the bundle porosity, promotes the macroscopic flow (due to an increase in the inter-bundle domain) and decreases the intra-bundle flow as the permeability decrease is dominant over the capillary pressure increase. Therefore, inter-bundle void volumes obtained by slow injection velocities, can effectively be reduced by injecting a fabric with a lower bundle porosity at a constant global preform porosity under the same injection conditions.

To conclude this section the following final remark can be made, which is that depending on the intended injection strategy it can be either advantageous or disadvantageous to change the bundle porosity at a constant global porosity. The research presented in this report indicates that bundle porosity effects on void formation are considerable. Therefore, once designing an injection strategy, it can be advantageous to select a fabric with a specific meso-geometry corresponding to the intended injection cycle to reduce void sizes.

Chapter 9

Conclusion

The goal of this research was to investigate the relationship between mesoscale bundle porosity and void formation. A 2D semi-analytical model that was capable of quantifying the bundle-porosity effects on void formation, was created and validated experimentally. A single unit cell of a fabric consisting of bundles running in the direction parallel- and perpendicular to the macroscopic flow direction, with a meso-scale pore (the inter-bundle domain) in between them, was simplified by creating height-averaged rectangular domains. Flows based on Darcy's law were used to calculate the impregnation times for the individual domains. The impregnation time of the inter-bundle domain was determined by applying Darcy's law on the macroscopic scale and used the experimentally determined global permeability of the preform. To determine the intra-bundle impregnation times, Darcy's law was expanded with a capillary pressure term and the permeabilities of the bundles were determined based on Gebart's equations. Based on these impregnation times it could then be determined whether voids would form in the inter-bundle domain (combined impregnation time of the intra-bundle domains is lower than the impregnation time of the inter-bundle domain) or in the intra-bundle domain (impregnation time of the inter-bundle domain is lower than the combined impregnation times of the intra-bundle domains). This ratio of impregnation times was then quantified by the newly introduced competitive number C_o , for which the following conditions apply:

- $C_o < 1$: Intra-bundle void formation occurs.
- $C_o = 1$: No void formation occurs
- $C_o > 1$: Inter-bundle void formation occurs.

In the inter-bundle domain, spherical voids were expected and in the transverse intra-bundle domains elliptical voids were expected. As such void sizes were calculated based on the ratio of inter-bundle- and intra-bundle impregnation times and spherical- and ellipsoidal shape functions. Based on the injection parameters from the experiments, void sizes for high- and low capillary number situations were calculated and they matched well with the void shapes

and -sizes obtained from the experiments. As such it was concluded that the analytical model was suitable for the evaluation of bundle porosity - void formation effects.

By increasing the bundle porosity at constant global porosity, it was observed that the competitive number increased as well, which indicates that the bundle permeability increases faster than the capillary pressure in the bundles drops, implying therefore that the permeability change was dominant over the capillary pressure change. Increased bundle porosity therefore should promote intra-bundle flow. Note that the global permeability was not altered in this analysis as the global porosity was kept constant as the semi-analytical model corrected the meso-geometry to account for mesoscale bundle porosity changes at a constant fiber volume fraction.

In addition to that it was observed that at a constant cross-sectional geometry, and a varying global porosity, the global permeability changed faster than the bundle permeabilities. This indicates that the global permeability change is not solely dependent on the bundle permeabilities and therefore the fiber volume fraction, but much rather the combination of the bundle permeabilities and the meso-scale geometry. The influence of meso-structural changes on the global permeability has been described in literature before [31], and the general observation was that the global permeability was predominantly related to the shapes and sizes of the inter-bundle domains through which the flow can be described by the Hagen–Poiseuille law for pressure driven, steady-state flow of incompressible fluids through straight channels. The free flow obtained by this method was then fed into Darcy’s law for saturated flow, which then could be rewritten to determine the global permeability. The main observation was that increased inter-bundle (or free flow) domains lead to an increase in the global permeability and vice-versa.

Combining the relationship between bundle-porosity and intra-bundle flow, with the relationship between inter-bundle domain size and macroscopic flow, lead to the conclusion that varying the bundle porosity at a constant global preform porosity greatly influences the void formation process. Increased bundle porosity at a constant global preform porosity, increases intra-bundle flow and decreases inter-bundle flow, and naturally decreased bundle porosity at a constant global preform porosity then would lead to the opposite. As such it was concluded that choosing a fabric with a suitable mesoscale geometry once designing an injection strategy could be advantageous in terms of reducing the overall void content of the laminate.

Chapter 10

Recommendations

Based on this research a couple of recommendations are listed in this section for subsequent research. With respect to the mould, it was found that placing the preform over the pressure sensors results in distorted pressure measurements. Due to the compaction pressure of the fabrics, the pressure sensors will not measure the actual resin or air pressure, which is needed for the global permeability analysis. It was also observed that once the fabrics above the pressure sensors got impregnated, that the pressure did not increase as expected from the vacuum pressure to the resin pressure. This was contributed to the lubrication of the fabrics upon impregnation, which then alter the compaction pressure, leading once again to distorted pressure measurements. To obtain better measurements, it is recommended not to place the preform over the pressure sensors, or to place a cap with a tiny hole in the top over the pressure sensors, which separates fabric from the pressure sensors whilst allowing resin to hit the membrane of the sensor. A final recommendation on the mold design is that a different type of seal should be chosen, because the EPDM closed cell sponge -rubber seal was too thick (3mm) to be compressed to the desired 1mm thickness. It is therefore recommended to either use a thinner seal or to create a slot to place the seal in.

Another recommendation can be made based on the curing of the resin. Though the experimental results are in line with the model, it was assumed in the modelling that the wall effects introduced by the mold, were negligible in the middle layer, as these would predominantly effect the outer layers in the three layer- preform used in the experiments. From the global permeability measurement however, it was concluded that the wall effects contributed to the discrepancy between the measured global permeability and the global permeability described by Çağlar et al. [11]. To better detach these wall effects from the void formation mechanisms in a fabric, a larger amount of plies and thus a thicker preform should be used. To do so a couple of adjustments could be made. The mold could be adapted to allow for double sided fast radiation curing (e.g. make the lower mold transparent as well), another radiation curing resin system that has better absorption characteristics could be chosen or a resin system which requires a light pulse to initialize the curing reaction, but which continues to cure without additional radiation after initialisation, could be chosen. All these are supposed to contribute to achieving larger sample thicknesses.

Some final recommendations can be made based on the modelling of void formation on the mesoscale. Eventually it turned out that the Finite Element model based on the Brinkman equations combined with the continuity equation could not be adapted straight forwardly to account for a mesoscale constant capillary pressure as defined by Michaud [8], because in mesoscale analysis it would result in a very large pressure differential and thus flow velocity locally, which could not be fed by the surrounding FE-cells in a realistic manner. To account for this a model should be developed for which the capillary pressure differential can be taken properly with respect to both the saturation as the fingering distance. An initial attempt that could be investigated is to use the velocity correction proposed earlier (equation 4.10), experimentally determine the fingering length during a low capillary number infusion, and then take the derivative of the capillary pressure with respect to that length and compare the correlation between model and experiments. Note that that would mean that the velocity is corrected over the entire bundle-domain in order to satisfy the continuity equation. This however could result in an unrealistic flow behaviour at the edges of the intra-bundle domains (especially for discontinuous bundle sections). An alternative for this would be to modify surface tension models from soil sciences (such as the Van Genuchten relationship between saturation levels and capillary pressure) to account for highly directional materials instead of homogenized isotropic materials. With respect to the analytical model proposed in this research, it would be recommended to include a model that relates the inter-bundle geometry to the global permeability and use that model in this same analysis to check the effects. To create such a model it would be useful to measure the global permeability at different fiber volume fractions and relate the mesoscale geometry and the bundle porosities and relate those to the global permeability, rather than using the overall global porosity of the preform. In addition to that it would also be interesting to expand the analytical meso-flow model with an additional intra-bundle domain at the intersection of warp- and weft direction as the flow needs to turn around the corner there to entrap the air in the inter-bundle domain. Investigation these different recommendations, and especially those related to the modelling, should help to better understand void formation mechanics and thus result in lower void contents in liquid composite molded parts in the future.

References

- [1] C. H. Park and W. I. Lee. Modeling void formation and unsaturated flow in liquid composite molding processes: a survey and review. *Journal of Reinforced Plastics and Composites*, 30:957–977, 2011.
- [2] M. Mehdikhani, L. Gorbatikh, I. Verpoest, and S.V. Lomov. Voids in fiber-reinforced polymer composites: A review on their formation, characteristics, and effects on mechanical performance. *Journal of Composite Materials*, 53(12):1579–1669, 2019.
- [3] P. Bussetta and N. Correia. Numerical forming of continuous fibre reinforced composite material: A review. *Composites Part A: Applied Science and Manufacturing*, 113:12–31, 2018.
- [4] M. Labordus. Voids and bubbles during vacuum infusion. Technical report, Technische Universiteit Delft - Technisch Natuurwetenschappelijk Onderzoek, 2001.
- [5] M. Afendi, W. Banks, and D. Kirkwood. Bubble free resin for infusion process. *Composites Part A: Applied Science and Manufacturing*, 36:739–746, 2005.
- [6] S. G. Advani and E. M. Sozer. *Process Modeling in Composites Manufacturing*. Marcel Dekker, Inc, New York, 1 edition, 2003.
- [7] J. Teuwen. Continuous fibre-reinforced thermoset composites: Liquid composite moulding processes (i). <https://brightspace.tudelft.nl/d21/1e/content/192103/viewContent/1578551/View>, 2019. Accessed: 2021-08-11.
- [8] V. Michaud. A review of non-saturated resin flow in liquid composite moulding processes. *Transport in Porous Media*, 115:581–601, 2016.
- [9] R. Matsuzaki, D. Seto, M. Naito, et al. Analytical prediction of void formation in geometrically anisotropic woven fabrics during resin transfer molding. *Composites Science and Technology*, 107:154–161, 2015.

- [10] S. Comas, C. Binetruy, and P. Krawcza. Mechanical properties and permeability measurements of fibre reinforcements : a continuous method. In *The 8th International Conference on Flow Processes in Composite Materials (FPCM8) Douai, France*, July 2006.
- [11] B. Çağlar, C. Tekin, F. Karasu, and V Michaud. Assessment of capillary phenomena in liquid composite molding. *Composites Part A: Applied Science and Manufacturing*, 120:73–83, 2019.
- [12] P. Mallick. *Fiber-Reinforced Composites: Materials, Manufacturing, and Design*. CRC Press, Boca Raton, 3 edition, 2007.
- [13] Removing barriers to lightweighting ships with composites. <https://www.compositesworld.com/articles/removing-barriers-to-lightweighting-ships-with-composites>. Accessed: 2021-05-21.
- [14] R. Matsuzaki, D. Seto, A. Todoroki, and Y. Mizutani. In situ void content measurements during resin transfer molding. *Advanced Composite Materials*, 22(4):239–254, 2013.
- [15] J. Castro, L. Helfen, C. González, and F. Sket. An in situ investigation of void generation and transport during resin transfer moulding by means of synchrotron x-ray laminography. In *ECCM18 - 18th European Conference on Composite Materials Athens, Greece*, June 2018.
- [16] B.R. Gebart. Permeability of unidirectional reinforcements for rtm. *Journal of Composite Materials*, 113(8):1100–1133, 1992.
- [17] J. M. Lawrence, V. Neacsu, and S. G. Advani. Modeling the impact of capillary pressure and air entrapment on fiber tow saturation during resin infusion in lcm. *Composites Part A: Applied Science and Manufacturing*, 40(8):1053–1064, 2009.
- [18] N. Patel, V. Rohatgi, and L. James Lee. Micro scale flow behavior and void formation mechanism during impregnation through a unidirectional stitched fiberglass mat. *Polymer Engineering Science*, 35(10):837–851, 1995.
- [19] T.S. Lundström, B.R. Gebart, and C.Y. Lundemo. Void formation in rtm. *Journal of Reinforced Plastics and Composites*, 12:1339–1349, 1993.
- [20] C. Park, A. Lebel, A. Saouab, J. Bréard, and W. I. Lee. Modeling and simulation of voids and saturation in liquid composite molding processes. *Composites Part A: Applied Science and Manufacturing*, 42:658–668, 2011.
- [21] T.S. Lundström. Measurement of void collapse during resin transfer moulding. *Composites Part A: Applied Science and Manufacturing*, 28:201–214, 1997.
- [22] J. Wood and M. Bader. Void control for polymer-matrix composites (1): Theoretical and experimental methods for determining the growth and collapse of gas bubbles. *Composites Manufacturing*, 5:139–147, 1994.

-
- [23] S. van Oosterom, A. Schreier, M. Battley, et al. Influence of dissolved gasses in epoxy resin on resin infusion part quality. *Composites Part A: Applied Science and Manufacturing*, 132, 2020.
- [24] Z. Dimitrova and S. G. Advani. Analysis and characterization of relative permeability and capillary pressure for free surface flow of a viscous fluid across an array of aligned cylindrical fibers. *Journal of Colloid and Interface Science*, 245:325–337, 2002.
- [25] N. Vernet, E. Ruiz, S. Advani, et al. Experimental determination of the permeability of engineering textiles: Benchmark ii. *Composites Part A: Applied Science and Manufacturing*, 61:172–184, 2014.
- [26] R. Arbter, J. Beraud, C. Binetruy, et al. Experimental determination of the permeability of textiles: A benchmark exercise. *Composites Part A: Applied Science and Manufacturing*, 42:1157–1168, 2011.
- [27] C. H. Park and L. Woo. Modeling void formation and unsaturated flow in liquid composite molding processes: a survey and review. *Journal of Reinforced Plastics and Composites*, 30:957–977, 2011.
- [28] K. Yazdchi, S. Srivastava, and S. Luding. Microstructural effects on the permeability of periodic fibrous porous media. *International Journal of Multiphase Flow*, 37:956–966, 2011.
- [29] Refractive index database. <https://refractiveindex.info/?shelf=glass&book=soda-lime&page=Rubin-clear>. Accessed: 2021-04-21.
- [30] I. Duarte, A. Rotter, A. Malvestiti, and M. Silva. The role of glass as a barrier against the transmission of ultraviolet radiation: an experimental study. *Photodermatology, photoimmunology photomedicine*, 25:181–184, 2009.
- [31] D. Salvatori, B. Çağlar, H. Teixidó, and V. Michaud. Permeability and capillary effects in a channel-wise non-crimp fabric. *Composites Part A: Applied Science and Manufacturing*, 108:41–52, 2018.
- [32] F. Robitaille and R. Gauvin. Compaction of textile reinforcements for composites manufacturing. i: Review of experimental results. *Polymer Composites*, 19:198–216, 1998.
- [33] H. Bruus. *Theoretical microfluidics*. Oxford University Press, 2008.
- [34] E. Syerko, C. Binetruy, S. Comas-Cardona, and A. Leygue. A numerical approach to design dual-scale porosity composite reinforcements with enhanced permeability. *Materials Design*, 131:307–322, 2017.

Appendix A

Macro-flow model

The following 1D finite element model was used to describe the flow front propagation of the macroscale through a porous medium in a linear injection set-up. The model is based on Darcy's law which is combined with the continuity equation.

```
import numpy as np
from scipy import sparse
from scipy.sparse import coo_matrix
from numpy import linalg as lin
from matplotlib import pyplot as plt
from numpy import exp

import pandas as pd

def Connectivity_based_on_saturation(S_global):
    for i in range(len(S_global)):
        if S_global[i] == 0:
            break

    connectivity = np.arange(0,i+1,1)

    return connectivity

def Pressure_distribution_based_on_saturation(S_global):
    P_global_condition = ["Pk" for i in range(len(S_global))]
    P_global_numerical = [str(P_flowfront) for i in range(len(S_global))]
    P_global_numerical[0] = str(P_inlet)

    for i in range(len(S_global)):
        i +=1
```

```

    if S_global[i] == 0:
        break
    else:
        P_global_condition[i] = 'Pu'
        P_global_numerical[i] = ''

return P_global_condition, P_global_numerical

def K_global_generator(connect, A, mu, kxx, L_element, S_global):
    Kxx = -((kxx*A)/(L_element*mu))
    K_global_dense = np.zeros((len(S_global),len(S_global)))

    for i in range(connect[-1]):
        n1 = connect[i]
        n2 = connect[i+1]

        K_global_dense[n1,n1] += Kxx
        K_global_dense[n2,n2] += Kxx
        K_global_dense[n1,n2] += -Kxx
        K_global_dense[n2,n1] += -Kxx

    K_global_sparse = coo_matrix(K_global_dense)

    return K_global_dense, K_global_sparse

def Determine_unknown_pressures(P_numerical, K_global_sparse, S_global):
    K_global_rewritten = np.array([K_global_sparse.row,
                                   K_global_sparse.col,
                                   K_global_sparse.data])

    # Determine number of unknowns/knowns
    n_unknowns = 0
    n_knowns = 0
    for i in range(len(S_global)):
        if P_numerical[i] == '':
            n_unknowns +=1
        else:
            n_knowns += 1

    known_value_indexes = np.zeros((n_unknowns*2, n_knowns))
    start1 = 0

    # Determine indexes of known values in K-matrix
    for i in range(len(S_global)):
        if P_numerical[i] == '':
            start2 =0

```

```

    for j in range(len(S_global)):
        if P_numerical[j] != '':
            known_value_indexes[start1*2 , start2] = i
            known_value_indexes[start1*2+1 , start2] = j
            start2 += 1
        start1 +=1

# Determine which known combinations of pressure and permeability
# correspond to unknown pressures
known_values_vector = []

for i in range(n_unknowns):
    known_single_value = 0
    for j in range(n_knowns):
        for k in range(np.shape(K_global_rewritten)[1]):
            comparison = K_global_rewritten[:,k].astype(int) == \
                known_value_indexes[i*2:(i+1)*2,j]
            if comparison.all():
                column_index = int(known_value_indexes[i*2+1,j])
                known_single_value += -K_global_rewritten[2,k] * \
                    float(P_numerical[column_index])
                break
    known_values_vector.append(known_single_value)

# Determine the inverse of the stiffness matrix of the unknown pressures
Indexes_unknowns = []
for i in range(len(S_global)):
    if P_numerical[i] == '':
        Indexes_unknowns.append(i)

K_reduced = K_global_sparse.tocsr()[Indexes_unknowns,:]
K_reduced = K_reduced[:,Indexes_unknowns]

K_red_inv = lin.inv(K_reduced.toarray())

P_unknown = K_red_inv @ (known_values_vector)
P_total = P_numerical

for i in range(len(Indexes_unknowns)):
    P_total[Indexes_unknowns[i]] = P_unknown.astype(str)[i]
P_total = np.array(P_total).astype(float)

return P_total

def Calculate_flows(P_total, K_global_sparse,por):
    Q = (K_global_sparse @ P_total)/por
    return Q

```

```

def Update_saturation(S_global, Q_total, L_element, A):
    for i in range(len(S_global)):
        if S_global[i] == 0 and Q_total[i]>0:
            dt = (A*L_element)/(Q_total[i])
            break

    S_global[i] += (A*L_element)/(Q_total[i]*dt)

    return S_global, dt

def Flow_progression(S_global, A, L_element, mu, kxx, n_nodes, L, por):
    Loop = True
    t = 0
    t_list, s_list, impreg = [0], [0], [0]

    while Loop:
        Connectivity = \
        Connectivity_based_on_saturation(S_global)

        K_global = \
        K_global_generator(Connectivity, A, mu, kxx, L_element, S_global)[1]

        Pressure_distribution = \
        Pressure_distribution_based_on_saturation(S_global)

        Unknown_pressures = \
        Determine_unknown_pressures(Pressure_distribution[1],\
        K_global, S_global)

        Total_flow = \
        Calculate_flows(Unknown_pressures, K_global,por)

        Saturation_time = \
        Update_saturation(S_global, Total_flow, L_element, A)

        S_global = \
        Saturation_time[0]

        t += \
        Saturation_time[1]

        s_percentage = (len(S_global)/n_nodes)

        t_list.append(t)
        s_list.append(s_percentage)

```

```

    impreg.append(s_percentage*L)
    if len(S_global) == n_nodes:
        Loop = False
        break

    S_global = np.hstack((S_global,0.0))

    return t, t_list, s_list, impreg

#####
'''
Input data
'''
# Geometry
L = 0.165
A = 0.0001

# Darcy parameters
Ea = -63.87e3
A = 1.475e-12
R = 8.315
T1 = 19.67+ 273.15
T2 = 22.9 + 273.15
mu1 = A*exp(-Ea/(R*T1))
mu2 = A*exp(-Ea/(R*T2))
vf = 0.31
por = 1 - vf

P_inlet = 1.0133e5
P_flowfront = 50e3
kLSF = 1.484e-10
kSFF = 1.407e-10

# Mesh parameters
n_nodes = [50]

#####
# import experimental information

filename = "C:/Users/flori/Desktop/TU Delft/9. Thesis/Experimental results\
/Permeability/Permeability_determination_R4.xlsx"
Experimental_impregnation_times = pd.read_excel(filename,'Permeability')

FF5 = np.asarray(np.stack(Experimental_impregnation_times.values[1:12,1:3])\
                 .astype(None))

```

```

FF6 = np.asarray(np.stack(Experimental_impregnation_times.values[1:12,4:6])\
                 .astype(None))
VC2 = np.asarray(np.stack(Experimental_impregnation_times.values[1:12,7:9])\
                 .astype(None))
VC3 = np.asarray(np.stack(Experimental_impregnation_times.values[1:12,10:12])\
                 .astype(None))
VD1 = np.asarray(np.stack(Experimental_impregnation_times.values[1:12,13:15])\
                 .astype(None))
VD2 = np.asarray(np.stack(Experimental_impregnation_times.values[1:12,16:18])\
                 .astype(None))
MF_R10_20210807 = np.asarray(np.stack(Experimental_impregnation_times\
                                     .values[1:401,19:21]).astype(None))

#CA = np.asarray(np.stack(dataframe_20210713.values[0:12,0]).astype(None))
#####
# Output
SMALL_SIZE = 20
MEDIUM_SIZE = 28
BIGGER_SIZE = 32

plt.rc('font', size=SMALL_SIZE)           # controls default text sizes
plt.rc('axes', titlesize=MEDIUM_SIZE)    # fontsize of the axes title
plt.rc('axes', labelsiz=MEDIUM_SIZE)     # fontsize of the x and y labels
plt.rc('xtick', labelsiz=SMALL_SIZE)     # fontsize of the tick labels
plt.rc('ytick', labelsiz=SMALL_SIZE)     # fontsize of the tick labels
plt.rc('legend', fontsiz=SMALL_SIZE)     # legend fontsize
plt.rc('figure', titlesiz=BIGGER_SIZE)

for i in range(len(n_nodes)):
    # Starting conditions
    S_global = np.zeros(2)
    S_global[0] = 1
    L_element = L/(n_nodes[i]-1)

    # Data generation
    Time_saturation_SFF1 = Flow_progression(S_global, A, L_element, mu1, \
                                           kSFF, n_nodes[i], L, por)

    Time_SFF1 = Time_saturation_SFF1[1]
    Impregnation_length_SFF1 = Time_saturation_SFF1[3]

for i in range(len(n_nodes)):
    # Starting conditions
    S_global = np.zeros(2)
    S_global[0] = 1
    L_element = L/(n_nodes[i]-1)

    # Data generation

```

```
Time_saturation_SFF2 = Flow_progression(S_global, A, L_element, mu2, \
                                         kSFF,n_nodes[i],L,por)

Time_SFF2 = Time_saturation_SFF2[1]
Impregnation_length_SFF2 = Time_saturation_SFF2[3]

plt.plot(FF5[:,0], FF5[:,1], 'o', markersize = 10, label='FF5 at T = 21.56 degC')
plt.plot(FF6[:,0], FF6[:,1], 'o', markersize = 10, label='FF6 at T = 21.70 degC')
plt.plot(VC2[:,0], VC2[:,1], 'o', markersize = 10, label='VC2 at T = 19.67 degC')
plt.plot(VC3[:,0], VC3[:,1], 'o', markersize = 10, label='VC3 at T = 22.80 degC')
plt.plot(VD1[:,0], VD1[:,1], 'o', markersize = 10, label='VD1 at T = 20.75 degC')
plt.plot(VD2[:,0], VD2[:,1], 'o', markersize = 10, label='VD2 at T = 22.90 degC')
#plt.plot(MF_R10_20210807[:,0], MF_R10_20210807[:,1]/1000, \
# label='Macro flow model Brinkman equations at T = 21.56 degC')

#label_SFF = '1D FEM-model at T = 21.56 degC and K_SFF = ' \
# + str(np.round(kSFF,12)) + str(' m^2')
label_SFF1 = '1D FEM-model at T = 19.67 degC and K_SFF = ' \
+ str(np.round(kSFF,12)) + str(' m^2')
label_SFF2 = '1D FEM-model at T = 22.9 degC and K_SFF = ' \
+ str(np.round(kSFF,12)) + str(' m^2')

plt.plot(Time_SFF1, Impregnation_length_SFF1, label = label_SFF1)
plt.plot(Time_SFF2, Impregnation_length_SFF2, label = label_SFF2 )
plt.legend()
plt.xlabel('Time in seconds')
plt.ylabel('Impregnated length [m]')
plt.title('Time versus impregnated length preform')
#plt.hlines(0.165,0,800)
plt.grid()
plt.show()
```

Appendix B

Meso-Flow model

The following model is used to calculate void formation on the meso-scale based on the ratio of impregnation times of intra- and inter bundle domains. Flow through the inter-bundle domains is described by the macroscopic (Darcy's law) flow, a constant applied pressure differential and experimentally determined parameters. Flow through the intra-bundle domains is based on Darcy's law with a pressure differential which consists of the applied pressure differential and a capillary pressure term, Gebart bundle permeabilities and experimentally observed geometrical cross-sections which are simplified to rectangular, height-averaged sections.

```
import numpy as np
import pandas as pd
from numpy import pi, sin, cos, tan, sqrt, exp, log, diff, gradient
from scipy.optimize import curve_fit
from matplotlib import pyplot as plt

# Material properties
r1f = 4.5e-6      # Fiber radius [m]
gamma = 26.5e-3  # Surface tension [N/m]
theta = 30.9     # Contact angle [deg]
A = 1.475e-12
Ea = -63.87e3
R = 8.31446261815324
K_SFF = 1.407e-10

# Fabric Geometry
bundle_widths = [1.46, 1.68, 1.61, 1.61, 1.59, 1.55, 1.46, 1.49, 1.65, 1.48]
bundle_height = [0.27, 0.18, 0.19, 0.18, 0.16, 0.23, 0.20, 0.21, 0.24, 0.19]
Ply_thickness = np.array([1.50, 1.42, 1.44, 1.47, 1.41, 1.50, 1.44, 1.45])/3
Width_avg = (sum(bundle_widths)/len(bundle_widths))/1000
```

```

Height_avg = (sum(bundle_height)/len(bundle_height))/1000
Average_thickness = sum(Ply_thickness)/len(Ply_thickness)/1000
Bundle_spacing = 1.7e-3 #[m]

# Definitions
def Capillary(Porosity):
    c1f = 2*pi*r1f
    a1f = pi*(r1f**2)
    Sf = (1-Porosity)*(c1f/a1f)
    Pc = Sf*gamma*cos(np.deg2rad(theta))
    return Sf, Pc

def Permeability_gebart(Porosity):
    # Gebart constants
    C_axial = 53
    C_cross = 16/(9*pi*sqrt(6))
    Vfmax = pi/(2*sqrt(3))

    # Calculation
    K11 = (8*(r1f**2)/C_axial)*((Porosity**3)/((1-Porosity)**2))
    K22 = C_cross*(r1f**2)*(sqrt(Vfmax/(1-Porosity))-1)**2.5
    return K11, K22

def Viscosity(Temperature_degC):
    viscosity = A*exp(-Ea/(R*(Temperature_degC+273.15)))
    return viscosity

def Darcy_velocity(Permeability, Pressure_differential, viscosity, Porosity):
    Velocity = (Permeability * Pressure_differential) / (viscosity * Porosity)
    return Velocity

#####
#Permeability data fit from Capillary phenomena paper
#####
def Permeability_fit_Caglar_exponential(Fiber_volume_fraction, c1, c2):
    Global_permeability = c1*Fiber_volume_fraction**c2
    return Global_permeability

Caglar_permeabilities = np.array([[0.35, 3.47e-10],
                                  [0.45, 9.84e-11],
                                  [0.55, 3.54e-11]])

parameters_Caglar_expo, covariance_Caglar_expo = \
    curve_fit(Permeability_fit_Caglar_exponential,\
              Caglar_permeabilities[:,0], Caglar_permeabilities[:,1])

def Permeability_fit_Kozeny(Fiber_volume_fraction, k):

```

```

Global_permeability = ((4*(r1f**2))/k)*(((1-Fiber_volume_fraction)**3)\
    /(Fiber_volume_fraction**2))
return Global_permeability

Experimental_permeabilities= np.array([[1.0,0.0],
    [0.31, K_SFF]])

parameters_experiments_Kozeny, covariance_experiments_Kozeny = \
    curve_fit(Permeability_fit_Kozeny,Experimental_permeabilities[:,0], \
        Experimental_permeabilities[:,1])

parameters_Caglar_Kozeny, covariance_Caglar_Kozeny = \
    curve_fit(Permeability_fit_Kozeny,Caglar_permeabilities[:,0], \
        Caglar_permeabilities[:,1])

def Permeability_based_on_vf_corrected(Fiber_volume_fraction, Type_of_permeability):
    if Type_of_permeability == 'Exponential_Caglar':
        Global_permeability = \
            Permeability_fit_Caglar_exponential(Fiber_volume_fraction, \
                parameters_Caglar_expo[0], \
                parameters_Caglar_expo[1])

    elif Type_of_permeability == 'Kozeny_Caglar':
        Global_permeability = \
            Permeability_fit_Kozeny(Fiber_volume_fraction, \
                parameters_Caglar_Kozeny)

    elif Type_of_permeability == 'Kozeny_Experiments':
        Global_permeability = \
            Permeability_fit_Kozeny(Fiber_volume_fraction, \
                parameters_experiments_Kozeny)

    else:
        Global_permeability = K_SFF
    return Global_permeability

#####
# Geometry simplification
#####
def Scaled_geometry_model(Porosity, Fiber_volume_fraction):
    Volume_section = (Bundle_spacing**2)*Average_thickness
    Volume_fibers = Volume_section*Fiber_volume_fraction
    Length_diagonal = Height_avg / sin(np.deg2rad(45))
    Length_bundle = (Bundle_spacing - Height_avg / \
        tan(np.deg2rad(45))) + Length_diagonal

    Bundle_width_corrected = (Volume_fibers) / \

```

```

(2*(1-Porosity)*Length_bundle*Height_avg)

if Bundle_width_corrected>Bundle_spacing:
    Bundle_width_corrected = Width_avg
    L_L, L_T = Bundle_spacing - Width_avg, Bundle_spacing - Width_avg
    h_T, h_L = Height_avg, Height_avg
    Dimensions_check = 0

else:
    # Define parameters from matuzaki
    L_L = Bundle_spacing - Bundle_width_corrected
    L_T = L_L

    h_T, h_L = Height_avg, Height_avg
    Dimensions_check = 1

return L_L, L_T, h_T, h_L, Bundle_width_corrected, Dimensions_check

def Geometry_constant_cross_section(Fiber_volume_fraction):
    Volume_section = (Bundle_spacing**2)*Average_thickness
    Area_bundle = (0.5*Height_avg) * (0.5*Width_avg) * pi
    Bundle_width_corrected = Area_bundle/Height_avg
    Length_diagonal = Height_avg / sin(np.deg2rad(45))
    Length_bundle = (Bundle_spacing - Height_avg / tan(np.deg2rad(45))) \
        + Length_diagonal

    Porosity = 1-((Fiber_volume_fraction * Volume_section)/ \
        (2 * Length_bundle * Height_avg * Bundle_width_corrected ))

    L_L = Bundle_spacing-Bundle_width_corrected
    L_T = L_L

    h_T, h_L = Height_avg, Height_avg

    return L_L, L_T, h_T, h_L, Bundle_width_corrected, Porosity

#####

def Matuzaki_saturation_time(Porosity, Global_porosity, Pressure_inlet, \
    Pressure_outlet, Location, Temperature_degC, \
    Global_permeability_type, Optimize_geometry):
    Fiber_volume_fraction = 1-Global_porosity

    if Optimize_geometry == 'Fixed_bundle_porosity':
        Geometry = Scaled_geometry_model(Porosity, Fiber_volume_fraction)
        L_L, L_T, h_T, h_L, Bundle_width, Dimensions_check = \
            Geometry[0],Geometry[1],Geometry[2],Geometry[3], \

```

```

    Geometry[4], Geometry[5]

elif Optimize_geometry == 'Fixed_cross_section':
    Geometry = Geometry_constant_cross_section(Fiber_volume_fraction)
    L_L, L_T, h_T, h_L, Bundle_width, Porosity, Dimensions_check = \
    Geometry[0],Geometry[1],Geometry[2],Geometry[3], \
    Geometry[4], Geometry[5], 1

Apparent_porosity_L = 1-(h_L/Average_thickness)*(1-Porosity)
Apparent_porosity_T = 1-(h_T/Average_thickness)*(1-Porosity)

k_axial = Permeability_gebart(Apparent_porosity_L)[0]
k_cross = Permeability_gebart(Apparent_porosity_L)[1]

k_L = k_axial
k_T = k_cross

k_g = Permeability_based_on_vf_corrected(Fiber_volume_fraction, \
    Global_permeability_type)

mu = Viscosity(Temperature_degC)

Applied_pressure_differential = (Pressure_inlet-Pressure_outlet)/Location
Capillary_pressure_L = Capillary(Apparent_porosity_L)[1]
Capillary_pressure_T = Capillary(Apparent_porosity_T)[1]

P_c_L = Capillary_pressure_L/(L_L)
P_c_T = Capillary_pressure_T/(L_T)

v_L = Darcy_velocity(k_L, Applied_pressure_differential+P_c_L,\
    mu, Apparent_porosity_L)
v_T = Darcy_velocity(k_T, Applied_pressure_differential+P_c_T,\
    mu, Apparent_porosity_T)
v_g = Darcy_velocity(k_g, Applied_pressure_differential, \
    mu, (1-Fiber_volume_fraction))

t_L = L_L/v_L
t_T = (L_T/2)/v_L
t_g = L_L/v_g
t_bb = Bundle_width / v_T
t_bg = Bundle_width / v_g

Competition = t_g/(t_L+t_T)

if Competition > 1:
    Void_radius = ((1-((t_L+t_T)/t_g))*L_L)/2

```

```

Void_volume_uncompressed = (4/3)*pi*(Void_radius**3)

else:
    a = 0.5*    L_T * (1-(t_g/(t_L+t_T)))
    c = 0.5*    Bundle_width * (1-(t_bg/t_bb))
    b = 0.5*    Height_avg * (1-(t_bg/t_bb))
    Void_volume_uncompressed = ((4/3)*pi*a*b*c)*Porosity

Ca = (v_g*mu)/(gamma * cos(np.deg2rad(theta)))

return Competition, k_axial, k_cross, Void_volume_uncompressed, \
        Bundle_width, k_g, Ca, Dimensions_check

#####
# Input
P_in = 101325
P_out = 50e3
vf = 0.31
Global_porosity_experiments = 1-vf
porosity_exp = 0.5151922254752931
T = 20
stepsize = 0.001

lCa_loc = 0.2
hCa_loc = 0.067

#####
# Calculate effects of varying location (Figure 1 & 2)
#####
location = np.arange(0.01, 0.4, stepsize)
location_dependency = []

for i in range(len(location)):
    # Figure 2: Influence of impregnation length at
    # fixed bundle porosity and fiber volume fraction
    location_dependency.append(Matuzaki_saturation_time(porosity_exp, \
                                                        Global_porosity_experiments, \
                                                        P_in, P_out, location[i], T, \
                                                        'Kozeny_Experiments', \
                                                        'Fixed_bundle_porosity'))

location_dependency = np.array(location_dependency)

#####
# Calculate effects of varying global porosity (figure 3)
#####
# Create datafits

```

```

Global_porosity_datafit = np.arange(0.0, 0.69, stepsize)
Global_permeability_expo_caglar, Global_permeability_Kozeny_caglar, \
Global_permeability_Kozeny_experiments = [], [], []

for i in range(len(Global_porosity_datafit)):
    Global_permeability_expo_caglar.append(\
        Permeability_based_on_vf_corrected(1-Global_porosity_datafit[i], \
            'Exponential_Caglar'))
    Global_permeability_Kozeny_caglar.append(\
        Permeability_based_on_vf_corrected(1-Global_porosity_datafit[i], \
            'Kozeny_Caglar')[0])
    Global_permeability_Kozeny_experiments.append(\
        Permeability_based_on_vf_corrected(1-Global_porosity_datafit[i], \
            'Kozeny_Experiments')[0])

# Create data based on models
Global_porosity = np.arange(0.58, 0.69, stepsize)
hCa_cbp, hCa_ccs, lCa_cbp, lCa_ccs = [], [], [], []
F1, F2 = [], []

for i in range(len(Global_porosity)):
    hCa_cbp.append(Matuzaki_saturation_time(porosity_exp, Global_porosity[i], \
        P_in, P_out, hCa_loc, T, 'Kozeny_Experiments', 'Fixed_bundle_porosity'))
    hCa_ccs.append(Matuzaki_saturation_time(porosity_exp, Global_porosity[i], \
        P_in, P_out, hCa_loc, T, 'Kozeny_Experiments', 'Fixed_cross_section'))
    lCa_cbp.append(Matuzaki_saturation_time(porosity_exp, Global_porosity[i], \
        P_in, P_out, lCa_loc, T, 'Kozeny_Experiments', 'Fixed_bundle_porosity'))
    lCa_ccs.append(Matuzaki_saturation_time(porosity_exp, Global_porosity[i], \
        P_in, P_out, lCa_loc, T, 'Kozeny_Experiments', 'Fixed_cross_section'))
    F1.append(Permeability_based_on_vf_corrected(1-Global_porosity[i], \
        'Exponential_Caglar'))
    F2.append(Permeability_based_on_vf_corrected(1-Global_porosity[i], \
        'Kozeny_Caglar')[0])

hCa_cbp, hCa_ccs, lCa_cbp, lCa_ccs = np.array(hCa_cbp), \
np.array(hCa_ccs), np.array(lCa_cbp), np.array(lCa_ccs)

# Take derivatives
der_Axial_K_hCa_ccs, der_Transverse_K_hCa_ccs = \
    gradient(hCa_ccs[:,1], stepsize), gradient(hCa_ccs[:,2], stepsize)
der_Axial_K_hCa_cbp, der_Transverse_K_hCa_cbp = \
    gradient(hCa_cbp[:,1], stepsize), gradient(hCa_cbp[:,2], stepsize)
der_Axial_K_lCa_ccs, der_Transverse_K_lCa_ccs = \
    gradient(lCa_ccs[:,1], stepsize), gradient(lCa_ccs[:,2], stepsize)
der_Axial_K_lCa_cbp, der_Transverse_K_lCa_cbp = \
    gradient(lCa_cbp[:,1], stepsize), gradient(lCa_cbp[:,2], stepsize)

```

```

der_F1 = gradient(F1, stepsize)
der_F2 = gradient(F2, stepsize)
der_F3 = gradient(hCa_ccs[:,5], stepsize)

#####
# Calculate effects of varying bundle porosity (figure 4) at constant vf
#####
Bundle_porosity = np.arange(0.01, 0.65, stepsize)

hCa_ccs_vbp, hCa_cbp_vbp, lCa_ccs_vbp, lCa_cbp_vbp = [], [], [], []

for i in range(len(Bundle_porosity)):
    hCa_ccs_vbp.append(Matuzaki_saturation_time(Bundle_porosity[i], \
        Global_porosity_experiments, P_in, P_out, hCa_loc, T, \
        'Kozeny_Experiments', 'Fixed_cross_section'))
    hCa_cbp_vbp.append(Matuzaki_saturation_time(Bundle_porosity[i], \
        Global_porosity_experiments, P_in, P_out, hCa_loc, T, \
        'Kozeny_Experiments', 'Fixed_bundle_porosity'))
    lCa_ccs_vbp.append(Matuzaki_saturation_time(Bundle_porosity[i], \
        Global_porosity_experiments, P_in, P_out, lCa_loc, T, \
        'Kozeny_Experiments', 'Fixed_cross_section'))
    lCa_cbp_vbp.append(Matuzaki_saturation_time(Bundle_porosity[i], \
        Global_porosity_experiments, P_in, P_out, lCa_loc, T, \
        'Kozeny_Experiments', 'Fixed_bundle_porosity'))

hCa_ccs_vbp, hCa_cbp_vbp, lCa_ccs_vbp, lCa_cbp_vbp = np.array(hCa_ccs_vbp), \
np.array(hCa_cbp_vbp), np.array(lCa_ccs_vbp), np.array(lCa_cbp_vbp)

# Crop arrays based on the geometry check for the fixed bundle porosity models
Checker = hCa_cbp_vbp[:,7]==1
hCa_ccs_vbp = hCa_ccs_vbp[Checker]
hCa_cbp_vbp = hCa_cbp_vbp[Checker]
lCa_ccs_vbp = lCa_ccs_vbp[Checker]
lCa_cbp_vbp = lCa_cbp_vbp[Checker]
Bundle_porosity = Bundle_porosity[Checker]

#####
# Import experimental data on void sizes

# High capillary number data
filename_hCa = \
"C:/Users/flori/Desktop/TU Delft/9. Thesis/Modeling/Meso_flow/\
VC4_Void_content_5mu_hCa_R1.xlsx"
Void_sizes_hCa_raw = pd.read_excel(filename_hCa, 'Sheet')
Void_sizes_hCa_raw = np.asarray(np.stack(Void_sizes_hCa_raw.values[0:,:0])\
.astype(None))

```

```
# Threshold size for void below a size of a sphere with 100 x r1f (fiberradius)
Void_threshold_size_hCa = 0.001
Void_sizes_above_threshold_hCa = []

for i in range(len(Void_sizes_hCa_raw)):
    if Void_sizes_hCa_raw[i] > Void_threshold_size_hCa:
        Void_sizes_above_threshold_hCa.append(Void_sizes_hCa_raw[i])

Average_void_size_hCa = np.mean(Void_sizes_above_threshold_hCa)

# Low capillary number data
filename_lCa = \
"C:/Users/flori/Desktop/TU Delft/9. Thesis/Modeling/Meso_flow/\
VC2_Void_content_5mu_lCa_R1.xlsx"
Void_sizes_lCa_raw = pd.read_excel(filename_lCa, 'Sheet')
Void_sizes_lCa_raw = np.asarray(np.stack(Void_sizes_lCa_raw.values[0:,0])\
.astype(None))

# Threshold size for void below a size of a sphere with 10 x r1f (fiberradius)
Void_threshold_size_lCa = 0.001
Void_sizes_above_threshold_lCa = []

for i in range(len(Void_sizes_lCa_raw)):
    if Void_sizes_lCa_raw[i] > Void_threshold_size_lCa:
        Void_sizes_above_threshold_lCa.append(Void_sizes_lCa_raw[i])

Average_void_size_lCa = np.mean(Void_sizes_above_threshold_lCa)

#####
# Plot lay out
#####

SMALL_SIZE = 14
MEDIUM_SIZE = 20
BIGGER_SIZE = 24

plt.rc('font', size=SMALL_SIZE)          # controls default text sizes
plt.rc('axes', titlesize=SMALL_SIZE)     # fontsize of the axes title
plt.rc('axes', labelsiz=MEDIUM_SIZE)     # fontsize of the x and y labels
plt.rc('xtick', labelsiz=SMALL_SIZE)     # fontsize of the tick labels
plt.rc('ytick', labelsiz=SMALL_SIZE)     # fontsize of the tick labels
plt.rc('legend', fontsize=12)            # legend fontsize
plt.rc('figure', titlesize=BIGGER_SIZE)
```

```
#####
# FIGURE 1: Capillary number, void size and competitive number versus location
# along impregnation length
#####

plt.figure(1)
figure_1_title = 'Plots for a a constant bundle porosity of ' + \
str(np.round(porosity_exp*100,1)) +'% and global porosity of '\
+str(np.round(100-vf*100,1)) + ' %'
plt.suptitle(figure_1_title)

# Create nodes set for datapoints
stp_n = int(len(location)/10)
n0, n1, n2, n3, n4, n5 = 0*stp_n, 1*stp_n, 2*stp_n, 3*stp_n, 4*stp_n, 5*stp_n
n6, n7, n8, n9, n10 = 6*stp_n, 7*stp_n, 8*stp_n, 9*stp_n, 10*stp_n-1

plt.subplot(131)
plt.plot(location*1e3,location_dependency[:,0])
plt.xlabel('Location along preform [mm]')
plt.ylabel('Competitive number <C> [-]')
plt.axhline(y=1, color = 'black')
plt.grid()

plt.subplot(132)
plt.plot(location*1e3,location_dependency[:,6])
plt.xlabel('Location along preform [mm]')
plt.ylabel('Capillary number [-]')
plt.axhline(color = 'black')
plt.grid()

plt.subplot(133)
plt.plot(location*1e3,location_dependency[:,3]*1e9)
plt.plot(lCa_loc*1e3, Average_void_size_lCa, 'o', markersize = 15, \
label = 'Average void size from experiments at lCa-location')
plt.plot(hCa_loc*1e3, Average_void_size_hCa, 'o', markersize = 15, \
label = 'Average void size from experiments at hCa-location')
plt.xlabel('Location along preform [mm]')
plt.ylabel('Void volume [mm^3]')
plt.axhline(color = 'black')
plt.legend()
plt.grid()

#####
# FIGURE 2: Void size versus capillary number, inverse of competitive number
# and location
#####
plt.figure(2)
```

```

figure_2_title = 'Plots for a a constant bundle porosity of ' \
+ str(np.round(porosity_exp*100,1)) +'%' and global porosity of '\
+str(np.round(100-vf*100,1)) + ' %'
plt.suptitle(figure_2_title)

plt.subplot(131)
plt.plot(location*1e3,location_dependency[:,3]*1e9)
plt.plot(lCa_loc*1e3, Average_void_size_lCa, 'o', markersize = 15, \
label = 'Average void size from experiments at lCa-location')
plt.plot(hCa_loc*1e3, Average_void_size_hCa, 'o', markersize = 15, \
label = 'Average void size from experiments at hCa-location')
plt.xlabel('Location along preform [mm]')
plt.ylabel('Void volume [mm3]')
plt.axhline(color = 'black')
plt.legend()
plt.grid()

plt.subplot(132)
plt.plot(location_dependency[:,6],location_dependency[:,3]*1e9)
plt.xlabel('Capillary number')
plt.ylabel('Void volume [mm3]')
plt.axhline(color = 'black')
plt.grid()

plt.subplot(133)
plt.plot(np.reciprocal(location_dependency[:,0]),location_dependency[:,3]*1e9)
plt.xlabel('Inverse of competitive number')
plt.ylabel('Void volume [mm3]')
plt.axhline(color = 'black')
plt.grid()

#####
# FIGURE 3:Permeability changes versus global porosity
#####
plt.figure(3)
figure_3_title = 'Effects of global porosity changes on permeability'
plt.suptitle(figure_3_title)

plt.subplot(131)
plt.title('Datafits for global permeability')
plt.plot(Global_porosity_datafit,Global_permeability_expo_caglar, \
label = 'Exponential datafit data set 1: [F1]')
plt.plot(Global_porosity_datafit,Global_permeability_Kozeny_caglar, \
label = 'Kozeny datafit data set 1: [F2]')
plt.plot(Global_porosity_datafit,Global_permeability_Kozeny_experiments, \
label = 'Kozeny datafit data set 2: [F3]')
plt.plot(1-Caglar_permeabilities[:,0],Caglar_permeabilities[:,1], 'x', \

```

```

        label = 'Data set 1')
plt.plot(1-Experimental_permeabilities[:,0],Experimental_permeabilities[:,1], \
        'x', label = 'Data set 2')
plt.xlabel('Global Porosity [-]')
plt.ylabel('Global Permeability [m^2]')
plt.legend()
plt.grid()

plt.subplot(132)
plt.title('Permeability versus global porosity')
plt.plot(Global_porosity,F1, label = 'K_g Model F1')
plt.plot(Global_porosity,F2, label = 'K_g Model F2')
plt.plot(Global_porosity,hCa_cbp[:,5], label = 'K_g Model F3')
plt.plot(Global_porosity,hCa_ccs[:,1], label = 'kxx model ccs')
plt.plot(Global_porosity,hCa_ccs[:,2], label = 'kyy model ccs')
plt.xlabel('Global Porosity [-]')
plt.ylabel('Permeability [m^2]')
plt.legend()
plt.grid()

plt.subplot(133)
plt.yscale('log')
plt.title('Derivatives of permeability wrt global porosity')
plt.plot(Global_porosity,der_Axial_K_hCa_ccs, label = 'Axial, ccs at hCa')
plt.plot(Global_porosity,der_Transverse_K_hCa_ccs, \
        label = 'Transverse, ccs at hCa')
plt.plot(Global_porosity,der_F1, label = 'Derivative of K_g based on [F1]')
plt.plot(Global_porosity,der_F2, label = 'Derivative of K_g based on [F2]')
plt.plot(Global_porosity,der_F3, label = 'Derivative of K_g based on [F3]')
plt.xlabel('Global Porosity [-]')
plt.ylabel('d(K)/d(por) ')
plt.legend()
plt.grid()

#####
# FIGURE 4: Bundle porosity effects on competitive number and capillary number
#####
plt.figure(4)
figure_4_title='Effects of bundle porosity for a constant global porosity of '\
+ str(1-vf) + ' %'
plt.suptitle(figure_4_title)

plt.subplot(131)
plt.yscale('log')
plt.plot(Bundle_porosity, hCa_cbp_vbp[:,0], label = 'sgm model at hCa location')
plt.plot(Bundle_porosity, lCa_cbp_vbp[:,0], label = 'sgm model at lCa location')
plt.xlabel('Bundle Porosity')

```

```
plt.ylabel('Competitive number')
plt.legend()
plt.grid()

plt.subplot(132)
plt.plot(Bundle_porosity, hCa_cbp_vbp[:,6], label = 'sgm model at hCa location')
plt.plot(Bundle_porosity, lCa_cbp_vbp[:,6], label = 'sgm model at lCa location')
plt.xlabel('Bundle Porosity')
plt.ylabel('Capillary number')
plt.legend()
plt.grid()

plt.subplot(133)
plt.yscale('log')
plt.plot(Bundle_porosity, hCa_cbp_vbp[:,3]*1e9, \
         label = 'sgm model at hCa location')
plt.plot(Bundle_porosity, lCa_cbp_vbp[:,3]*1e9, \
         label = 'sgm model at lCa location')
plt.xlabel('Bundle Porosity')
plt.ylabel('Void volume [mm3]')
plt.legend()
plt.grid()

plt.show()
```

Appendix C

Viscosity Measurements

Table C.1 presents the data to which the Arrhenius function is fitted and from which the constants have been used in other models as well. The following script has been used to process the data presented in the table, as well as data from literature and an failed experiment which is not included in this report:

```
import numpy as np
import matplotlib.pyplot as plt
import pandas as pd
from matplotlib import pyplot as plt
from scipy.optimize import curve_fit
from numpy import exp

# Import data
filename = "C:/Users/flori/Desktop/TU Delft/9. Thesis\
/Experimental results/Viscosity/Viscosity_20210713.xlsx"
dataframe_20210713 = pd.read_excel(filename, 'Viscosity_20210713')
Temp_20210713 = np.asarray(np.stack(dataframe_20210713.values[:,3]).astype(None))
Visc_20210713 = np.asarray(np.stack(dataframe_20210713.values[:,2]).astype(None))

dataframe_20210707 = pd.read_excel(filename, 'Viscosity_20210707')
Temp_20210707 = np.asarray(np.stack(dataframe_20210707.values[:,3]).astype(None))
Visc_20210707 = np.asarray(np.stack(dataframe_20210707.values[:,2]).astype(None))

Temp = np.concatenate((Temp_20210713, Temp_20210707))
Visc = np.concatenate((Visc_20210713, Visc_20210707))

# Create arrhenius function
def Arrhenius(T_c, A, Ea):
    R = 8.31446261815324
```

```

T = T_c + 273.15
eta = A*exp(-Ea/(R*T))
return eta

# Find paramters and coveriance
parameters_tot, covariance_tot = curve_fit(Arrhenius, Temp, Visc)
parameters_20210713, covariance_20210713 = \
curve_fit(Arrhenius, Temp_20210713, Visc_20210713)
parameters_20210707, covariance_20210707 = \
curve_fit(Arrhenius, Temp_20210707, Visc_20210707)

# Create datafit total
T_fit = np.linspace(15,30,31)
eta_fit_tot = Arrhenius(T_fit,parameters_tot[0],parameters_tot[1])
eta_fit_20210713 = Arrhenius(T_fit,parameters_20210713[0],parameters_20210713[1])
eta_fit_20210707 = Arrhenius(T_fit,parameters_20210707[0],parameters_20210707[1])

Fit_tot = np.array([T_fit, eta_fit_tot])
Fit_20210713 = np.array([T_fit, eta_fit_20210713])
Fit_20210707 = np.array([T_fit, eta_fit_20210707])

# Create plot based on literature
A_lit = 2.2384e-10
Ea_lit = -51930
eta_lit = Arrhenius(T_fit,A_lit,Ea_lit)
Literature = np.array([T_fit, eta_lit])

# plot data along fit
SMALL_SIZE = 18
MEDIUM_SIZE = 20
BIGGER_SIZE = 24

plt.rc('font', size=SMALL_SIZE)          # controls default text sizes
plt.rc('axes', titlesize=SMALL_SIZE)     # fontsize of the axes title
plt.rc('axes', labelsiz=SMALL_SIZE)      # fontsize of the x and y labels
plt.rc('xtick', labelsiz=SMALL_SIZE)     # fontsize of the tick labels
plt.rc('ytick', labelsiz=SMALL_SIZE)     # fontsize of the tick labels
plt.rc('legend', fontsize=SMALL_SIZE)    # legend fontsize
plt.rc('figure', titlesize=BIGGER_SIZE)

plt.plot(Temp_20210713,Visc_20210713, 'x', label='Data from experiments 2021-07-13')
#plt.plot(Temp_20210707,Visc_20210707, 'x', label='Data from experiments 2021-07-07')
label_tot = str('Fitted Arrhenius curve to all data; A = ')+\
str(np.round(parameters_tot[0],15))+str(' [Pa*s] and Ea = ')+\
str( np.round((parameters_tot[1]/1000),2))+str(' [kJ/mol]')

label_20210713 = str('Fitted Arrhenius curve to data 20210713; A = ')+\

```

```

str(np.round(parameters_20210713[0],15))+str(' [Pa*s] and Ea = ')+\
str( np.round((parameters_20210713[1]/1000),2))+str( ' [kJ/mol]')

label_20210707 = str('Fitted Arrhenius curve to data 20210707; A = ')\
+ str(np.round(parameters_20210707[0],15))+str(' [Pa*s] and Ea = ')+\
str( np.round((parameters_20210707[1]/1000),2))+str( ' [kJ/mol]')

label_literature = str('Literature datafit; A = ') +\
str(np.round(A_lit,12)) + str(' [Pa*s] and Ea = ') +\
str(np.round(Ea_lit/1000,2))+str( ' [kJ/mol]')

#plt.plot(T_fit,eta_fit_tot, label=label_tot)
plt.plot(T_fit,eta_fit_20210713, label=label_20210713)
#plt.plot(T_fit,eta_fit_20210707, label=label_20210707)
plt.plot(T_fit,eta_lit, label=label_literature)
plt.xlabel('Temperature [degC]')
plt.ylabel('Viscosity [Pa*s]')
plt.title('Arrhenius temperature-viscosity relationship')
plt.legend()
plt.grid()
plt.show()

```

Table C.1: Viscosity measurements

Shear rate in 1/s	Surface tension in Pas	T in C	t in min
10,02	0,51	14,90	0,50
10,02	0,54	14,90	1,00
10,02	0,54	15,10	1,50
10,02	0,55	15,10	2,00
10,02	0,56	15,20	2,50
10,02	0,56	15,20	3,00
10,03	0,56	15,30	3,50
10,03	0,56	15,30	4,00
10,03	0,55	15,30	4,50
10,03	0,55	15,40	5,00
10,03	0,55	15,50	5,50
10,03	0,55	15,50	6,00
10,03	0,54	15,60	6,50
10,03	0,54	15,60	7,00
10,03	0,54	15,70	7,50
10,03	0,54	15,70	8,00
10,04	0,53	15,80	8,50
10,04	0,53	15,80	9,00
10,04	0,53	15,90	9,50
10,04	0,53	15,80	10,00

10,04	0,52	16,00	10,50
10,04	0,52	16,00	11,00
10,04	0,52	16,10	11,50
10,04	0,51	16,00	12,00
10,04	0,51	16,20	12,50
10,04	0,51	16,20	13,00
10,05	0,50	16,40	13,50
10,05	0,50	16,30	14,00
10,05	0,50	16,40	14,50
10,05	0,50	16,40	15,00
10,05	0,49	16,50	15,50
10,05	0,49	16,50	16,00
10,05	0,49	16,60	16,50
10,05	0,49	16,60	17,00
10,06	0,48	16,70	17,50
10,06	0,48	16,70	18,00
10,06	0,48	16,80	18,50
10,06	0,48	16,80	19,00
10,06	0,47	16,90	19,50
10,06	0,47	16,90	20,00
10,06	0,47	17,00	20,50
10,06	0,47	17,00	21,00
10,06	0,46	17,10	21,50
10,06	0,46	17,10	22,00
10,07	0,46	17,20	22,50
10,07	0,46	17,20	23,00
10,07	0,45	17,30	23,50
10,07	0,45	17,20	24,00
10,07	0,45	17,40	24,50
10,07	0,45	17,40	25,00
10,07	0,44	17,60	25,50
10,07	0,44	17,60	26,00
10,07	0,44	17,60	26,50
10,07	0,44	17,60	27,00
10,08	0,44	17,80	27,50
10,08	0,43	17,70	28,00
10,08	0,43	17,90	28,50
10,08	0,43	17,70	29,00
10,08	0,43	17,80	29,50
10,08	0,43	17,90	30,00
10,09	0,42	18,10	30,50
10,08	0,42	18,00	31,00
10,08	0,42	18,00	31,50
10,09	0,42	18,10	32,00

10,09	0,41	18,10	32,50
10,09	0,41	18,30	33,00
10,09	0,41	18,20	33,50
10,09	0,41	18,30	34,00
10,09	0,41	18,30	34,50
10,09	0,40	18,40	35,00
10,09	0,40	18,40	35,50
10,09	0,40	18,40	36,00
10,10	0,40	18,60	36,50
10,10	0,40	18,60	37,00
10,10	0,39	18,80	37,50
10,10	0,39	18,70	38,00
10,10	0,39	18,80	38,50
10,10	0,39	18,70	39,00
10,10	0,39	18,90	39,50
10,10	0,38	18,90	40,00
10,10	0,38	19,00	40,50
10,11	0,38	19,00	41,00
10,11	0,38	19,10	41,50
10,11	0,38	19,10	42,00
10,11	0,38	19,20	42,50
10,11	0,37	19,20	43,00
10,11	0,37	19,30	43,50
10,11	0,37	19,30	44,00
10,11	0,37	19,40	44,50
10,11	0,37	19,40	45,00
10,12	0,37	19,50	45,50
10,12	0,36	19,50	46,00
10,12	0,36	19,50	46,50
10,12	0,36	19,60	47,00
10,12	0,36	19,70	47,50
10,12	0,36	19,80	48,00
10,12	0,35	19,80	48,50
10,12	0,35	19,80	49,00
10,12	0,35	19,90	49,50
10,13	0,35	19,90	50,00
10,13	0,35	20,00	50,50
10,13	0,35	20,00	51,00
10,13	0,35	20,10	51,50
10,13	0,34	20,10	52,00
10,13	0,34	20,20	52,50
10,13	0,34	20,20	53,00
10,14	0,34	20,40	53,50
10,14	0,34	20,40	54,00

10,14	0,34	20,40	54,50
10,14	0,34	20,40	55,00
10,14	0,33	20,60	55,50
10,14	0,33	20,50	56,00
10,14	0,33	20,50	56,50
10,14	0,33	20,60	57,00
10,14	0,33	20,80	57,50
10,14	0,33	20,70	58,00
10,15	0,32	20,90	58,50
10,14	0,32	20,80	59,00
10,15	0,32	21,00	59,50
10,15	0,32	20,90	60,00
10,15	0,32	21,00	60,50
10,15	0,32	21,00	61,00
10,15	0,31	21,20	61,50
10,15	0,32	21,10	62,00
10,15	0,31	21,20	62,50
10,15	0,31	21,30	63,00
10,16	0,31	21,40	63,50
10,16	0,31	21,30	64,00
10,16	0,31	21,40	64,50
10,16	0,31	21,40	65,00
10,16	0,31	21,50	65,50
10,16	0,30	21,40	66,00
10,16	0,30	21,70	66,50
10,16	0,30	21,60	67,00
10,16	0,30	21,70	67,50
10,16	0,30	21,70	68,00
10,17	0,30	21,80	68,50
10,17	0,30	21,80	69,00
10,17	0,30	22,00	69,50
10,17	0,29	21,90	70,00
10,17	0,29	22,10	70,50
10,17	0,29	22,00	71,00
10,17	0,29	22,00	71,50
10,17	0,29	22,10	72,00
10,17	0,29	22,10	72,50
10,17	0,29	22,20	73,00
10,17	0,29	22,20	73,50
10,18	0,29	22,30	74,00
10,18	0,28	22,30	74,50
10,18	0,28	22,30	75,00
10,18	0,28	22,40	75,50
10,18	0,28	22,40	76,00

10,18	0,28	22,60	76,50
10,19	0,28	22,70	77,00
10,18	0,28	22,60	77,50
10,18	0,28	22,60	78,00
10,19	0,27	22,70	78,50
10,19	0,27	22,80	79,00
10,19	0,27	22,90	79,50
10,19	0,27	22,90	80,00
10,19	0,27	23,00	80,50
10,20	0,27	23,10	81,00
10,19	0,27	23,10	81,50
10,19	0,27	23,10	82,00
10,20	0,26	23,20	82,50
10,20	0,26	23,30	83,00
10,20	0,26	23,40	83,50
10,20	0,26	23,30	84,00
10,20	0,26	23,40	84,50
10,20	0,26	23,40	85,00
10,21	0,26	23,60	85,50
10,20	0,26	23,50	86,00
10,21	0,26	23,70	86,50
10,21	0,25	23,70	87,00
10,21	0,25	23,80	87,50
10,21	0,26	23,70	88,00
10,21	0,25	23,80	88,50
10,21	0,25	23,70	89,00
10,21	0,25	23,90	89,50
10,21	0,25	23,90	90,00
10,21	0,25	24,00	90,50
10,21	0,25	24,00	91,00
10,22	0,24	24,10	91,50
10,22	0,24	24,20	92,00
10,22	0,24	24,20	92,50
10,22	0,24	24,20	93,00
10,22	0,24	24,30	93,50
10,22	0,24	24,30	94,00
10,22	0,24	24,40	94,50
10,22	0,24	24,40	95,00
10,23	0,24	24,50	95,50
10,23	0,24	24,50	96,00
10,23	0,24	24,60	96,50
10,23	0,24	24,60	97,00
10,23	0,23	24,70	97,50
10,23	0,23	24,70	98,00

10,23	0,23	24,80	98,50
10,23	0,23	24,80	99,00
10,23	0,23	24,90	99,50
10,24	0,23	25,00	100,00
10,24	0,23	25,00	100,50
10,24	0,23	25,10	101,00
10,24	0,23	25,10	101,50
10,24	0,23	25,10	102,00
10,24	0,23	25,10	102,50
10,24	0,23	25,20	103,00
10,24	0,22	25,30	103,50
10,24	0,23	25,30	104,00
10,25	0,22	25,40	104,50
10,25	0,22	25,40	105,00
10,25	0,22	25,50	105,50
10,25	0,22	25,60	106,00
10,25	0,22	25,50	106,50
10,25	0,22	25,60	107,00
10,25	0,22	25,70	107,50
10,25	0,22	25,80	108,00
10,25	0,21	25,80	108,50
10,26	0,21	25,90	109,00
10,26	0,21	25,90	109,50
10,26	0,21	26,00	110,00
10,26	0,21	26,00	110,50
10,26	0,21	26,00	111,00
10,26	0,21	26,20	111,50
10,26	0,21	26,20	112,00
10,26	0,21	26,20	112,50
10,26	0,21	26,20	113,00
10,27	0,21	26,30	113,50
10,27	0,21	26,40	114,00
10,27	0,20	26,40	114,50
10,27	0,20	26,50	115,00
10,27	0,20	26,50	115,50
10,27	0,20	26,60	116,00
10,27	0,20	26,60	116,50
10,27	0,20	26,70	117,00
10,28	0,20	26,70	117,50
10,27	0,20	26,70	118,00
10,28	0,20	26,80	118,50
10,28	0,20	26,90	119,00
10,28	0,20	26,90	119,50
10,28	0,20	26,90	120,00

10,28	0,20	27,00	120,50
10,28	0,20	27,00	121,00
10,28	0,19	27,10	121,50
10,28	0,19	27,10	122,00
10,29	0,19	27,20	122,50
10,29	0,19	27,20	123,00
10,29	0,19	27,30	123,50
10,29	0,19	27,40	124,00
10,29	0,19	27,30	124,50
10,29	0,19	27,40	125,00
10,29	0,19	27,50	125,50
10,29	0,19	27,50	126,00
10,29	0,19	27,60	126,50
10,29	0,19	27,60	127,00
10,30	0,19	27,70	127,50
10,30	0,18	27,70	128,00
10,30	0,18	27,80	128,50
10,30	0,18	27,90	129,00
10,30	0,18	27,90	129,50
10,30	0,18	28,00	130,00
10,31	0,18	28,10	130,50
10,31	0,18	28,10	131,00
10,31	0,18	28,20	131,50
10,31	0,18	28,20	132,00
10,31	0,18	28,20	132,50
10,31	0,18	28,20	133,00
10,31	0,18	28,40	133,50
10,31	0,18	28,40	134,00
10,31	0,17	28,40	134,50
10,31	0,18	28,50	135,00
10,32	0,17	28,50	135,50
10,32	0,17	28,60	136,00
10,32	0,17	28,50	136,50
10,32	0,17	28,70	137,00
10,32	0,17	28,70	137,50
10,32	0,17	28,80	138,00
10,32	0,17	28,80	138,50
10,32	0,17	28,90	139,00
10,32	0,17	28,90	139,50
10,33	0,17	29,00	140,00
10,33	0,17	29,00	140,50
10,33	0,17	29,20	141,00
10,33	0,17	29,10	141,50
10,33	0,17	29,20	142,00

10,33	0,17	29,20	142,50
10,34	0,17	29,40	143,00
10,33	0,16	29,30	143,50
10,34	0,16	29,40	144,00
10,34	0,16	29,40	144,50
10,34	0,16	29,50	145,00
10,34	0,17	29,50	145,50
10,34	0,16	29,60	146,00
10,34	0,16	29,60	146,50
10,34	0,16	29,70	147,00
10,34	0,16	29,70	147,50
10,35	0,16	29,90	148,00
10,34	0,16	29,80	148,50
10,35	0,16	30,00	149,00
10,35	0,16	29,90	149,50
10,35	0,16	30,10	150,00

Appendix D

Surface tension measurements and processing

The following python code was used to obtain the mean and standard deviations from the both the surface tension - and contact angle measurements. The file from which the data is substracted is summarized in table [D.1](#).

```
import numpy as np
import matplotlib.pyplot as plt
import pandas as pd

# Import data
filename = "C:/Users/flori/Desktop/TU Delft/9. Thesis\
    /Experimental results/Surface tension/CA_ST_20210713.xlsx"
dataframe_20210713 = pd.read_excel(filename, '20210713')
CA = np.asarray(np.stack(dataframe_20210713.values[0:12,0]).astype(None))
ST = np.asarray(np.stack(dataframe_20210713.values[: -2,1]).astype(None))

# Statistics
mean_Contact_Angle = np.mean(CA)
dev_Contact_Angle = np.std(CA)
mean_Surface_Tension = np.mean(ST)
dev_Surface_Tension = np.std(ST)

# Print statements
print('Contact angle = ', np.round(mean_Contact_Angle,2), ' + st.dev ', \
    np.round(dev_Contact_Angle,2), ' deg')

print('Surface tension = ', np.round(mean_Surface_Tension,2), ' + st.dev ', \
    np.round(dev_Surface_Tension,2), ' mN/m')
```

Name	Contact angle (deg)	Surface tension (mN/m)
CA1	22.33	20.74
CA2	29.65	18.25
CA3	30.74	22.77
CA4	36.92	28.21
CA5	27.34	32.76
CAST1	29.59	42.77
CAST2	33.53	35.69
CAST3	34.80	25.61
CAST4	33.57	18.58
CAST5	24.10	24.84
CAST6	38.20	27.32
Test	30.53	25.22
PD1	-	25.02
PD2	-	24.88
PD3	-	24.77

Table D.1: Measured surface tension and contact angle from 96 wt % Omnilane OC1005 + 3 wt% Genocure ITX + 1 wt% Omnicat 250. Note that 'PD' in the name column stands for pendant drop method which can be used to determine the surface tension. 'CA' and 'CAST' on the other hand were measurements based on the sessile drop method, which is capable of measuring both the surface tension as the contact angle.

Appendix E

Global permeability determination

The global permeability was determined based on tracking the flow propagation through the preform over time, based on the methodologies presented in the work of Vernet et al. [25], which can be found in section 7.1. The injection parameters used for this analysis can be found in table E.1 and the propagation of the flow front over time for 6 different injection are shown in table E.2.

Table E.1: Injection parameters used to determine the global permeability values

Sample	FF5	FF6	VC2	VC3	VD1	VD2
Pressure drop [Pa]	51300,00	51300,00	51300,00	51300,00	51300,00	51902,00
Temperature [degC]	21,56	21,70	19,67	22,80	20,75	22,90
Global porosity sample [-]	0,70	0,68	0,69	0,68	0,69	0,69
Thickness sample [mm]	1,50	1,42	1,47	1,41	1,44	1,45
Viscosity [Pa*s]	0,31	0,30	0,36	0,28	0,33	0,27
KLSF [m ²]	1,68E-10	1,67E-10	1,37E-10	1,56E-10	1,22E-10	1,41E-10
KSSF [m ²]	1,57E-10	1,61E-10	1,25E-10	1,46E-10	1,21E-10	1,36E-10

Table E.2: Flow front tracking information used for permeability determination

Sample	Datapoint	1	2	3	4	5	6	7	8	9
FF5	Impregnated length [cm]	0	2	4	6	8	10	12	14	16,5
	Time [s]	0	6	25	51	89	132	180	238	322
FF6	Impregnated length [cm]	0	2	4	6	8	10	12	14	16,5
	Time [s]	0	8	20	45	80	127	177	237	318
VC2	Impregnated length [cm]	0	2	4	6	8	10	12	14	16,5
	Time [s]	0	11	35	73	130	194	263	350	444
VC3	Impregnated length [cm]	0	2	4	6	8	10	12	14	16,5
	Time [s]	0	8	23	47	81	123	169	226	301
VD1	Impregnated length [cm]	0	2	4	6	8	10	12	14	16
	Time [s]	0	10	32	62	115	182	260	354	467
VD2	Impregnated length [cm]	0	2	4	6	8	10	12	14	-
	Time [s]	0	6	22	49	86	134	184	240	-